Communauté
UNIVERSITÉ Grenoble Alpes

THÈSE

Pour obtenir le grade de

DOCTEUR DE LA
COMMUNAUTÉ UNIVERSITÉ GRENOBLE ALPES

Spécialité : 2MGE : Matériaux, Mécanique, Génie civil, Electrochimie

Arrêté ministériel : 25 mai 2016

Présentée par

Seyed Ali ELAHI

Thèse dirigée par **Yohan PAYAN,** CNRS
et codirigée par **Nathanaël CONNESSON,** UGA
préparée au sein du **Laboratoire Techniques de L'Ingénierie Médicale et de la Complexité – Informatique, Mathématiques et Applications Grenoble**
dans **l'École Doctorale I-MEP2 – Ingénierie – Matériaux, Mécanique, Environnement, Energétique, Procédés, Production.**

Vers la caractérisation in-vivo et in-situ des propriétés mécaniques des tissus mous du vivant

Towards in-vivo and in-situ mechanical characterization of soft living tissues

Thèse soutenue publiquement le **4 octobre 2018**,
devant le jury composé de :

Monsieur Yohan PAYAN
PROFESSEUR, CNRS DELEGATION ALPES, Directeur de thèse
Monsieur Nathanaël CONNESSON
MAITRE DE CONFERENCES, UNIVERSITE GRENOBLE ALPES, Codirecteur de thèse
Monsieur Edoardo MAZZA
PROFESSEUR, ETH ZURICH - SUISSE, Rapporteur
Monsieur Poul MICHAEL FONSS NIELSEN
PROFESSEUR, UNIVERSITE D'AUCKLAND - NOUVELLEZELANDE, Rapporteur
Monsieur Aain-Ali MOJALLAL
PROFESSEUR, UNIVERSITE DE LYON, Examinateur
Monsieur Jacques OHAYON
PROFESSEUR, UNIVERSITE GRENOBLE ALPES, Président

To my dearest wife,

who leads me through the valley of darkness
with light of hope and support.

ACKNOWLEDGMENTS

To my life-coaches, my parents Saeedeh Mozafari and Seyed Morteza Elahi: because I owe it all to you.

My sincere thanks goes to my supervisors Prof. Yohan Payan and Dr. Nathanael Connesson for the continuous support of my Ph.D. study and related research, for their patience, motivation, and immense knowledge. Their guidance helped me in all the time of research and writing of this thesis.

Besides my supervisors, I would like to thank the rest of my thesis committee: Prof. Edoardo Mazza, Prof. Poul Michael Fonss Nielsen, Prof. Alain-Ali Mojallal, and Prof. Jacques Ohayon for their insightful comments and encouragement, but also for the hard questions which incented me to widen my research from various perspectives.

A very special gratitude goes out to Dr. Gregory Chagnon for his endless supports. I also thank my colleagues in BioMMat team for the stimulating discussions and for all the fun we have had in the last three years.

And finally, last but by no means least, to my wife Hanie Zarafshani for supporting me spiritually throughout writing this thesis and my life in general.

ABSTRACT

In-vivo characterization of biological soft tissues is a key step toward patient-specific biomechanical simulation and planning of intra-operative assisted surgery. Unfortunately, these tissues' structures are usually highly heterogeneous due to the variety of their constituents (skin, mucosa, muscle fibers, fat, fascia, vascularization, etc.). In particular, their local mechanical properties may change with depth. Characterizing such materials is thus highly challenging, especially if in-vivo characterizations are required.

Among various characterization techniques, aspiration method is a standard due to its simplicity: tissue is aspirated through a hole while measuring the negative pressure and the associated apex height. An inverse problem is then solved to identify the material mechanical properties. In the literature, the apex height was usually measured using a camera, which induced design difficulties, in particular regarding the required sterilization process for in-vivo measurements.

This thesis aims at developing new practical aspiration techniques and inverse analyze techniques to deal with these challenges. First, the aspiration method is revisited, replacing the apex height optical measurement by the measurement of the aspirated tissue volume. The proposed method enables reduction of the system head to a simple tube: sterilization becomes easy and the aspiration aperture diameter can be changed according to experimental requirements. The proposed system is thus probably among the simplest, lightest and most inexpensive devices one could achieve.

Then, many studies are developed: (i) a comparison of this volume-based method with classical techniques based on optical measurements, (ii) the validation of the volume-based aspiration device and inverse identification on soft homogeneous synthetic materials, (iii) the development of a method for in-vivo identification of multi-layered soft tissues and its validation on two-layer synthetic samples, and (iv) a method for real-time inverse mechanical identification of constitutive materials using the aspiration results.

To address this issue (i), the experimental signal-to-noise ratio in raw volume measurements obtained either optically or by the volume-based method were compared. The effects on the accuracy of various experimental parameters were investigated and quantified: the volume measurement was proved to present the same order or even better signal-to-noise ratio compared to optical measurements.

To validate the inverse identifications (issue (ii)) using the volume-based aspiration method, silicone samples were then made and characterized using (1) aspiration, and, as references, two standard tests such as (2) uniaxial and (3) equibiaxial extension tests. Performing a Finite Element (FE) inverse identification on the experimental results provided Young's moduli similar to classical tests with about 7% maximum overestimation

for the silicones. This underlines a significant improvement of the measurement method accuracy compared to the literature (about 30% relative overestimation).

In the proposed device, the aspiration aperture diameter can be easily changed. This feature was used to develop a new method to characterize the mechanical properties as well as the superficial layers' thicknesses in multi-layer soft tissues (issue (iii)). A proof of concept was experimentally validated on two-layer artificial soft silicone specimens. As a conclusion, the superficial layer thicknesses and the materials Young's moduli were identified with a maximum error of 4% and 8%, respectively. Such results thus provide encouraging perspectives for the in-vivo characterization of two-layer anatomical structures such as skin and sub-dermal tissues.

Eventually, a Design Of Experiment (DOE) method was applied to drastically decrease the computation time involved during the inverse identification step, which is a prerequisite for any use in a clinical routine (issue (iv)). The identifications using the DOE method were compared with the reference characteristics of the investigated silicones and maximum errors of 10 and 12% were obtained for the homogeneous and two-layer samples, respectively.

All these developments, associated with the low cost of the system, should help to generalize the method among physicians and encourage its use in operative rooms.

Résumé

Cette thèse s'inscrit dans la démarche de caractérisation mécanique des tissus mous du vivant in situ et in vivo par un dispositif de succion utilisable en salle opératoire. L'objectif est de fournir au chirurgien un outil simple, efficace, et si possible de coût réduit, pour estimer les propriétés mécaniques spécifiques au patient et en temps réel afin guider leur décisions (simulation, planification d'opération, etc). Malheureusement, les structures biologiques sont souvent hétérogènes due à leur composition (peau, muqueuse, fibres musculaires, matière adipeuse, fascias, vascularisation,). En particulier, ces structures biologiques présentent un gradient de propriétés mécanique dans la profondeur. Il s'agit donc de répondre à un problème complexe, d'autant plus qu'il est nécessaire de proposer une méthode non destructive adaptée à une mesure in situ et in vivo en salle opératoire.

Parmi les procédés de caractérisation mécanique rencontrés, les méthodes basées sur la succion sont courantes. Ce procédé de mesure consiste à aspirer un volume de tissu mou à travers une ouverture en mesurant simultanément la pression et la hauteur de tissu dans l'enceinte. Une procédure d'identification inverse est ensuite mise en place pour identifier les propriétés mécaniques du tissu. Cette mesure de hauteur étant généralement effectuée à l'aide d'une caméra, le design des systèmes rencontrés reste cependant délicat, en particulier pour respecter les contraintes d'encombrement et de stérilisation des systèmes.

Au cours de ce travail, la méthode d'aspiration a été revisitée en remplaant la mesure de hauteur par une mesure de volume. L'extrémité du dispositif d'aspiration se réduit maintenant à un simple tube : le système fourni est donc facilement stérilisable, le diamètre et la géométrie de l'ouverture peuvent être choisis en fonction des objectifs des mesures à effectuer. Il semble donc difficile d'imaginer un système plus simple, d'encombrement plus réduit et de cot inférieur à celui-ci.

Plusieurs problématiques ont été étudiées autour de ce nouveau système : (i) les précisions de mesures obtenues par volume ou, plus classiquement, par caméra ont été

confrontées. Au bilan, la mesure de volume présente un ratio signal/bruit similaire ou inférieur aux mesures de volume obtenues par caméra. L'impact de différents paramètres expérimentaux a été évalué et quantifié, permettant d'optimiser la qualité des mesures.

(ii) les résultats d'identification inverse ont été validés sur des échantillons en silicone. Leur matériau constitutif a été caractérisé pour référence en traction uniaxiale et par bulge test. Les modules de Young obtenus par identification inverse sur le test d'aspiration (calcul itératif par Elements Finis) montrent une sur-estimation de 7% au maximum avec les résultats des tests de référence. Ce résultat est une amélioration significative par rapport aux sur-estimations de 30% rencontrées dans la littérature.

(iii) les caractéristiques du système ont été mises à profit pour mesurer directement l'épaisseur et les propriétés mécaniques de couches superficielles de tissus multicouches sans autre système de mesure. La preuve de concept a été effectuée expérimentalement sur un échantillon artificiel constitué de deux silicones différents. Au bilan, l'épaisseur de la couche supérieure a été identifiée avec une erreur inférieure à 4% , les modules de Young des deux matériaux avec une erreur inférieure à 8%. Ces résultats sont jugés très encourageants pour une future application de la méthode à des tissus du vivant : identifier in-vivo les caractéristiques mécaniques de structures anatomiques composées de plusieurs couches telles que la peau semble à portée.

(iv) une méthode d'identification inverse des propriétés mécaniques en temps réelle a été développée. Cette procédure est basée sur une réduction de modèle et fournit également des indications sur la sensibilité de l'identification aux différents paramètres expérimentaux. L'utilisation de cette méthode d'inversion a montré une erreur d'identification de 10 et 12% par rapport aux valeurs de références sur les spécimens constitués de deux couches de silicones. L'augmentation de l'erreur d'identification a été jugée acceptable en regard au gain de temps obtenus lors de l'identification inverse.

Enfin, ces développements, associés au faible coût de ce système, devraient favoriser l'utilisation de cette méthode de caractérisation in-vivo et in-situ en salle opératoire.

CONTENTS

LIST OF FIGURES

LIST OF TABLES

GENERAL INTRODUCTION

Context

This thesis was funded by a French ministerial grant at the research laboratory "Techniques de l'Ingénierie Médicale et de la Complexité - Informatique, Mathématiques et Applications, Grenoble"(TIMC-IMAG). It was performed between the "Biomedical and Mechanical engineering of Materials"(BioMMat) and "Computer-Assisted Medical Interventions"(CAMI) teams. The thesis focuses on *in-vivo* and *in-situ* mechanical characterization of soft living tissues.

Objectives

Simulating the deformations of soft tissues has gained importance in recent years due to the development of 3D patient-specific biomechanical models in the context of Computer Assisted Medical Interventions. Since the mechanical behavior of living tissues varies between *in-vivo* and *ex-vivo* conditions, measuring these properties *in-vivo* and *in-situ* is important. To perform intra-operative measurements on human, the procedure must be non-traumatic and operated under sterile conditions. It also has to comply with space and time limitations in the operating room. Considering these constraints, several devices were developed in the literature based on various measurement methods.

Among all the proposed methods, the aspiration technique is one of the easiest to use and allows a good control of the applied experimental boundary conditions. Such aspiration method consists in putting a chamber with an aperture in contact with the investigated soft tissue and then decreasing the pressure inside the chamber. Due to the pressure difference, the portion of the tissue under the aperture is partially aspirated. For a given pressure difference, it has usually been proposed to measure the aspirated tissue height using various methods such as ultrasound, mechanical stops or cameras, associated to mirrors or prisms. An inverse problem is then solved to identify the material mechanical properties.

These methods based on the measurement of the aspirated tissue height suffer from constraints which make them difficult to be used during surgery, under sterile conditions. In order to address this question, this thesis aims at introducing and validating an original aspiration technique by replacing the apex height optical measurement by the measurement of the aspirated tissue volume. The proposed method enables to reduce the system head to a simple tube: the sterilization becomes easy and the head is disposable

after use. The proposed system is thus probably among the simplest, lightest and most inexpensive devices one could achieve.

Moreover, several complexities occur while studying biological soft tissues: these tissues are usually heterogeneous, anisotropic and made of multi-layer materials due to their inner structure (muscle fibers, fat, skin, mucosa, vascularization, *etc.*). As the proposed volume-based aspiration device easily enables the use of various aperture diameters, a new method was developed to study the in-depth heterogeneity of multi-layer soft tissues. The targeted application being an intra-operative use of the device for modeling the static behavior of soft tissues, the dynamic loading of the tissues was out of the scope of this study.

Organization of the manuscript

The manuscript is divided into five chapters.

Chapter 1 focuses on the experimental methods to identify the mechanical behavior of human soft tissues. First, mechanical behavior of soft tissues under different loading conditions is presented. Then, a brief comparison is made between *in-vivo* and *in-vitro* mechanical characterization, while the frequently used methods for *in-vivo* experimental measurements are introduced. Subsequently, the various experimental techniques proposed in the literature are discussed and the aspiration method is highlighted. The chapter ends with an anatomical description of the human soft tissues with a focus on skin that will be the first anatomical structure studied with our new aspiration device in a near future.

Chapter 2 introduces our volume-based aspiration device and assesses its performance. As the data signal-to-noise ratio is the main factor impacting any applied inverse method when extracting the mechanical properties, the aim of this chapter is to assess and compare the experimental signal-to-noise ratio in the raw volume measurements obtained either optically or with the proposed method. In this chapter effects on accuracy of various experimental parameters is investigated and quantified: the volume measurement is proven to present a same order or even better signal-to-noise ratio compared to the usual optical measurements.

Chapter 3 focuses on the validation of the volume-based aspiration method on synthetic materials. For this purpose, two silicones with slightly different stiffnesses were made. Samples were characterized using (1) our aspiration test along with an updated Finite Element (FE) inverse characterization, and, as references, two standard tests such as (2) uniaxial and (3) equibiaxial extension tests.

In the proposed device, the aspiration aperture diameter can be easily changed. This feature is used in Chapter 4 to develop a new method to characterize the mechanical properties as well as the superficial layers thicknesses in multi-layer soft tissues. The proof of concept was experimentally validated on artificial soft silicone specimens composed of a single superficial layer of silicone#1 over a bulk volume of silicone#2. To mimic the behavior of skin and subcutaneous complex, silicone#2 was softer than silicone#1. The silicones' mechanical properties, used as references, were experimentally measured with classical uniaxial tensile test and bulge test.

Chapter 5 presents a Design Of Experiment (DOE) method to drastically decrease the computation time involved during the inverse identification step, which is a prerequisite

for clinical routine application. In this chapter, the method is presented using a simple example and is then evaluated for the inverse characterization of homogeneous and two-layer silicones that were tested in Chapters 3 and 4, respectively.

CHAPTER

ONE

LITERATURE REVIEW

1.1 Introduction

Understanding and measuring human organs' mechanical properties impacts medical practices [Payan and Ohayon, 2017]. In particular, such mechanical properties provide insights for clinical diagnosis [Badir, Bajka, and Mazza, 2013; Mazza et al., 2014], surgical training (simulators) [Székely, 2003], tissue replacement engineering [Gentleman et al., 2003], and trauma research [Snedeker et al., 2002]. These novel applications have raised a need for accurate modeling of the human soft tissues mechanical behavior.

The aim of this chapter is to give an overview on the structure and the mechanical behavior of biological soft tissues and to present different existing methods for the mechanical characterization of such tissues. Section 1.2 briefly presents various experimental observations made during mechanical tests on soft tissues. The experimental measurement methods for a mechanical characterization of soft tissues can be divided into two main categories: *in-vivo* and *in-vitro* measurements, which are compared in section 1.3. Different experimental methods for *in-vivo* mechanical characterization of soft living tissues are then discussed and compared in section 1.4. Finally, section 1.5 will introduce a generic and schematic representation of the skin and subcutaneous complex recently published in the literature.

1.2 Mechanical behavior of biological soft tissues

During this Ph.D. work, the mechanical properties of soft tissues have been identified with the aspiration experimental data using an inverse updated Finite Element (FE) method. The constitutive laws that characterize the mechanical properties of human soft tissues have to be defined for modeling and simulating tissues and organs responses to external mechanical stresses [Budday et al., 2017a; Holzapfel and Ogden, 2010; Payan and Ohayon, 2017; Schwenninger David, Schumann, and Guttmann, 2011]. Such constitutive laws are usually based on the experimental observations of the materials behavior in specific loading conditions.

This section focuses on describing the various phenomena encountered during the biological soft tissues mechanical testing. Modeling of these phenomena using constitutive laws is summarized in Appendix A.

1.2.1 Experimental stress-strain relationship of soft tissues

In order to characterize the mechanical properties of a material (biological or not), its behavior under different loading conditions should be observed. To observe stress-strain relationship of classic soft materials, two tests have been chosen in the literature: (1) uniaxial tensile test (Fig. 1.1) [Farshad et al., 1999; Ní Annaidh et al., 2012; Veronda and Westmann, 1970] and (2) equibiaxial tensile test that can be generated at the top of a bulge test (Fig. 1.2) [Lally, Reid, and Prendergast, 2004; Machado, 2011; Qi and Boyce, 2004; Zemánek, Burša, and Děták, 2009]. In this Ph.D. work, the uniaxial tensile test and the bulge test are used to characterize the studied materials. The results provided by these tests will be used as references to compare with the identifications provided by our aspiration device.

Uniaxial extension test, also known as tensile or tension test, has been extensively used for the identification of the mechanical behavior of soft materials. The test consists in placing a standard specimen between two machine jaws and applying a given uniaxial displacement or a prescribed uniaxial force to the sample (Fig. 1.1). The machine measures the material response, namely the force or the displacement, simultaneously. The stress-strain behavior of the material is then calculated using the experimental results.

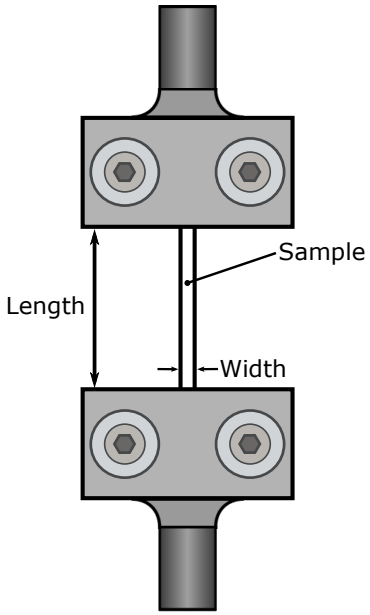

Figure 1.1: Uniaxial tensile test configuration [Masri, 2017].

A bulge test, also called balloon test, consists of a thin disk specimen (testing sample in Fig. 1.2), constrained between two clamping flanges. This test setup consists in an air or liquid piston connected to the bottom circumferential clamp. The internal pressure is measured with a manometer. For this test, out-of-plane displacements measurements are needed, therefore a Stereo Digital Image Correlation (SDIC) system is used to acquire and correlate the images. With such a stereo-correlation, it is possible to reconstruct the geometry of the deformed sample surface geometry as well as to determine its displacement and strain fields. The axial-symmetry of the experimental configuration and the isotropic and homogeneous material behavior assumptions induce the equibiaxiality

of the stress and strain state at the top of the inflated membrane (point M). Given the thickness dimension is largely smaller than the membrane diameter, the in-plane stresses are assumed to be uniform along the thickness dimension. The in-plane stress at point M can be calculated using the internal pressure data and the obtained deformations using the SDIC system. More details about the performed bulge test in this work can be found in chapter 3.

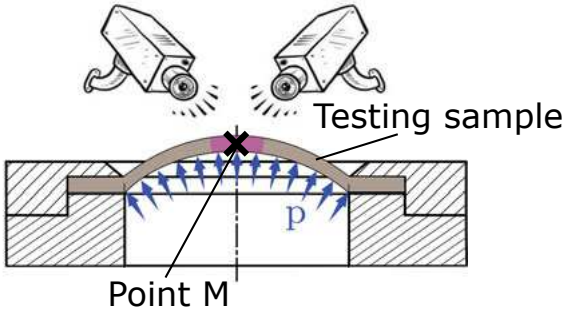

Figure 1.2: Bulge test configuration [Machado et al., 2017].

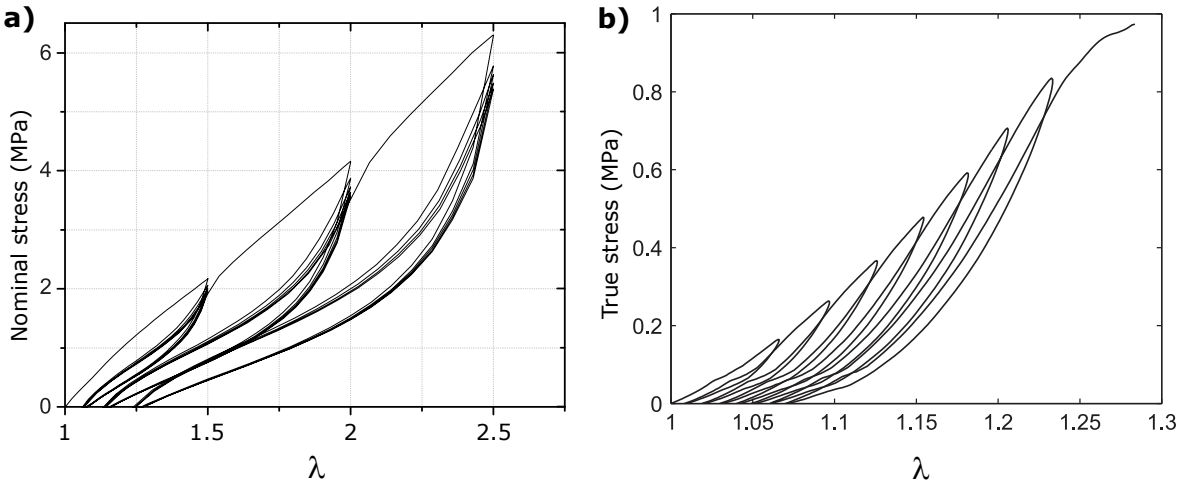

Figure 1.3: Stress-stretch curves of a) a hot temperature vulcanization silicone rubber [Rebouah, 2014] and b) ovine vena cava tissue [Peña, 2014].

Both the tensile and the bulge tests permit the observation of the material mechanical behavior in specific loading conditions (quasi-static and dynamic loadings). Biological soft tissues exhibit highly nonlinear mechanical behavior, like many filled rubber-like materials [Machado, Chagnon, and Favier, 2010]. Figure 1.3a shows the stress response of a silicone rubber material under a time-dependent cyclic (loading-unloading) stretch in a quasi-static loading condition, while Fig. 1.3b illustrates the graph for cyclic stretch of the ovine vena cava tissue. These graphs permit observation of many typical mechanical behaviors, namely viscoelasticity, stress-softening and residual strain. These different phenomena are introduced in the following section.

1.2.2 Different mechanical behaviors

Viscoelasticity

The difference between the loading and unloading phases of a cyclic test response is known as hysteresis (Fig. 1.3) [Morris, 2011]. The hysteresis in a biological soft tissue can be modeled as viscoelasticity.

Other methods to characterize the viscoelasticity in the materials are relaxation and creep. Relaxation is observed when the material is subjected to a constant strain while the stress response decreases in time. Creep happens when the strain increases while a constant stress is applied to the material [Findley, Lai, and Onaran, 1976]. Another method to identify the viscoelasticity in the materials is Dynamic Mechanic Analysis (DMA) based on dynamic tests [Odegard, Gates, and Herring, 2005]. In such tests some vibrations are applied to the material sample while the resonant frequency is measured [Menard, 2008].

Most of the biological soft tissues have a viscoelastic behavior. This is for example the case for arterial walls [Holzapfel, Gasser, and Stadler, 2002], skin [Jor et al., 2013; Vexler, Polyansky, and Gorodetsky, 1999], liver [Asbach et al., 2008] and uterine tissue [Omari et al., 2015].

Stress softening

The stress-softening effect is observed when a soft sample is loaded, unloaded, and then reloaded. In a material with a stress-softening behavior, the load required to produce a given stretch during reloading is smaller than that the one required to produce the same stretch during the primary loading phase [Beatty and Krishnaswamy, 2000]. After exceeding the previous maximal applied strain, the material stiffness returns to its original stiffness. This phenomenon is also known as the Mullins effect [Mullins, 1948, 1969]. The material response shown in Fig. 1.3, clearly manifests such a Mullins effect at each strain level.

The biological soft tissues usually exhibit similar behavior with this difference that, in the rubber-like materials, the stress-softening is permanent while for the biological soft tissues the initial behavior is recovered after some time [Masri, 2017].

Residual strain

It has been shown that arteries removed from the body that are load-free are not stress-free (or strain-free) [Holzapfel, 2001]. This phenomena, which is known as residual strain or permanent set, is defined as a positive strain in an unloaded material after applying a load cycle. The residual strain was observed in other biological soft tissues like tendon [Abrahams M, 1967], brain [Franceschini et al., 2006], skin [Muñoz et al., 2008], vaginal tissues [Peña, 2011], *etc.*

Figure 1.3 shows residual strains caused by cyclic loading of a silicone rubber. As it can be observed in this figure, the magnitude of residual strain depends on the maximum elongation of the material prior to unloading: a larger elongation causes a larger residual strain.

The residual strain magnitude is time-dependent [Dorfmann and Ogden, 2004]. It means that the material viscoelasticity is effective in its residual strain during cyclic

loads. The residual strain due to the material viscoelasticity can thus be recovered over a period of time.

Anisotropy

The anisotropy in a material is defined as a directionally-dependent mechanical behavior. This phenomenon can be observed when uniaxial tensile testing of the materials in different directions, provide different stress responses. Most of the biological soft tissues depict anisotropic behavior under loading in different directions [Cox et al., 2008; Holzapfel, 2001; Picinbono et al., 2001]. The anisotropy in soft tissues is due to the presence of muscle fibers, vascularization, mesostructural collagen fiber networks, *etc.*.

1.3 In-vivo versus in-vitro experimental measurements

To estimate the mechanical properties of soft tissues, the experimental measurements have been performed *in-vitro* or *in-vivo* [Budday et al., 2017a; Cox et al., 2008; Nicolas et al., 2018; Pensalfini et al., 2018; Samani, Zubovits, and Plewes, 2007].

In the *in-vitro* experimental approaches, different tissue parts can be separated and tested under various loading conditions [Brown et al., 1998; Budday et al., 2017b; Miller and Chinzei, 2002; Miller et al., 2000], while in the *in-vivo* approaches, the living tissues undergo *in-situ* experimental measurements [Agache et al., 1980; Hendriks et al., 2006a; Schiavone et al., 2008].

The mechanical behavior of soft tissues can differ significantly between *in-vivo* and *ex-vivo* conditions due to various reasons *e.g.* the vascularization of the tissues, change in boundary conditions, temperature, oxygenation, *etc.* [Kerdok, Ottensmeyer, and Howe, 2006; Schiavone et al., 2008]. Therefore, *in-vivo* and *in-situ* measurements seem almost mandatory to take into account patient specificities, to maintain the natural state of the tissues and to estimate more realistic mechanical properties.

1.4 Methods for in-vivo mechanical characterization of soft living tissues

In order to perform intra-operative measurements on humans, the procedure must be non-traumatic and operated under sterile conditions. The proposed procedure must also comply with space and time limitations within the operating room. These constraints motivated researchers to design devices with small sizes, low weights and avoiding if possible any electronic parts, so as to be able to withstand severe sterilization processes.

To measure *in-vivo* and *in-situ* the sought mechanical properties, various methods have been proposed in the literature such as indentation, grasping, torsion, and aspiration. The principle in these methods is to apply a given displacement to the tissue and to measure the force response. In most of the cases, the mechanical properties of soft tissues are characterized using an inverse procedure. The following sections provide brief descriptions of the different experimental methods, their limitations and their advantages.

1.4.1 Indentation method

In this method, a displacement is applied at the surface of the soft tissue using an indenter and the force response is measured with respect to the indentation depth and elapsed time.

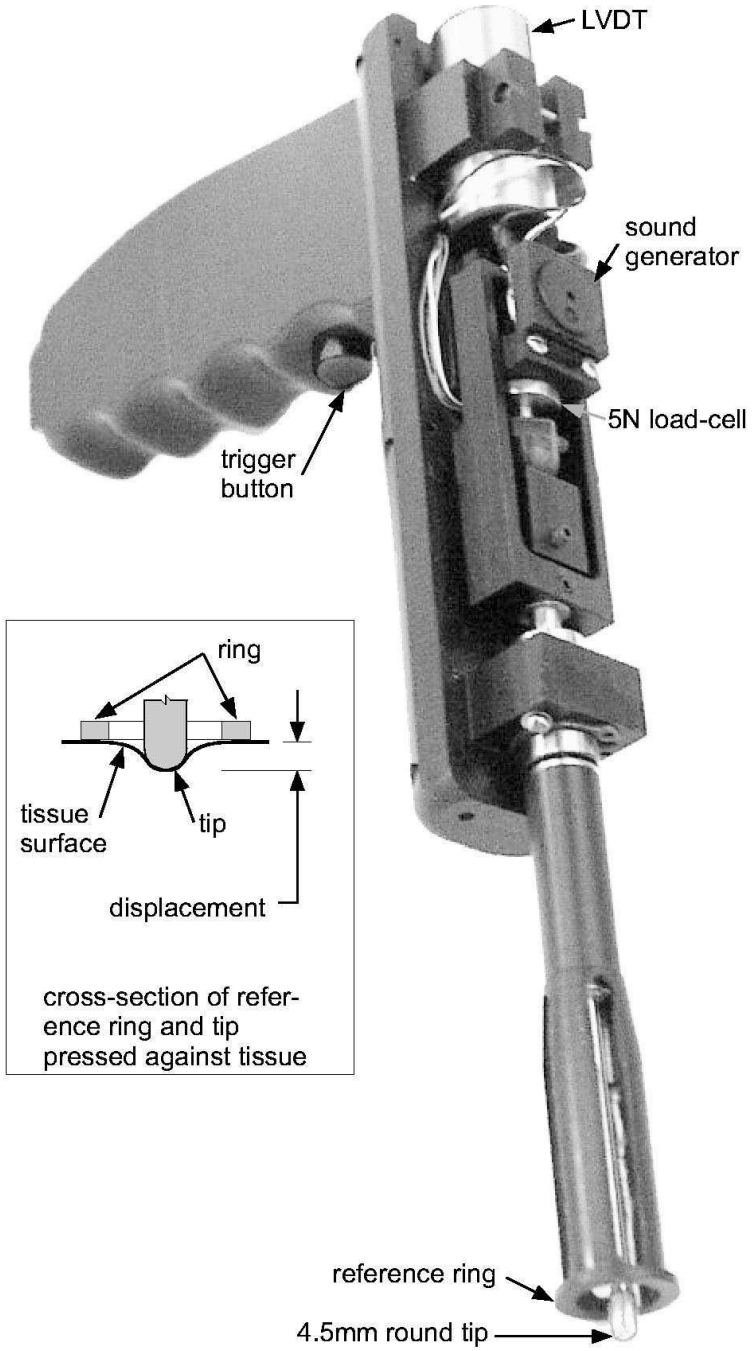

Figure 1.4: A motorized indentation device for *in-vivo* measurement of soft tissues mechanical behavior [Carter et al., 2001].

There are two main types of indentation devices: motorized ones and hand-held ones. The major benefit of hand-held devices is that using them reduces the possibility

of risky movements in comparison with the motorized devices. On the other hand, the measurements using the hand-held devices are less reproducible and less reliable [Samur et al., 2007].

Figure 1.4 shows a motorized indentation device, which was used by Carter et al., 2001 for the *in-vivo* characterization of human abdominal soft tissues. With such a device, because of the difficulties keeping the probe stationary during the measurements, it was not possible to measure the displacements relative to the probe handle. Instead, the displacements were measured relative to a reference ring surrounding the contact tip. The tip and the ring assembly could be sterilized while the rest of the device parts, which had difficulties for sterilization (because of electronic parts), were placed in a sterile sleeve during the measurements.

The main limitation of the indentation method is its difficulty to secure an accurate positioning of the device tip with respect to the tissue, in a way that they are in contact and the tissue is not affected by any initial force due to the tip [Yao et al., 2014].

1.4.2 Grasping method

The Grasping method is a minimally invasive technique to measure the mechanical behavior of soft tissues. The method consists in pressurizing the soft tissue in a grasper using a known displacement and estimating the force response by a strain gage. For this purpose, surgical graspers were modified by adding strain gages and used as the measurement devices [Brouwer et al., 2001]. Laparoscopic measurements are enabled in the grasping method by using laparoscopic graspers [Rosen et al., 1999].

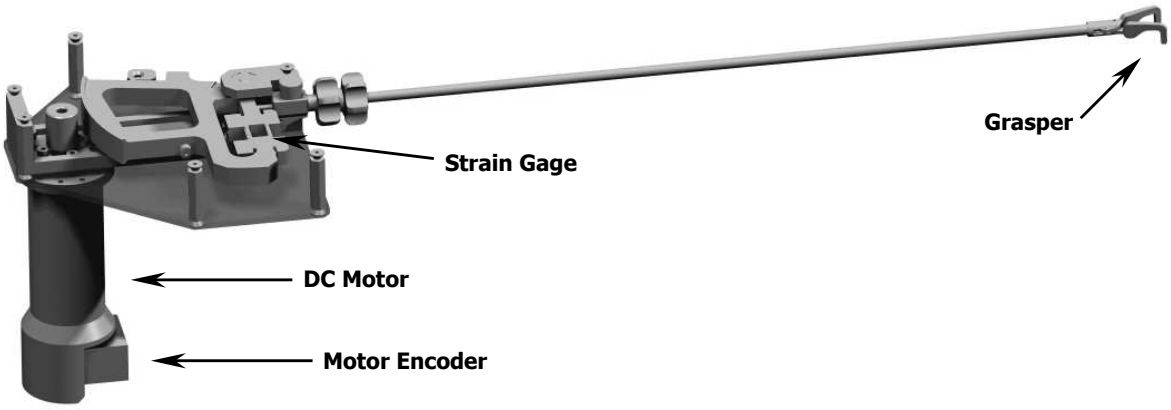

Figure 1.5: A motorized endoscopic grasper [Brown et al., 2002].

Like the indentation devices, the grasping instruments can be categorized into two main types: manual driven and automated devices. Figure 1.5 shows an automated endoscopic grasping instrument developed by Brown et al., 2002 for *in-vivo* measurement of the soft tissues mechanical properties. This device uses a brushed DC motor to drive a grasper and a strain gage to estimate the force applied by the grasper jaws to the tissue. The device was capable of applying about 70 N of grasping force [Brown et al., 2003].

Like for the indentation method, the problem of the accurate positioning of the device according to the tissue is still unresolved. Moreover, the risk for tissue damage in the grasping is higher compared to the other presented *in-vivo* measurement techniques.

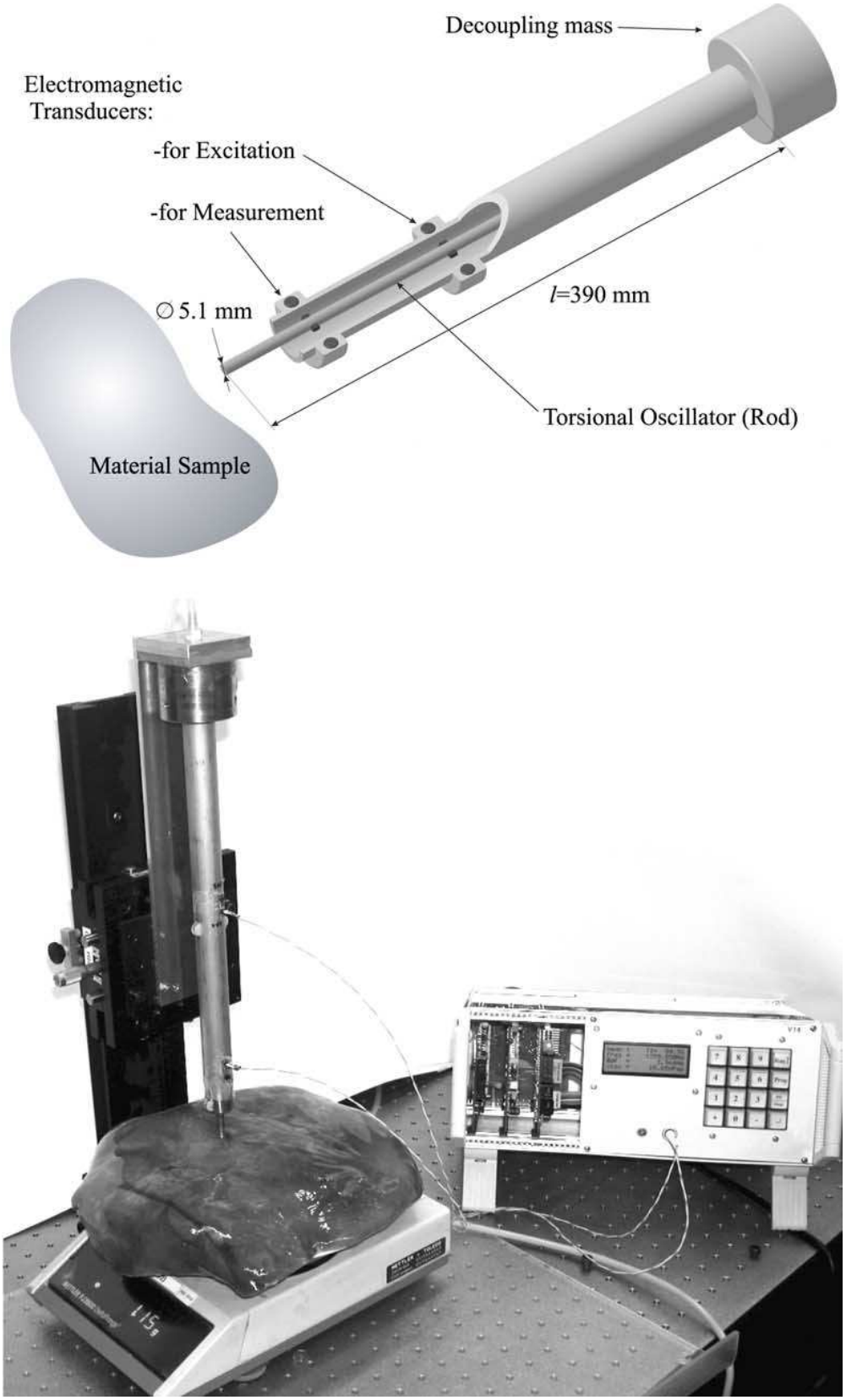

Figure 1.6: A torsion device sketch (above) and photograph of testing on a soft tissue (below) [Valtorta and Mazza, 2005].

1.4.3 Torsion method

In the torsion method, the device probe (usually a disc) comes in contact with the investigated tissue and a torque is applied to the tissue using the probe. Knowing the applied torque, the probe motion is measured using a dedicated sensor. The torsion method was often used for *in-vivo* measurement of the human skin mechanical behavior [Agache et al., 1980; Finlay, 1971; Sanders, 1973].

Figure 1.6 illustrates the components of a torsional device and its photograph during an *ex-vivo* test on a soft tissue. This device was used by Valtorta and Mazza, 2005 for the dynamic measurement of viscoelastic properties. The instrument was made of a brazen cylinder that was excited by an electromagnetic transducer. A second electromagnetic transducer was used as a sensor for measuring the motion. When the probe comes in contact with the soft tissue, changes occur in the dynamic properties of the vibrating system.

In the torsion technique, like the previously presented techniques, the relative motion of the device probe according to the tissue may cause considerable errors in the measurements.

1.4.4 Aspiration method

As this method is of particular interest in this work, the different aspiration devices existing in the literature are described in detail.

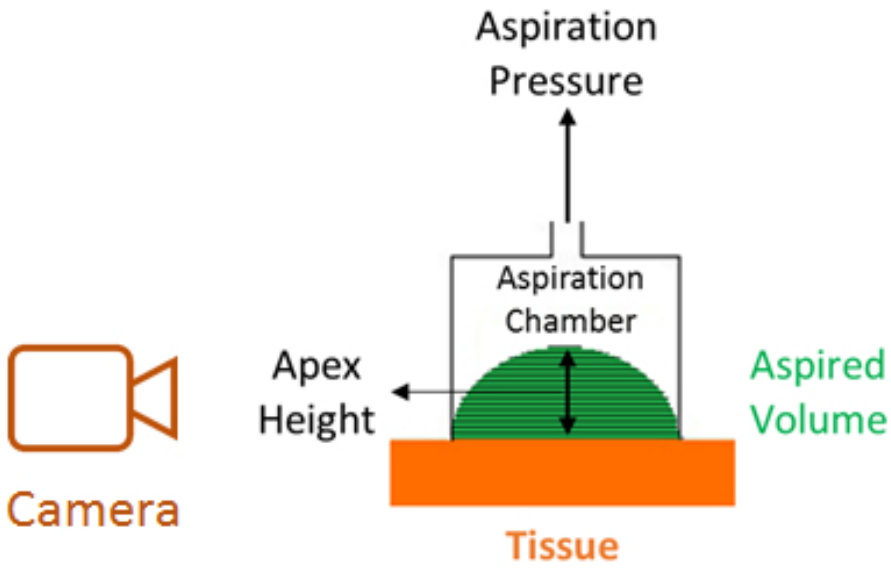

Figure 1.7: General scheme of the aspiration method [Elahi, Connesson, and Payan, 2018].

The principle of the aspiration method consists in putting a chamber with a hole in contact with the tissue and in setting a negative pressure inside the chamber. The tissue is thus aspirated inside the chamber through the hole while the negative pressure is measured during the test (Fig. 1.7). Authors usually propose to measure the aspirated tissue height using different methods such as ultrasound [Diridollou et al., 2000; Hendriks

et al., 2006a], mechanical stops [Badir, Bajka, and Mazza, 2013] or cameras associated to mirrors or prisms [Hollenstein et al., 2013; Kauer et al., 2001; Luboz, Promayon, and Payan, 2014; Luboz et al., 2012; Nava et al., 2008; Schiavone et al., 2008; Schiavone et al., 2009; Schiavone, Promayon, and Payan, 2010; Weickenmeier, Jabareen, and Mazza, 2015].

The device developed by Diridollou et al., 2000 is an example of using ultrasound method for aspirated tissue height measurement (Fig. 1.8). This device was composed of a small cylinder with an aperture under it and an ultrasound transducer fixed inside the cylinder. Putting the aperture in contact with the tissue and applying a partial vacuum inside the cylinder, the tissue was aspirated into the cylinder. An electronic circuit automatically detected the first echo corresponding to the coupling liquid/ tissue surface interface, which permitted measurement of the vertical displacement of the tissue surface. This device was used to characterize human skin.

Yet, as ultrasound methods add additional experimental constraints (ultrasound imaging requires the use of an ultrasound machine and a coupling liquid interfacing the probe with the tissue), optical methods are usually preferred in practical cases to provide pressure versus apex height characteristic curves.

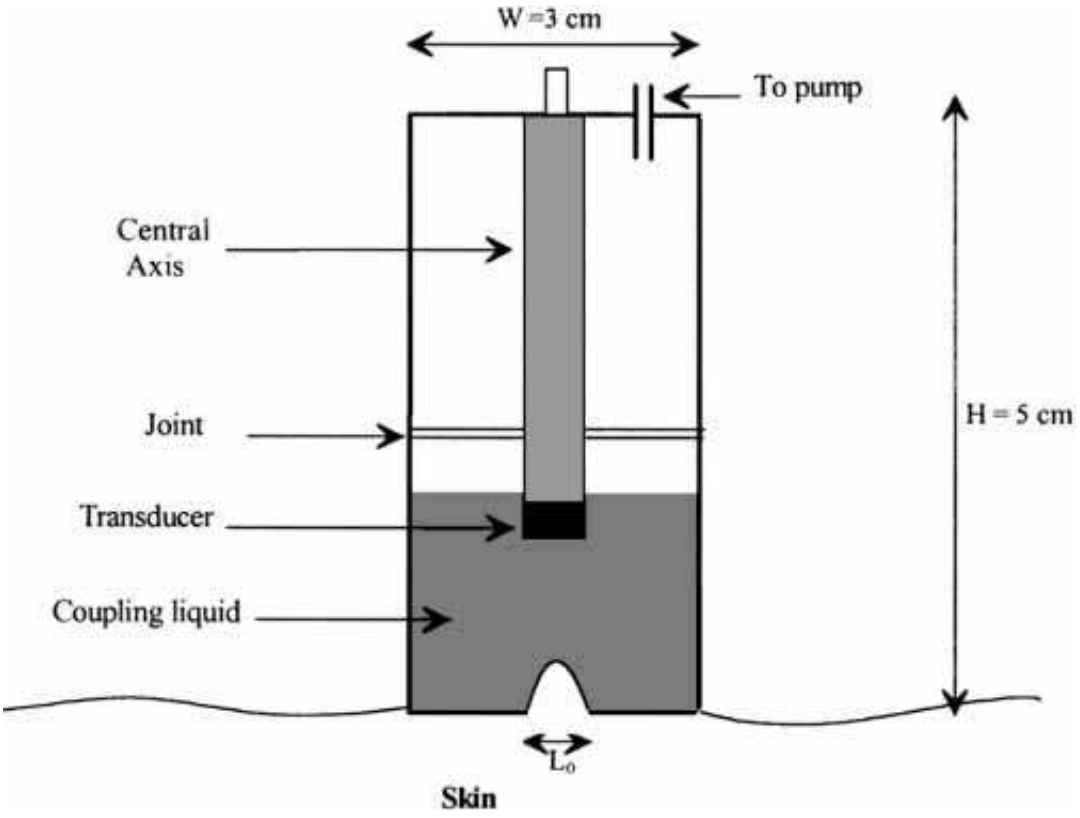

Figure 1.8: The ultrasound aspiration device schematic developed by Diridollou et al., 2000.

In optical methods, the tissue aspiration is observed by a camera, either directly (Fig. 1.7) or using a mirror or prism (Fig. 1.9) : apex height of the aspirated tissue inside the chamber is measured using recorded images. A graph of pressure versus apex height of the aspirated tissue can thus be plotted. Material properties of the tissue are

then identified with these experimental data using inverse methods such as updated FE method [Luboz, Promayon, and Payan, 2014] or gap method [Florentin and Lubineau, 2010]. For example, such aspiration devices have been used to estimate the mechanical properties of cervix [Badir, Bajka, and Mazza, 2013], facial tissues [Luboz, Promayon, and Payan, 2014; Weickenmeier, Jabareen, and Mazza, 2015], brain [Schiavone et al., 2009] or liver [Hollenstein et al., 2009, 2013]. Moreover, performing the tests with different aspiration apertures provides information on the mechanical properties contrasts and in-depth gradient. This potential of the aspiration technique was used for *in-vivo* characterization of multi-layer soft tissues like skin [Weickenmeier, Jabareen, and Mazza, 2015].

A typical example of design evolution is presented by Schiavone et al., 2008, where a light pipette and an external camera were first used. This system was able to meet the required severe sterilization and handling issues imposed during surgery. Yet, using an external camera induced measurements errors due to misalignment. The authors thus designed a two part Light Aspiration device for *in-vivo* Soft TIssue Characterization (LASTIC) [Luboz et al., 2012; Schiavone, Promayon, and Payan, 2010] (Fig. 1.9). The obtained device head was a 3 $cm \times 3$ cm metallic cylinder divided in two compartments with circular aspiration aperture (diameter of 12 mm). The sterilizable lower compartment was a cylindrical chamber made airtight by a glass window in which a negative pressure was applied. A miniature digital camera was fixed inside an upper chamber (not sterilizable) and placed relative to the mirror so as to avoid misalignment errors. This final LASTIC head has yet not been used in intra-operative situations due to its still relative complexity, large weight and large size compared to its aspiration aperture.

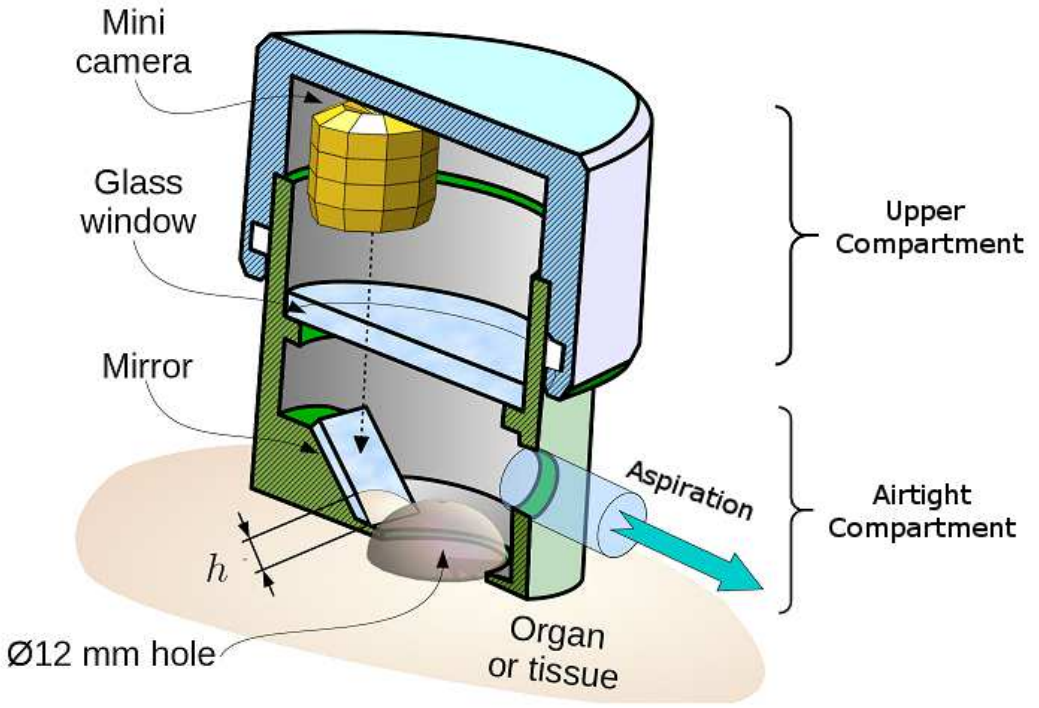

Figure 1.9: Design of LASTIC head and its components [Luboz et al., 2012].

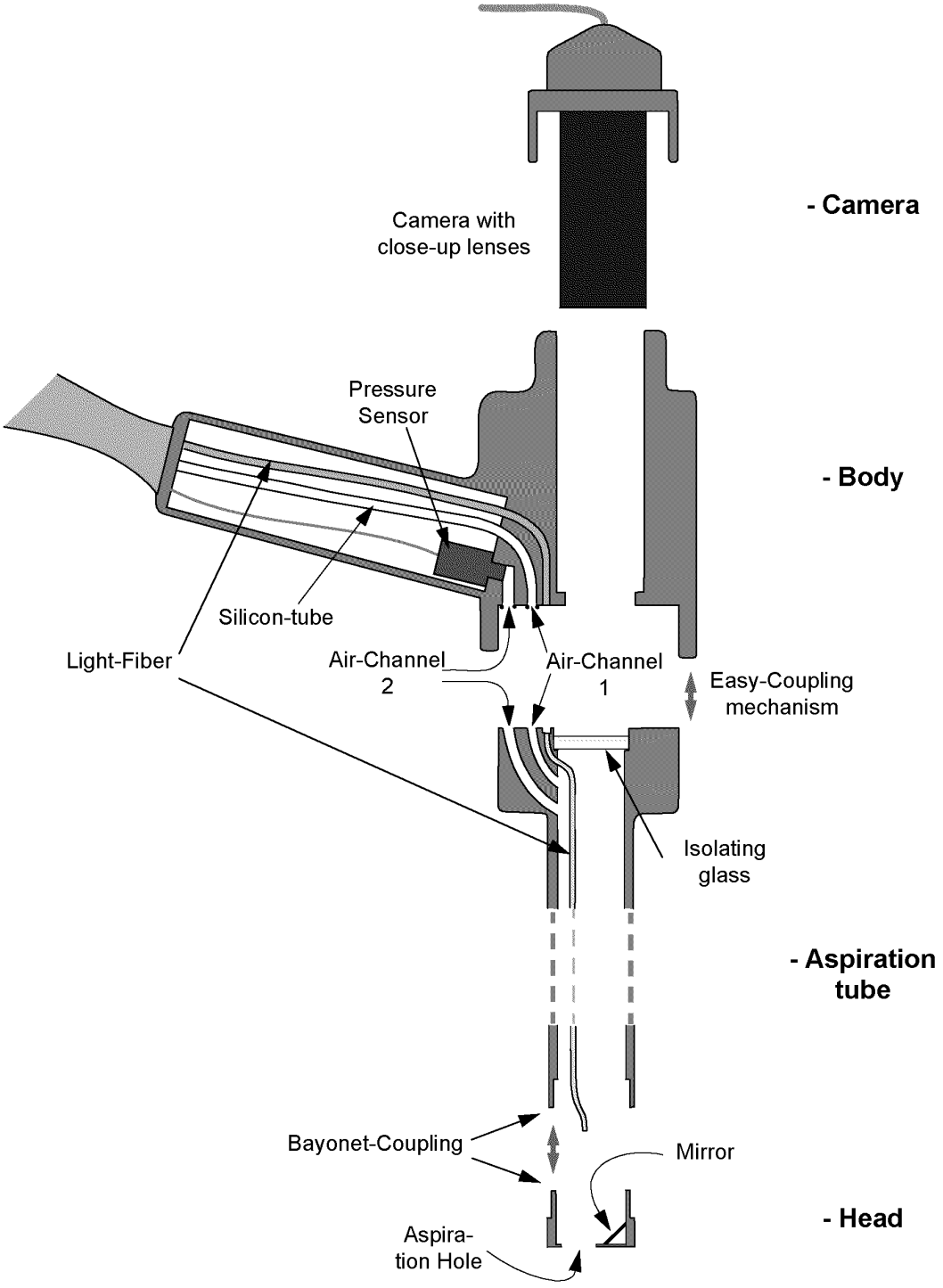

Figure 1.10: Components of the aspiration instrument designed by Vuskovic, 2001.

Another aspiration device was designed by Vuskovic, 2001, where using an optical method lead to a complicated design (Fig. 1.10). As for LASTIC, the silhouette of the aspirated tissue was visible in a mirror mounted beside an aspiration aperture with an angle of 45 degrees relative to the tube pavement. The aspirated tissue height was recorded by a video-camera placed at the top of the aspiration tube. The inside of the

tube was illuminated by an optical fiber. In this device, as for LASTIC, the unsterilizable components were separated from the parts that were in contact with tissue by an isolating glass.

In recent years, this device has been modified and used for *in-vivo* measurement of different human soft tissues' mechanical behavior [Barbarino, Jabareen, and Mazza, 2011; Hollenstein et al., 2009; Nava et al., 2008; Weickenmeier, Jabareen, and Mazza, 2015].

Hollenstein et al., 2013 also developed an aspiration device for application during laparoscopic surgery. This setup was tested and validated under lab-conditions and came then to *in-vivo* operation in order to characterize the mechanical properties of human liver. The optical setup was installed opposite to the pressure sensor (Fig. 1.11) including a stack of lenses, a deflection prism and the image bundle. The field of view was adjusted to capture the aspiration hole and the side view of the aspirated material.

However, these examples of optical aspiration devices and methods present some limitations preventing the generalization of their use in operative rooms:

1. As camera and electronic parts can not go through severe sterilization processes, their contact with tissues must be prevented, which constrained authors to propose complex and large designs, usually using mirrors or prisms [Hollenstein et al., 2013; Kauer et al., 2001; Luboz, Promayon, and Payan, 2014; Luboz et al., 2012; Nava et al., 2008; Schiavone et al., 2008; Schiavone et al., 2009; Schiavone, Promayon, and Payan, 2010; Weickenmeier, Jabareen, and Mazza, 2015].

2. The use of cameras and mirrors requires accurate relative positioning, which lead to designing systems that are large and rigid [Nava et al., 2008; Schiavone, Promayon, and Payan, 2010].

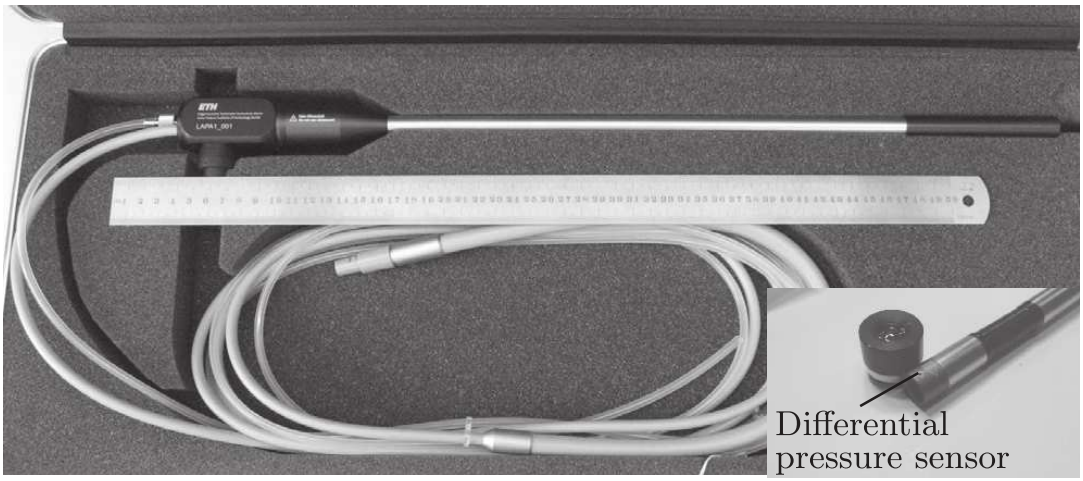

Figure 1.11: The laparoscopic aspiration probe connected to the silicone tubing at the handle. The location of the differential pressure sensor is indicated on the probe head [Hollenstein et al., 2013].

A possible solution was proposed by Badir, Bajka, and Mazza, 2013, where the authors used a mechanical stop in order to measure the aspirated tissue height (Fig. 1.12).

With progressive vacuum increase inside the aspiration chamber, the tissue was sucked into the tube and formed a nearly spherical cup. Once the apex of the cup reached four millimeters into the aspiration chamber, it closed the thin pipe used to aspirate the tissue. This provided a safe, displacement controlled end-point of the experiment. The instrument was used to measure the mechanical properties of the uterine cervix during pregnancy. A camera and glass fibers (for lighting) were located in the device aspiration chamber to facilitate the placement of the aspiration aperture on the cervix. The extracted information from the camera was not used to quantify the tissue deformation.

Still, the mechanical stop method provides data for a unique point, which might decrease the accuracy because of possible experimental errors.

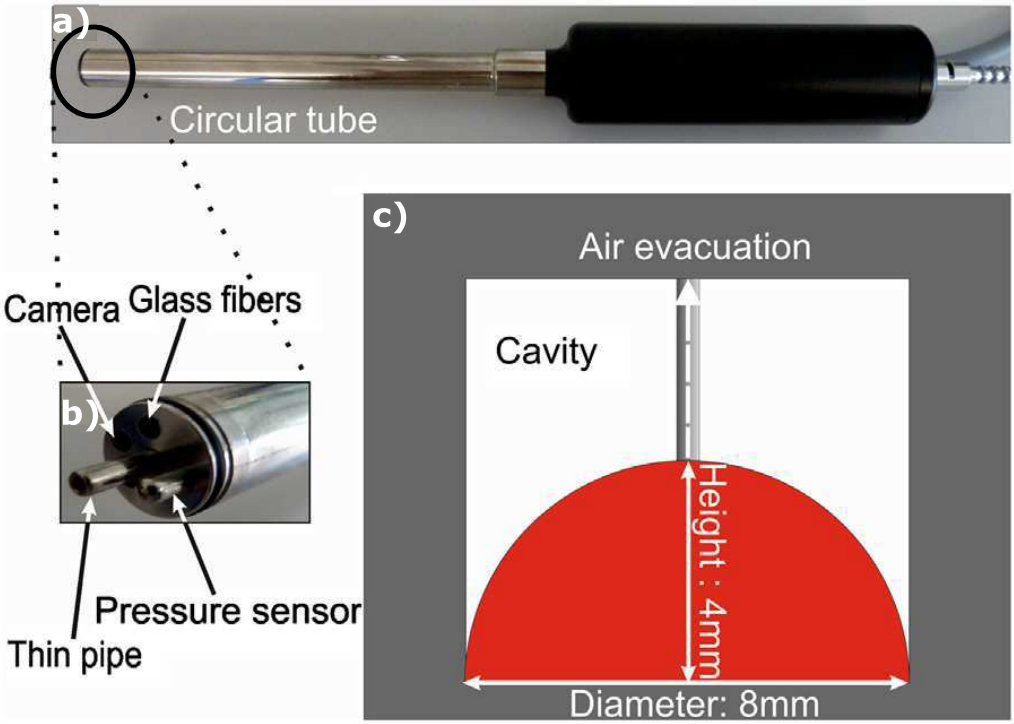

Figure 1.12: a) The proposed aspiration device by Badir, Bajka, and Mazza, 2013, b) the integrated camera, glass fiber and pressure sensor are placed within the tube, and c) schematic of the aspirated tissue which forms a nearly spherical cup until it touches and closes the thin pipe.

1.4.5 Practical conclusion

Among all the proposed methods for *in-vivo* mechanical characterization of soft tissues, aspiration/suction is the most widely used technique due to its simplicity and robustness. Several commercial aspiration devices are designed for dermatology market (*e.g.* Cutometer from Courage and Khazaka, Germany, or Dermaflex from Cortex Technology, Denmark).

In particular, aspiration method limits relative displacement of the tissues in relation with the device, which is one of the most important limitation in the other methods.

In this work, the aspiration technique is used for the experimental measurements because of its advantages and simplicity in comparison with the other methods. To over-

come the limitations provided by the previous aspiration devices, a new method based on the measurement of the aspirated tissue volume is proposed and evaluated. In addition, the capability of this technique for measuring the in-depth mechanical behavior gradient of the tissues is used to propose a method for multi-layer soft tissues identification.

1.5 Structures of the biological soft tissues

Biomechanicians are looking for realistic estimations of soft tissues deformations. The first step in this regard is an accurate modeling of these heterogeneous complex structures. Thus, it seems crucial to have a basic knowledge about multi-layer structures of biological soft tissues.

Human soft organs can be divided into two groups: "internal"organs, like the liver or the brain, and "external"organs, like the skin or the breast. To characterize internal organs intra-operative experiments should be performed. This adds some limitations to the experimental procedure in regards with the measurement duration, the instrument sterilization, as well as its size and design. In contrast with the internal organs, external tissues are more accessible. Measuring their behavior therefore adds fewer limitations to the experimental procedure. As a consequence, the material properties of human skin have been characterized with several experimental methods [Agache et al., 1980; Finlay, 1971; Flynn, Taberner, and Nielsen, 2011a,c; Hendriks et al., 2006b; Veronda and Westmann, 1970; Vexler, Polyansky, and Gorodetsky, 1999; Xu and Yang, 2015].

Since the skin will be the first organ studied with our new aspiration device in a near future, its anatomical description is provided in this section.

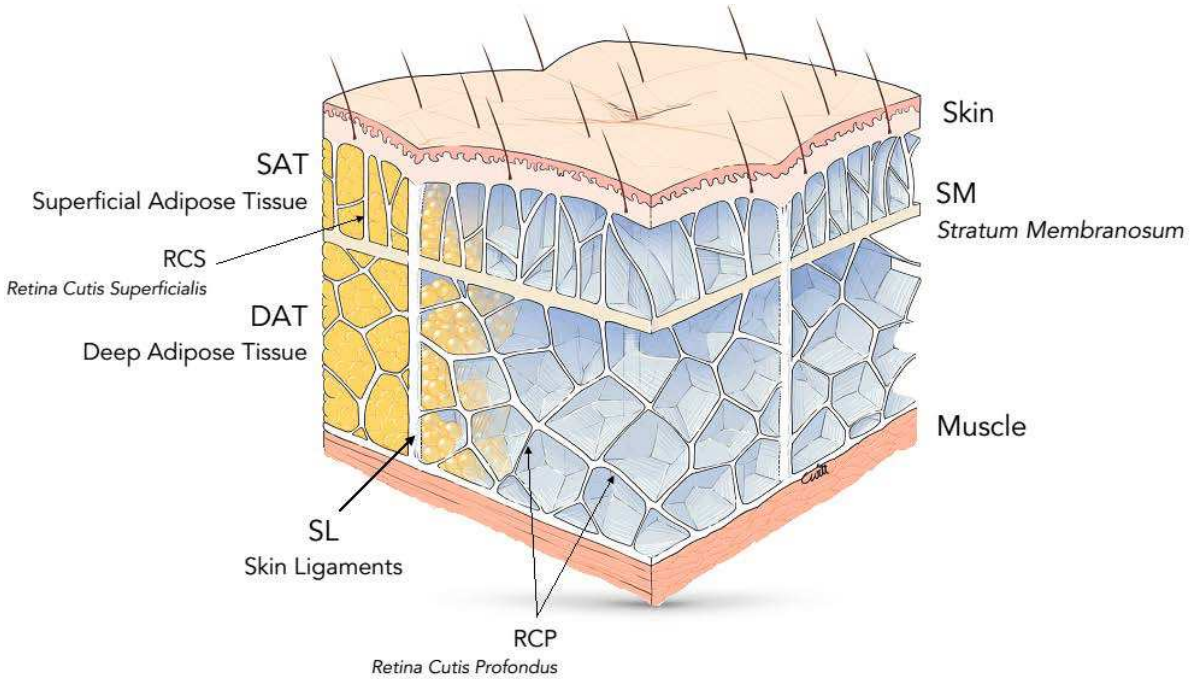

Figure 1.13: Generic model of the skin and subcutaneous complex with all the substructures [Herlin et al., 2014].

The generic anatomical model of the human skin and subcutaneous complex organization, as proposed by Herlin et al., 2014, can be summarized into a multi-layered model, which combines the following substructures (Fig. 1.13):

- Skin which has a multicomponent micro-structure. The basic elements of the skin are: networks of collagen, elastic and nerve fibers, small blood vessels and lymphatics, covered by a layer of epithelium and transfixed at intervals by hairs and the ducts of sweat glands [Kenedi et al., 1975].
- Superficial Adipose Tissue (SAT) consisting of fat lobules with variable sizes.
- Retinacula Cutis Superficialis (RCS) formed by the septal densifications lobules of the SAT.
- Stratum Membranosum (SM) that can be either fibrous and/or muscular and either single or multiple.
- Deep Adipose Tissue (DAT) composed of polyhedral fat lobules, as in a honeycomb arranged more randomly than in the SAT.
- Retinacula Cutis Profondus (RCP) formed by the septal densifications lobules of the DAT.
- Skin Ligaments (SL), which are a particular specialization of RCS and RCP.
- Deep Layer which is the inferior limit of the skin and subcutaneous complex. This may be muscle, aponeursosis or periosteum.

In multi-layered tissues (like the skin), the individual layers have distinct mechanical properties that influence the overall mechanical behavior [Flynn, Taberner, and Nielsen, 2011b; Herlin et al., 2014; Xu and Yang, 2015; Zhao, Sider, and Simmons, 2011]. Hence, it seems to be important to take the layered inhomogeneity of the tissues into account, which is one of the goals of our work (Chapter 4).

1.6 Conclusion

This chapter briefly presented the various experimental approaches to *in-vivo* characterize the mechanical properties of biological soft tissues. The aspiration method was selected for the experimental measurements in this study due to its simplicity and accuracy in comparison with the other methods.

According to the literature, the current aspiration devices still have some limitations, such as sterilization problems that prevent their general use for intra-operative measurements. In particular, the complicated designs of these instruments limit the use of different aspiration aperture diameters for the same device in order to for instance test the organs with different sizes, *etc.*

In this thesis, a new volume-based aspiration device is introduced which does not have the limitations raised above and which provides the same level of accuracy (Chapter 2). The characterization method using the new device is validated on synthetic materials (Chapter 3). As mentioned earlier in this chapter, the biological soft tissues like the skin

are often complex multi-layered structures. This work introduces a novel method, based on our volume-based aspiration device, for the in-depth mechanical characterization of soft tissues (Chapter 4). Eventually, a real-time identification is enabled by introducing in Chapter 5 a design of experiments method for inverse characterization of the tissues based on the aspiration tests.

CHAPTER

TWO

DISPOSABLE SYSTEM FOR IN-VIVO MECHANICAL CHARACTERIZATION OF SOFT TISSUES BASED ON VOLUME MEASUREMENT

Some parts of this chapter have been published and can be found in the following reference

- ***SA. Elahi, N. Connesson, Y. Payan****, 2018, Disposable system for in-vivo mechanical characterization of soft tissues based on volume measurement, J. Mech. Med. Biol.*

2.1 Introduction

As it was stated in Chapter 1, the existing aspiration devices have some limitations regarding their complicated designs and sterilization processes for intra-operative applications. This chapter introduces a new aspiration method based on the measurement of the aspirated volume. The idea consists in replacing the apex height optical measurement in the existing aspiration devices by the measurement of the aspirated tissue volume. Such a change in the method enables the removal of any camera, mirror and electronic part from the system head that is basically reduced to a simple aperture and is thus able to meet the required severe sterilizations. The proposed system is thus probably among the simplest, lightest and most inexpensive that one could achieve. Hopefully, simplifying the system will enable a generalized use of the device.

Switching the input data from apex height to volume measurement will only slightly change the inverse method process: both the apex height and the aspirated tissue volume are directly related to the aspirated tissue surface shape. The mechanical properties thus identified with either input data rely on the same hypotheses (boundary conditions, material thickness, stiffness and anisotropy, mechanical properties gradients due to different layers, *etc.*) and will provide similar results. The inverse identification method is beyond the scope of this chapter and will be presented in the next chapters.

Eventually, only differences in the input data signal-to-noise ratio can significantly impact the inverse analyses. The main question to deal with is then to assess if the experimental volume measurements signal-to-noise ratio obtained optically or with the new proposed method are comparable: is there a loss of measurement precision while

changing of measurement mean? This question will be answered experimentally in this chapter by comparing volume measurements obtained either optically or with the proposed method.

The measurement method based on the aspirated volume is first thoroughly presented (section 2.2). This method is then compared with a specifically designed reference method and then with more classical optical measurements (sections 2.3 and 2.4). The results obtained with each setup are then analyzed with a particular attention to reproducibility, error, measurement standard deviation (section 2.5), and impact of different setup experimental parameters (section 2.6). Finally, some recommendations are provided to help users to obtain the same results quality (section 2.7).

2.2 Proposed volume measurement method

During *in-situ* and *in-vivo* tests, the proposed new system is simply composed of a syringe pump, a manometer and an aspiration chamber (Fig. 2.1).

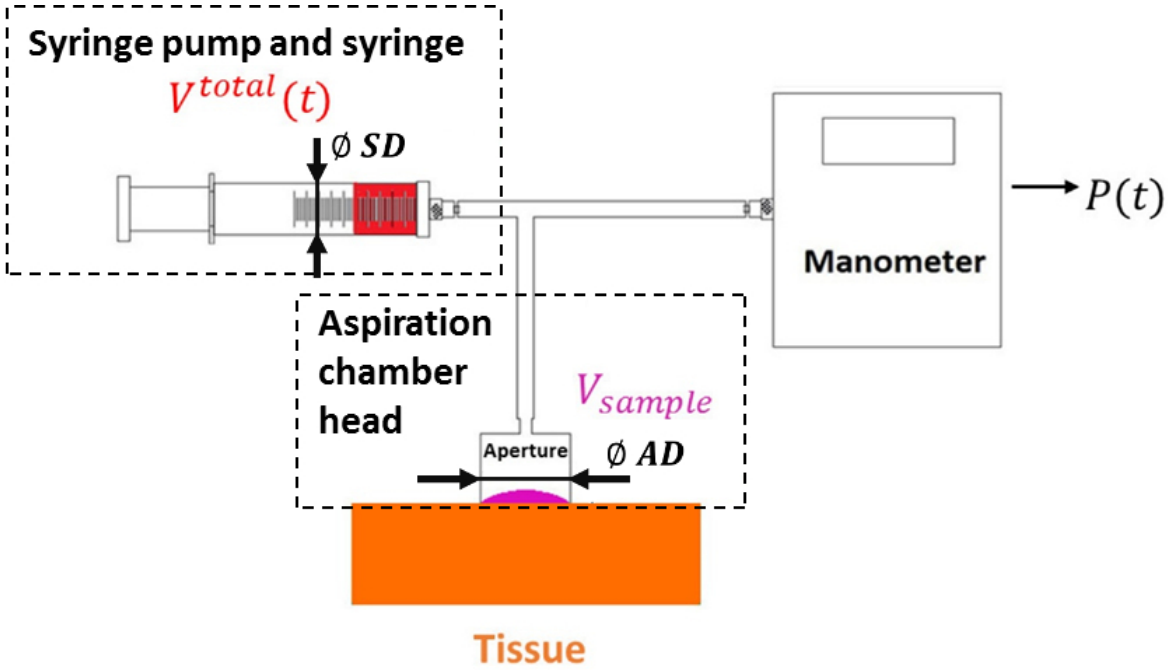

Figure 2.1: Measurement principle of the proposed volume measurement method.

The volume removed by the syringe pump V^{total} and the associated pressure P are measured during the test. Yet, the volume removed by the syringe pump V^{total} is obviously different from the tissue volume V_{sample}: this difference is mainly due to volume changes in the system because of the applied pressure; the system volume V_{system} is compressible due to air expansion and elasticity of the components (connections, tubes, syringe, *etc.*). The total removed volume V^{total} can therefore be seen as the sum of the aspirated tissue volume V^{RB}_{sample} and the volume changes due to system compressibility V_{system}:

$$V^{total}(P) = V^{RB}_{sample}(P) + V_{system}(P) \tag{2.1}$$

The system volume function $V_{system}(P)$ is experimentally assessed during a second step by testing an undeformable material, referred to as rigid test: in this experimental configuration the aspirated tissue volume V_{sample}^{RB} remains zero and the system volume compressibility V_{system} can be directly measured using Eq. 2.1:

$$V_{system}(P) = V_{rigid}^{total}(P) \tag{2.2}$$

Combining the system volume V_{system} (Eq. 2.2) and Eq. 2.1, the aspirated tissue volume V_{sample}^{RB} can thus naturally be estimated by:

$$V_{sample}^{RB}(P) = V^{total}(P) - V_{system}(P) \tag{2.3}$$

When applying the rate-based volume measurement method V_{sample}^{RB} during *in-vivo* experiments, the total volume V^{total} will be measured first, using a sterilized aspiration head. The rigid test will be performed afterward, when sterilized conditions are no longer required. During this test, a clamp system can be used to avoid leakage between the aspiration head and the undeformable material. Performing this additional rigid test adds less than 5 minutes to the overall procedure.

2.3 Performance assessment test-bench

As the aim of this work is to compare optical and rate-based volume measurement signal-to-noise ratio, all results should be compared with a reference obtained in identical conditions. Three different methods and associated volume measurements will thus be performed on the same material:

1. the proposed rate-based volume measurement method V_{sample}^{RB} (section 2.3.1),
2. a reference method $V_{sample}^{reference}$ (section 2.3.2),
3. and a camera based method V_{sample}^{camera} (section 2.3.3).

In this work, it has been chosen to perform these three measurements simultaneously on the same test material. As no inverse characterization will be performed here, the tested material is not required to be known or to mimic accurately the tissue mechanical behavior, but only to provide a sufficient shape variation (flat to a half sphere in this case) for a pressure range of the order of magnitude observed during actual tissue mechanical characterization: the tests have been performed in a range of 0 to 50 mbars, which is approximately the range obtained while characterizing *in-vivo* lower lip tissues [Luboz, Promayon, and Payan, 2014].

In the performance assessment configuration, the tissue has thus been replaced with a soft thin membrane cut from a latex glove (Fig. 2.2). This membrane has been glued to a system providing the reference volume $V_{sample}^{reference}$ (section 2.3.2). A camera has been used to take pictures of the aspirated membrane during the tests and to deduce the aspirated volume V_{sample}^{camera} (section 2.3.3).

The results will thus provide the signal-to-noise ratio of the rate-based volume measurement method V_{sample}^{RB} and classic optical method V_{sample}^{camera} by using the reference volume $V_{sample}^{reference}$.

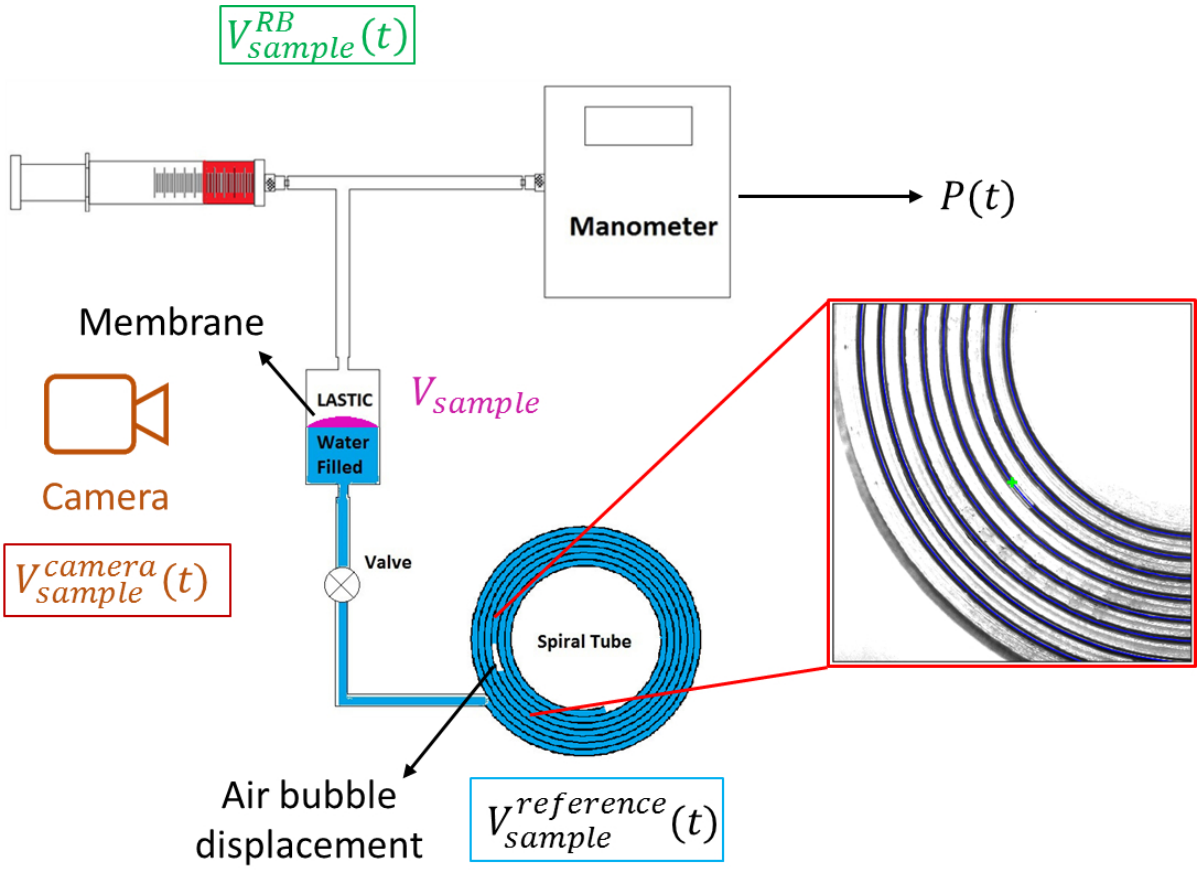

Figure 2.2: Performance assessment configuration: simultaneous measurement of the aspirated tissue volume using the 3 methods: the reference method $V_{sample}^{reference}$, the rate-based method V_{sample}^{RB} and the camera method V_{sample}^{camera}.

2.3.1 Rate-based volume measurement method

The method previously presented is directly applied (section 2.3.1). In particular, the rigid test in this test configuration is performed by closing the valve in the setup (Fig. 2.2), so that the contribution of the aspirated tissue volume is zero during the rigid test.

2.3.2 Reference volume measurement

A reference volume measurement device has been developed to estimate measurement errors (Fig. 2.2). Such a device obviously will not be used in practical cases.

This device, glued to a membrane, simply consists in a thin tube filled with water where an air bubble has been inserted (Fig. 2.3). Any movement of the membrane will induce movements of both the water and the bubble. Knowing the tube section S and the bubble displacement ΔL straightforwardly provides the "tissue" aspirated volume $V_{sample}^{reference}$:

$$V_{sample}^{reference} = S\Delta L \tag{2.4}$$

The bubble movements ΔL have been tracked on pictures synchronized with the pressure measurement. A dark background and proper lighting have been used to help

automated bubble position tracking.

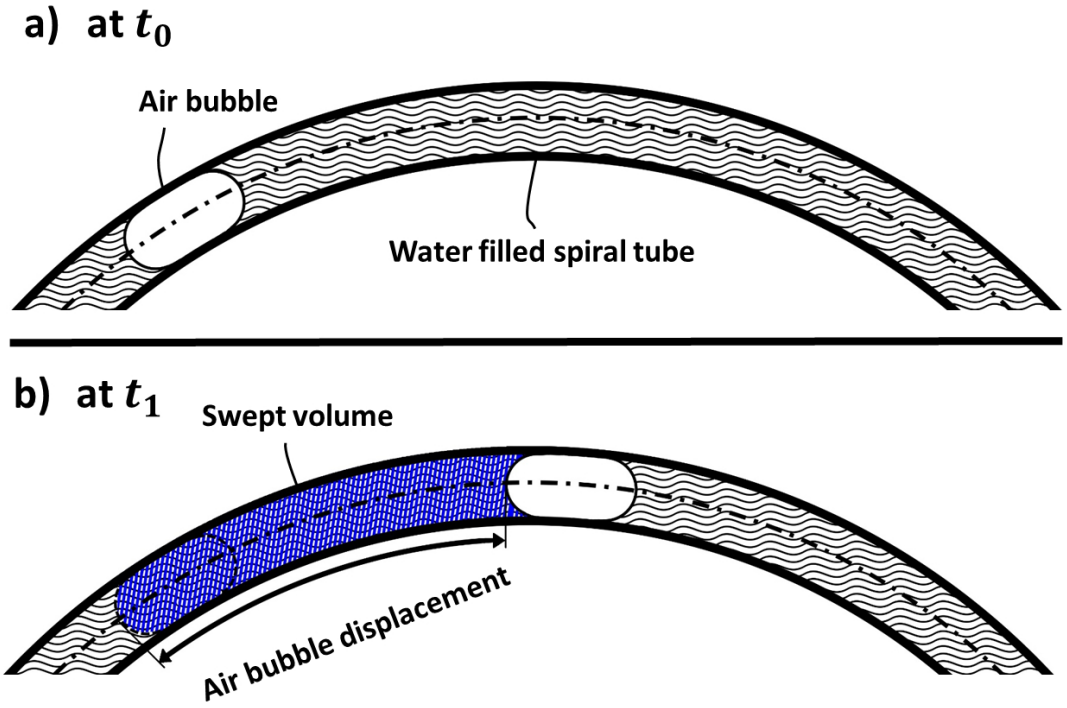

Figure 2.3: Air bubble inside the spiral tube a) before and b) after the aspiration process.

2.3.3 Camera volume measurement method

The proposed rate-based method V_{sample}^{RB} should be compared to an optical based method V_{sample}^{camera} even if the measurements using camera will not be necessary to apply the proposed method. For this, a camera has been used to take pictures of the aspirated membrane shape $h(r)$ during the test (Fig. 2.4). Computing the associated volume can be easily performed by:

$$V_{sample}^{camera} = \pi \int_{-R}^{R} rh(r)dr \tag{2.5}$$

where r is the radius of any point M of the aspirated surface, dr is an elementary radius, h is the membrane height above point M, and R is the aperture internal radius (Fig. 2.4c).

A dark background and proper lighting have been used to help automated membrane shape $h(r)$ recognition. According to Fig. 2.4b, some irregularities are visible in the lower part of the initial picture, which are due to the glue between the membrane and the aspiration chamber. The erroneous additional volume induced by these extra white parts is simply removed by subtracting the estimated volume of the initial picture from all other volumes during the aspiration.

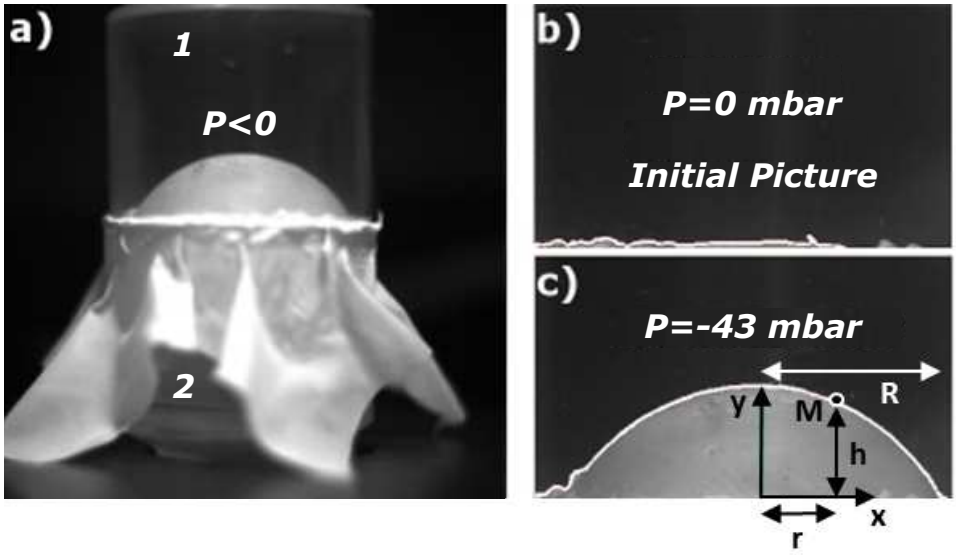

Figure 2.4: a) Global view of the aspiration chamber: (1) aspiration head and (2) reference measurement system and pictures used to measure the aspirated volume V_{sample}^{camera} b) before and c) during aspiration.

2.4 Preliminary results and parameters definition

2.4.1 Preliminary results

An example of typical results obtained simultaneously by the three methods is presented as pressure P versus volume curves (Fig. 2.5).

Curves 1 to 3 are obtained using the rate-based volume measurement method V_{sample}^{RB} with a rate of $0.4ml/min$, which proved to be small enough to provide quasi-static mechanical behavior:

- the total volume $V^{total}(P)$ obtained with the syringe pump while aspirating the membrane is presented as Curve 2 (Eq. 2.1)
- the measurement obtained during rigid test $V_{rigid}^{total}(P)$, valve closed, is presented as Curve 1 (Eq. 2.2). This volume variation is mainly due to the volume variation of air but also to the polyurethane tubes connecting the aspiration head, syringe pump and manometer. Special attention has been made to prevent any possible leakage in the connection zones.
- the sought volume V_{sample}^{RB} (Curve 3) is the result of the difference of the two previous curves (Eq. 2.3).

Curves 4 and 5 are obtained using the reference $V_{sample}^{reference}$ and camera based methods V_{sample}^{camera}, respectively (Eq. 2.4 and 2.5, respectively). It should be specified here that the reference measurement system has been built using a tube of internal diameter of $0.9mm$ to increase the bubble movement sensitivity. The bubble position has been estimated with a precision of about $\pm 1mm$; the reference volume $V_{sample}^{reference}$ variations are thus measured with an accuracy of about $\pm 0.64\mu l$.

These preliminary tests underline that all three pressure P versus volume curves (V_{sample}^{RB}, $V_{sample}^{reference}$, V_{sample}^{camera}) are very similar, validating thus the three proposed methods. The signal-to-noise ratio of each method needs now to be estimated, which will be presented in section 2.6.

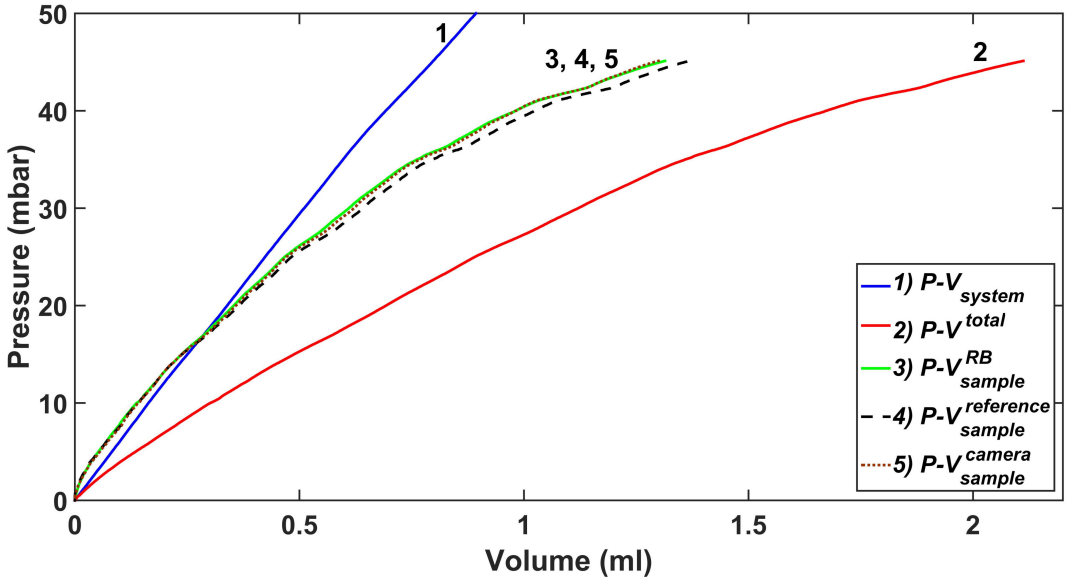

Figure 2.5: Pressure versus volume for each experiment.

2.4.2 Parameter definition and experimental design

The signal-to-noise ratio of the rate-based volume method depends on the inner aspiration Aperture Diameter (AD) and the Syringe Diameter (SD) associated to the syringe pump (Fig. 2.1). Tests have thus been performed for two different inner Aperture Diameters (AD) and three different Syringe Diameters (SD). Therefore, 6 groups of tests have been conducted. Syringe and aperture inner diameters for the 6 test groups have been summarized in table 2.1. As the camera volume measurements V_{sample}^{camera} depends only on the chosen Aperture Diameters (AD), only two measurement sets are required to perform the signal-to-noise ratio study on the camera volume measurements.

Table 2.1: Characteristics of different test groups and the used measurement methods in each group

Test groups	AD (mm)	SD (mm)	Performed volume measurement method		
			$V_{sample}^{reference}$	V_{sample}^{RB}	V_{sample}^{camera}
VT-1	21.0	21.0	✓	✓	✓
VT-2	21.0	12.9	✓	✓	no data
VT-3	21.0	4.6	✓	✓	no data
VT-4	12.9	21.0	✓	✓	✓
VT-5	12.9	12.9	✓	✓	no data
VT-6	12.9	4.6	✓	✓	no data

2.5 Error measurement tests

In order to estimate the error of the method, the 6 test groups (table 1) have been repeated 9 times. Diagrams of pressure P versus measured aspirated volume using rate-based V_{sample}^{RB}, reference $V_{sample}^{reference}$ and camera V_{sample}^{camera} methods for the 9 repetitions of test group VT-1 are presented in Fig. 2.6 as an example of raw data. The results show mechanical behavior differences for these successive tests, but, for each particular test, the three methods provide very similar results. This underlines that the rate-based method is able to monitor the lack of the chosen latex membrane mechanical reproducibility (attributed here to the complex local loading history and latex non linear behavior): the measurement error is lower than the mechanical behavior variations between tests.

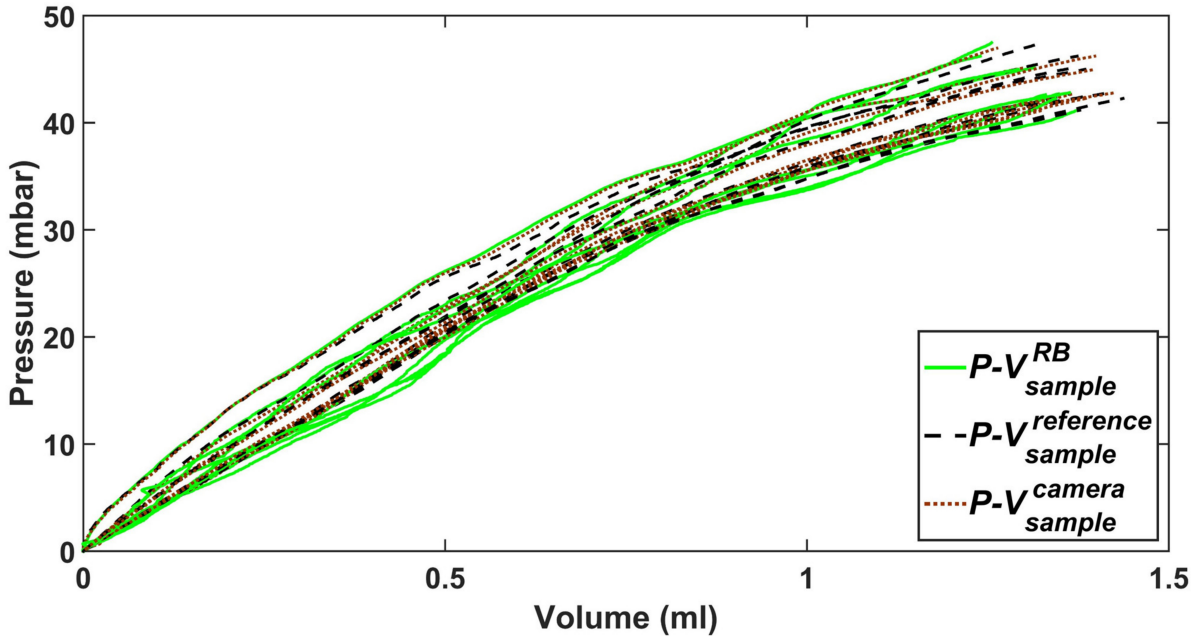

Figure 2.6: Comparison of 9 diagrams of pressure P versus measured aspirated volume using rate-based V_{sample}^{RB}, reference $V_{sample}^{reference}$ and camera V_{sample}^{camera} methods for the test group VT-1.

The errors of the rate-based volume measurement V_{sample}^{RB} and of the camera V_{sample}^{camera} methods have been computed using the reference volume $V_{sample}^{reference}$. Such errors are thus defined as:

$$Error^{RB}(P) = V_{sample}^{RB}(P) - V_{sample}^{reference}(P) \tag{2.6}$$

$$Error^{camera}(P) = V_{sample}^{camera}(P) - V_{sample}^{reference}(P) \tag{2.7}$$

For example, the experimental results of Eq. 2.6 ($Error^{RB}$) for test group VT-1 are presented versus pressure P in Fig. 2.7. In addition, the associated STandard Deviations (STD) and average of volume measurements errors $Error^{RB}$ have been reported as three thick black lines (average and average$\pm 2STD$, Fig. 2.7). The two curves average$\pm 2STD$ will be referred to as envelope curves in the following.

The same results have been obtained on each test group (table 1) but are not presented here for conciseness.

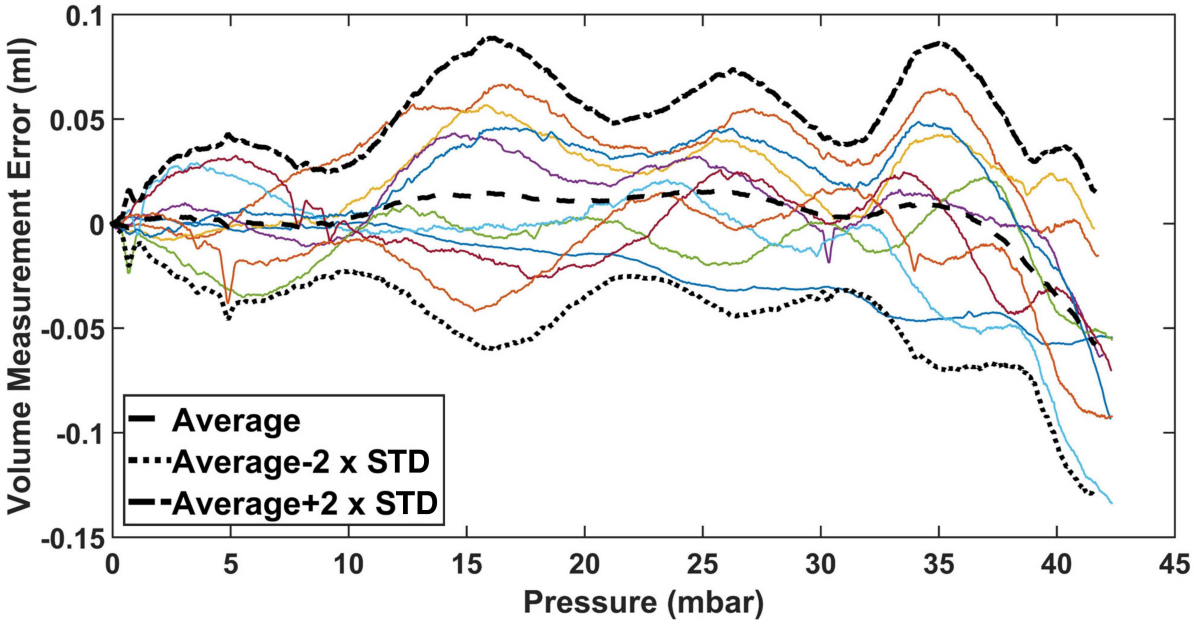

Figure 2.7: Comparison of 9 diagrams of rate-based errors $Error^{RB}$, their average and STD for test group VT-1.

2.6 Results and discussion

In this section the two volume measurement errors $Error^{RB}$ and $Error^{camera}$ have been analyzed and compared: averages and standard deviations of the errors have been represented for all the test groups (table 1) in two different categories:

1. Tests with the same aspiration Aperture Diameter (AD, Section 2.6.1).

2. Tests with the same Syringe Diameter (SD, Section 2.6.2).

2.6.1 Tests with the same aspiration Aperture Diameter (AD)

Rate-based results

The rate-based volume error $Error^{RB}$ for each test group with the same aperture diameter has been presented using only their envelope curves in Figs. 2.8a (AD=21mm) and 10b (AD=12.9mm). Theses results underline:

- The average rate-based errors $Error^{RB}$ are oscillating around zero (no measurement bias) for both aspiration Aperture Diameters AD.

- The standard deviation of measurements errors can be reduced by choosing a smaller Syringe Diameter SD.

It could also be underlined here that decreasing the Syringe Diameter SD diminishes the maximal aspirated volume V^{total} out of the system (Fig. 2.1) and consequently reduces the maximal pressure range.

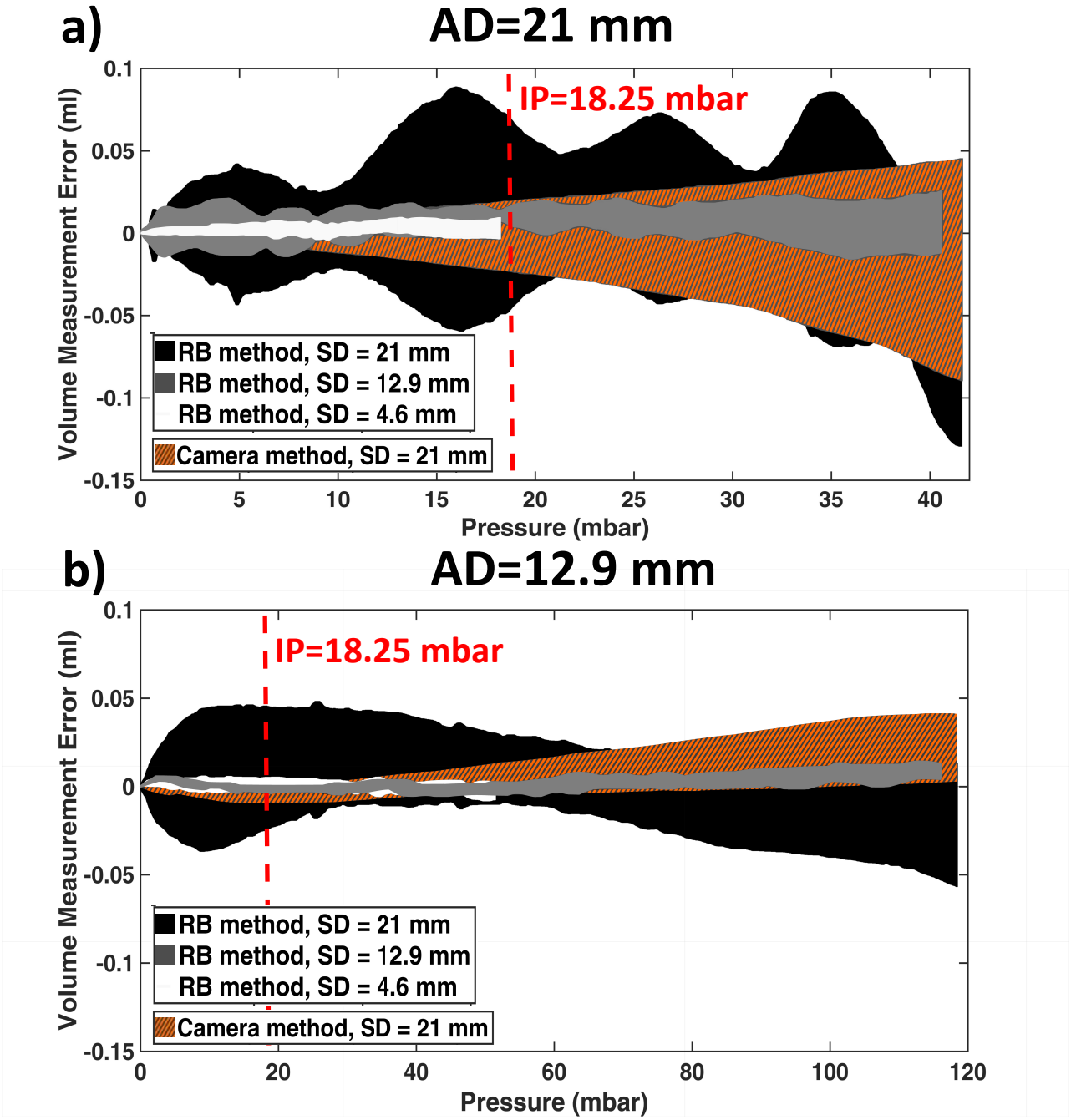

Figure 2.8: Envelope curves of volume measurement errors ($Error^{RB}$ and $Error^{camera}$) versus pressure P for the tests with different Syringe Diameters SD and aspiration Aperture Diameters AD = a) $21mm$ and b) $12.9mm$.

Optical results

The envelope curves of the optical volume errors $Error^{camera}$ are presented for each of the aspiration Aperture Diameter AD= $21mm$ and $12.9mm$ (hatched areas in Figs. 2.8a and b, respectively).

- The standard deviation of camera measurements errors increases with the pressure level and is of the same order of magnitude as the rate-based volume error $Error^{RB}$.

It yet should be underlined here that by properly choosing the Syringe Diameter SD, the rate-based method can provide more accurate results than the optical method. This observation will encourage the use of the rate-based method rather than the optical method thanks to its simplicity and accuracy.

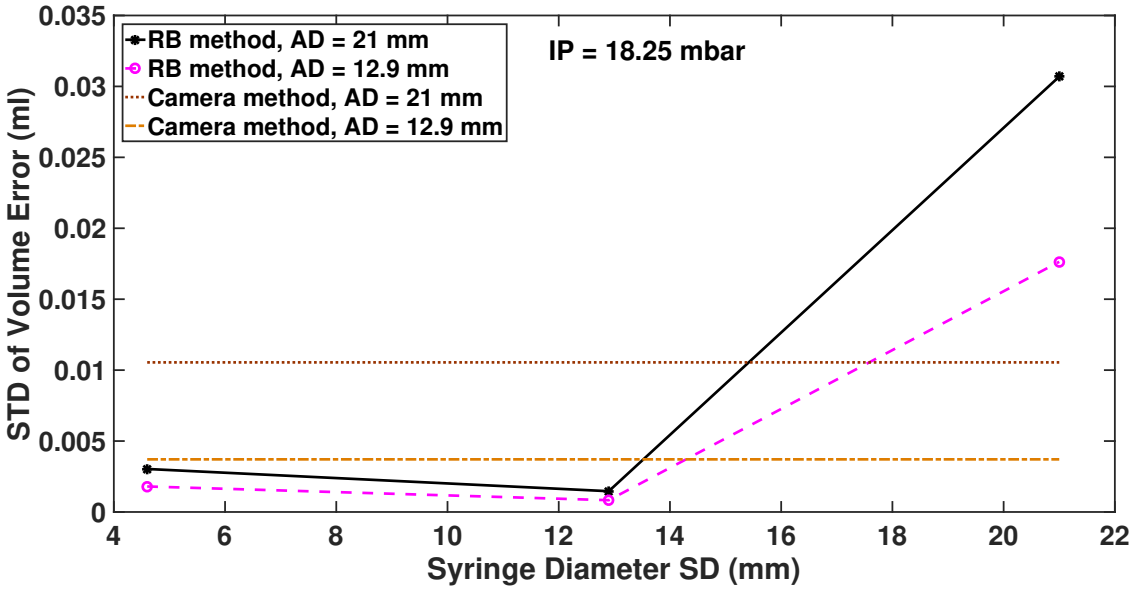

Figure 2.9: STD of volume measurement errors ($Error^{RB}$ and $Error^{camera}$) versus SD for the tests with various AD at Iso Pressure (IP).

Results comparison

To compare the methods accuracy more fairly, the results have been evaluated at a the pressure (IP) of $18.25mbar$ (red vertical dashed line, Figs. 2.8a and b), which is the maximal pressure for which data is available for all the different tests. The extracted standard deviations at IP are presented as functions of the Syringe Diameter SD (Fig. 2.9). As previously mentioned, it can be underlined that: decreasing the Syringe Diameter SD reduces the error standard deviation. In particular, the Syringe Diameter SD can be chosen so as to obtain smaller errors than with the optical method. This conclusion is independent of the chosen aspiration aperture diameter or chosen pressure IP.

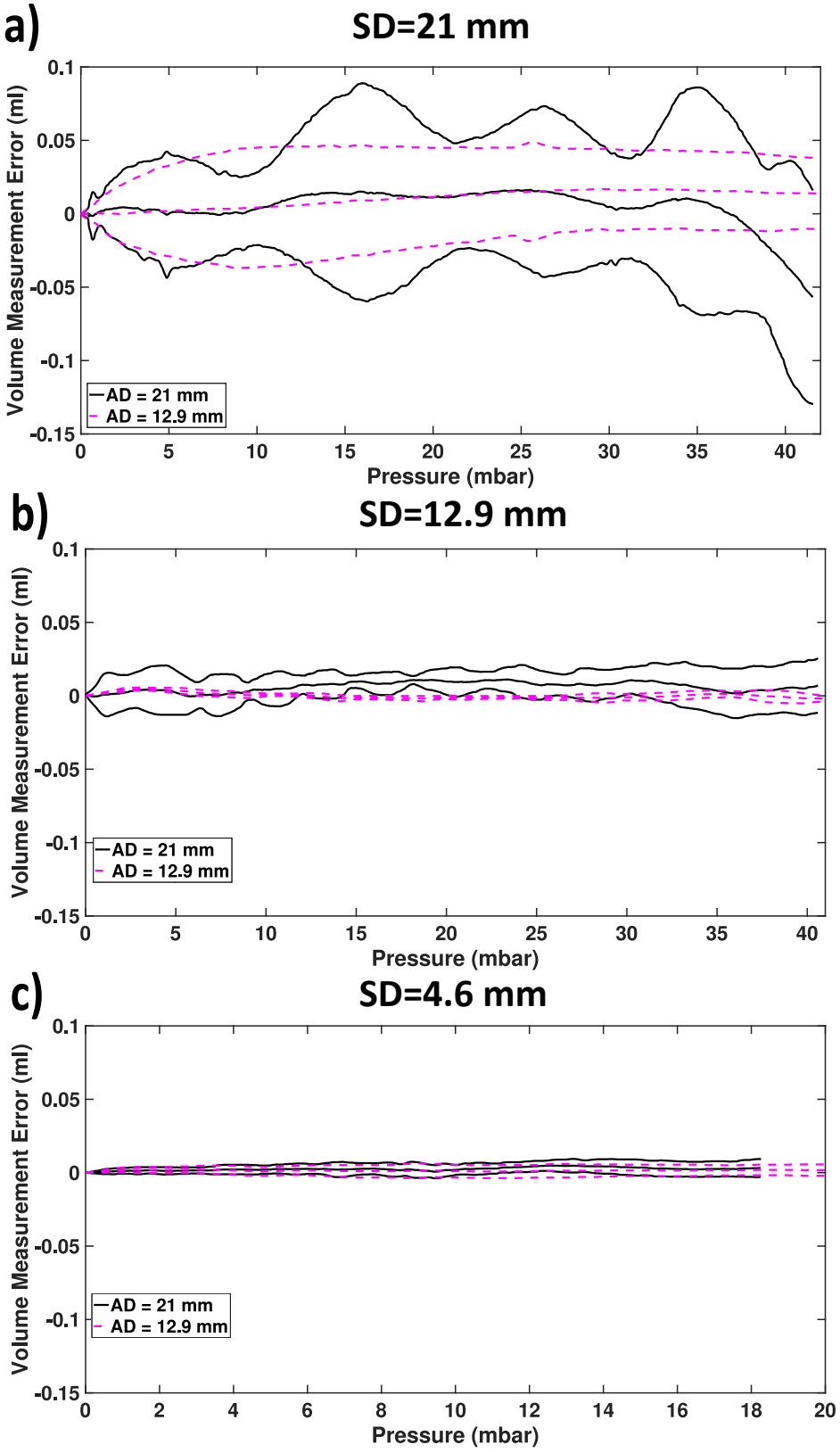

Figure 2.10: Rate-based error $Error^{RB}$ (average and average$\pm 2\times$STD) versus pressure P for AD = 12.9 and $21mm$ with SD = a) $21mm$, b) $12.9mm$ and c) $4.6mm$.

2.6.2 Tests with the same Syringe Diameter (SD)

It has been underlined previously that the rate-based measurement errors mainly depend on the Syringe Diameter SD. To emphasize the impact of the aspiration Aperture Diameter AD on the errors, the results have also been studied for similar syringe diameters (Figs. 2.10a to c). In each graph, the observed error curves are of the same order of magnitude whatever the Aperture Diameter AD value is. The aspiration Aperture Diameter AD has thus almost no impact on the error of the rate-based volume measurement method $Error^{RB}$. The aspiration aperture diameter can thus be chosen by taking into account only criteria as space constraints or required depth analyze.

2.7 User recommendations

To apply the rate-based volume measurement method V^{RB}_{sample}, a user should take into account the following considerations:

- Pay a special attention to prevent any leakage in both main and rigid tests. Before any test, applying an initial small negative pressure (in range of $1mbar$) and checking the pressure stability would be advisable. This initial pressure should be very small compared to the measurements pressure range. Special fixture apparatus should be design to perform the rigid test, using, for example, a caoutchouc surface clamped on the aspiration aperture.

- To avoid potential effects of the temperature on the error, the main and rigid tests should be performed in the same environment and within a short interval.

- If sterilized conditions are required during the actual test, the rigid body test should be performed after the main test to avoid any possible system contamination.

- Too high volume rate applied by the syringe pump can be a source of error due to viscoelastic behavior of either tissue or system: low enough volume rate should thus be used. Such a volume rate can be partially estimated during rigid tests performed before sterilization and by insuring that the volume rate has no effect on the obtained function $V^{total}_{rigid}(P)$. In this work, a volume rate of $0.4\ ml/min$ has been selected. The same method can be applied while testing the material with equal or lower volume rate to ensure its behavior is rate independent. The presented methods and systems could also be used to estimate viscoelastic properties of materials, but this aspect is beyond the scope of this work.

2.8 Conclusion

In this chapter, an original method based on volume measurement was developed and validated to perform aspiration tests on soft living tissues. Unlike previous aspiration devices, this method does not require the presence of camera, mirror, or any electronic part. It thus enables designing simpler, lighter, smaller and easily sterilizable systems compared to the previous proposed systems. The simple design of the new device enables the user to choose the aspiration aperture diameter and shape according to the test needs.

In particular, the proposed method requires two measurement steps: (1) measuring the system+tissue behavior and (2) measuring only the system behavior during a secondary test referred to as rigid test.

A performance assessment test-bench was proposed to estimate the experimental bias and errors of the method. Classic optical method was also implemented so as to compare each method strengths and weaknesses.

As a conclusion, the volume-based method proved to have similar or lower measurement error than the classic optical method provided that the syringe diameter used in the syringe pump is properly chosen and that no leakage occurs during the tests. Eventually, it was experimentally proven that the aspiration aperture diameter has a negligible impact on the measurements error. User recommendations were also provided to guide any user that would be prone to use such a method.

The results of this chapter provide encouraging perspectives to use the new volume-based aspiration device for *in-vivo* characterization of soft human tissues. For this purpose, the whole inverse characterization procedure should first be validated on synthetic materials to assess the accuracy of the characterization method and avoid any risk during *in-vivo* measurements on real human tissues. In Chapter 3, the method is validated on soft silicone materials and the inverse identified material parameters are compared with reference characterization results (tensile and bulge tests).

CHAPTER

THREE

VOLUME-BASED ASPIRATION METHOD VALIDATED ON SILICONES

Some parts of this chapter have been submitted and can be found in the following reference

- ***SA. Elahi, N. Connesson, G. Chagnon, Y. Payan****, In-vivo soft tissues mechanical characterization: volume-based aspiration method validated on silicones, Exp. Mech., under revision.*

Contents

3.1 Introduction

The volume measurements using the volume-based aspiration method were evaluated in Chapter2. The effects of different parameters on the measurement accuracy were

also investigated. This volume-based method measures, for each negative pressure put into the chamber, the volume of the soft tissue aspirated through the device's aperture (Chapter 2): the pressure is thus known as a function of the volume. The material properties of the tissue can be identified with these experimental data using an inverse updated Finite Element (FE) method [Luboz, Promayon, and Payan, 2014].

The aim of this chapter is to validate the volume-based aspiration method on synthetic materials. For this purpose, first, the discrimination ability of the method is underlined on two silicone samples, one being softer than the other one. The the Young's modulus value of each material is then estimated using an inverse updated FE method and compared with reference materials properties obtained from classical characterization tests (tensile and bulge tests).

Section 3.2 focuses on the used experimental methods for aspiration and classical characterization tests. The preparation of silicone samples is detailed in this section. In section 3.3, the assumed constitutive material model is presented. Then, the FE modeling of the aspiration test is described while the methods for materials parameters identification using both the classical characterization tests and the inverse identification based on aspiration tests are explained. The results of the aspiration tests and the inverse and classical identifications are presented in section 3.4. The qualitative experimental data and the identified materials parameters using the inverse and reference characterization methods are compared in section 3.5. In this section, some user recommendations are given in order to help the users to get accurate results.

3.2 Experiments

3.2.1 Silicone samples

According to the literature, several synthetic materials have mechanical properties within the same range of human soft tissues [Franceschini et al., 2006; Luboz et al., 2012; Vuskovic, 2001]. RTV-EC00 silicone, obtained by mixing two components (base and catalyst), was chosen due to its ability to generate samples with a very low stiffness (equivalent Young's moduli of the order of some kPa). After removing any air bubble from the mixture using a vacuum chamber, samples were hardened for two weeks at room temperature. For RTV-EC00 silicone, changing the ratio of base and catalyst impacts the silicone stiffness. Two soft silicones were thus generated, using the ratios:

- Silicone#1: 40% base, 60% catalyst.
- Silicone#2: 45% base, 55% catalyst.

For each silicone, three types of samples were created using two different molds:

- Aspiration test: cylindrical bulk sample (110 mm diameter, 50 mm height)
- Tensile and bulge test: 2 mm thick membrane cut either into a 50 mm disks or 4 $mm \times 100$ mm strips.

For each silicone, all samples were made in the same day from the same mixture to ensure identical mechanical properties.

3.2.2 Aspiration tests

The aspiration system and volume-based method will be briefly presented in this section. Details can be found in [Elahi, Connesson, and Payan, 2018]. An aspiration head was applied on a soft material (Fig. 3.1) while a negative pressure aspirates part of this material through a circular aperture of 9.7 mm diameter. A programmable syringe pump coupled with a syringe (Sy1 in Fig. 3.1a) was used to reduce the pressure inside the system. During the test, the pressure variation P was measured using a digital manometer with a precision of ± 0.004 $mbar$. The corresponding aspirated volume V^{total} was measured by the syringe pump given the piston translation with a resolution of ± 0.002 ml.

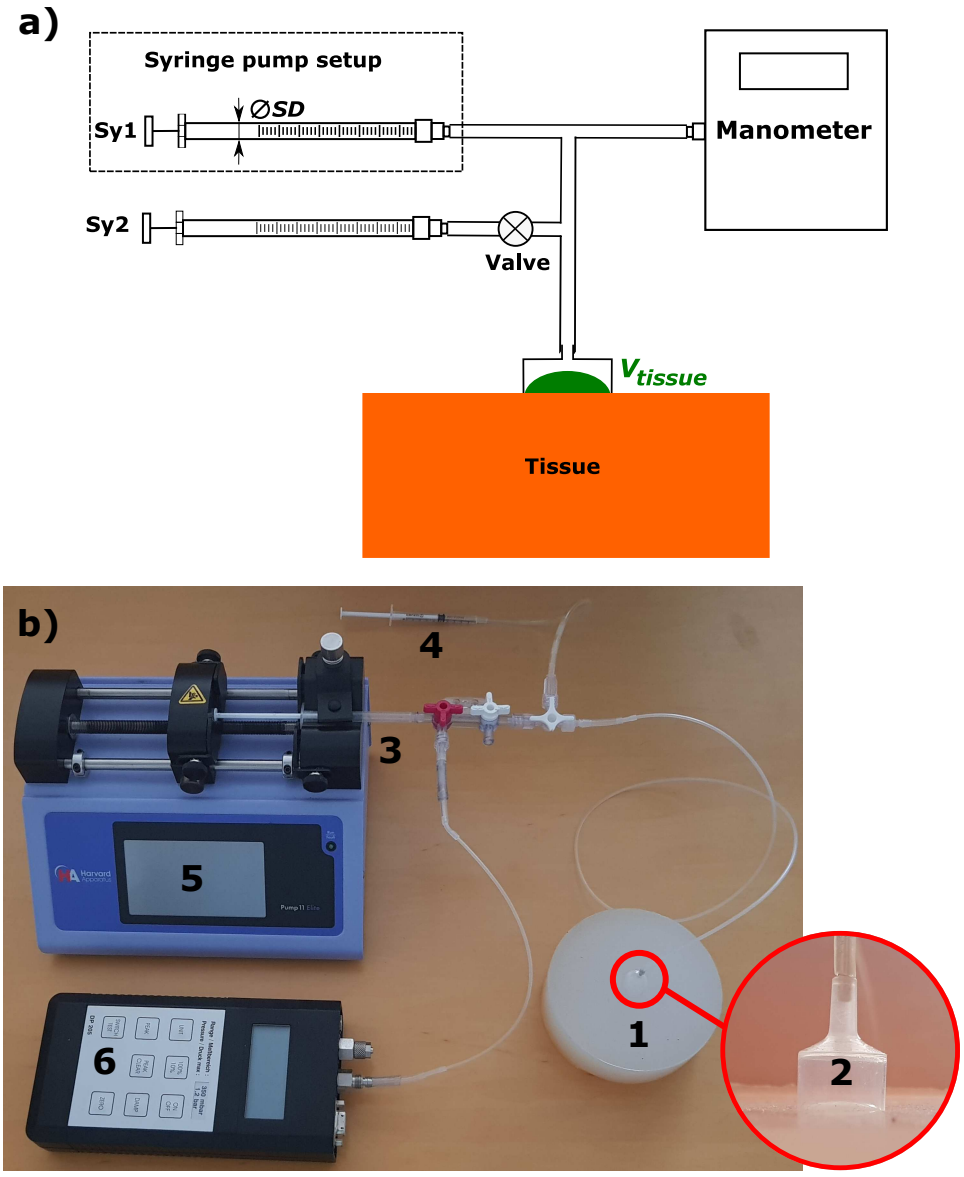

Figure 3.1: Volume-based aspiration setup: a) schematic of the setup and b) photograph of the setup: (1) silicone sample, (2) aspiration probe, (3) Sy1, (4) Sy2, (5) syringe pump and (6) manometer.

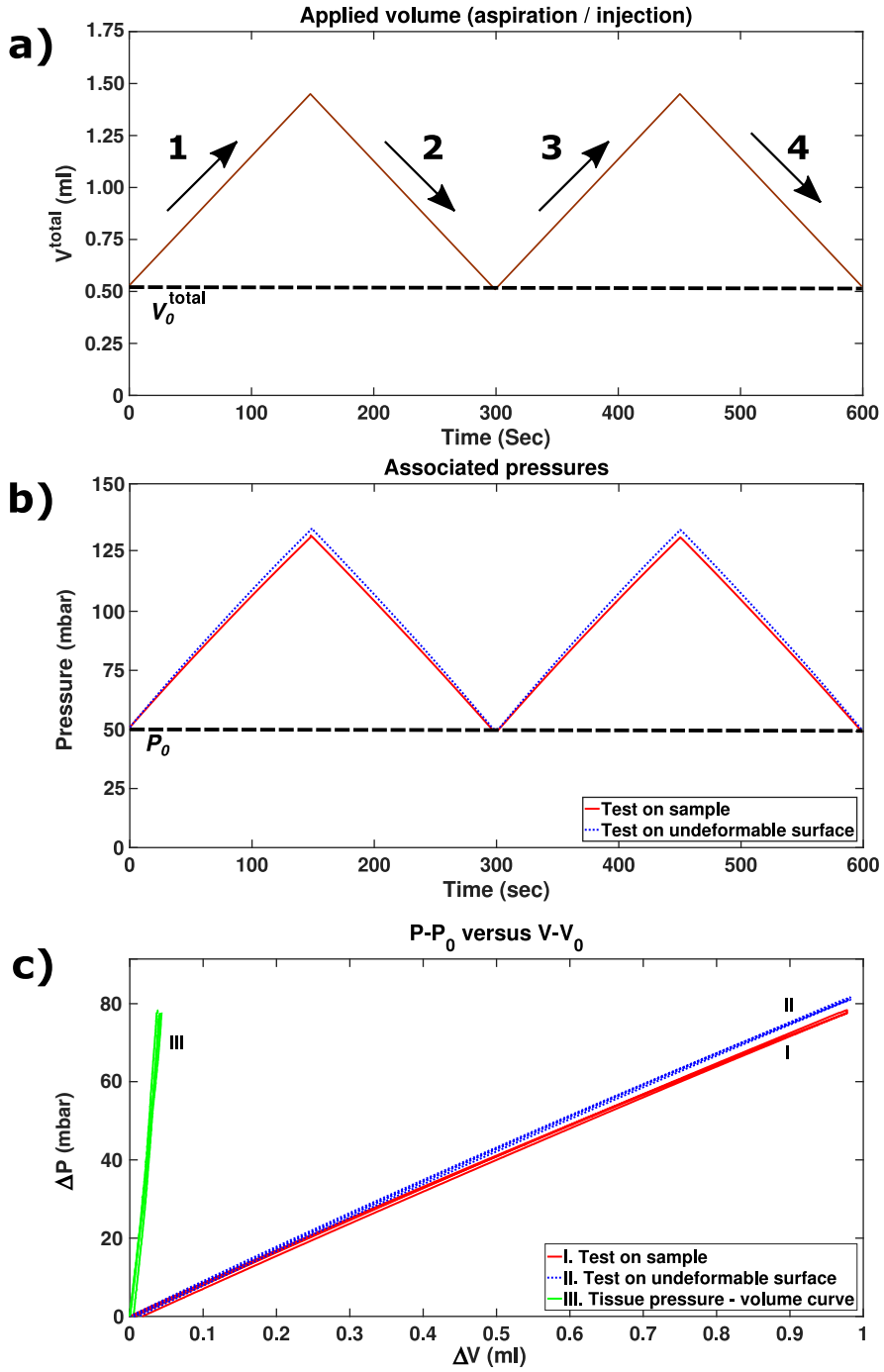

Figure 3.2: Methodology (example on Silicone#1): a) applied volume loading path, b) associated negative pressures of the test on sample (red) and on the undeformable surface (blue) and c) resulting pressure-volume curves (red and blue) and extracted tissue behavior (green).

The measured volume $V^{total}(P)$ contains information on both the aspirated tissue volume inside the chamber $V_{tissue}(P)$ and the volume changes in the device $V_{system}(P)$ (air expansion, elasticity of the connections, tubes, syringe, etc.). The changes in the system volume V_{system} were experimentally assessed during a second step by testing an undeformable material (stiff material in comparison to the system): in this experimental

configuration the aspirated tissue volume V_{tissue} remains zero and the system volume V_{system} compressibility can be directly measured. Such an experiment provided the required data to evaluate a calibration curve $V_{system}(P)$. The aspirated tissue volume V_{tissue}^{exp} can thus naturally be estimated by:

$$V_{tissue}^{exp}(P) = V^{total}(P) - V_{system}(P) \tag{3.1}$$

As experimentally demonstrated in [Elahi, Connesson, and Payan, 2018], decreasing the Syringe Diameter of Sy1 (SD in Fig. 3.1a) improves the measurement precision and repeatability: Sy1 is here a 1 ml syringe with a diameter of 4.7 mm. However, using a small syringe also limits the aspirated volume range and thus the maximal aspirated tissue volume V_{tissue}. In order to solve this problem, an additional 1 ml syringe with a diameter of 4.7 mm (Sy2 in Fig. 3.1a) and a valve were added to the system. Before starting the syringe pump, an initial volume was withdrawn from the system using Sy2, while applying a vertical load to the aspiration probe to limit possible leakage. The vertical load was then removed and the withdrawn volume was manually adjusted to reach P_0. The valve was then closed and the associated initial volume V_0^{total} was read directly on the syringe Sy2. It should be mentioned that this volume V_0^{total} shall be overestimated due to initial leakage. If no leakage occurs and given the nominal volume of Sy2 (1 ml), V_0^{total} is estimated to be measured at $\pm 0.01ml$.

Using Eq. 3.1, the starting point $(V_{0(tissue)}^{exp}, P_0)$ was computed and considered as the initial situation. Impact of potential errors on the experimental measurement of $V_{0(tissue)}^{exp}$ will be discussed in section 3.5.1.

The volume loading path, defined with four steps (air aspiration / injection, see Fig. 3.2a), was then applied using Sy1 in both tests, either with the silicone or the undeformable surface. As all the pressures dealt with are negative compared to atmospheric pressure, only the absolute values will be discussed. An example of pressure results are plotted versus time in Fig. 3.2b. The pressure-volume curves of the tests were extracted from the data (Fig. 3.2c, red and blue curves) and the tissue pressure-volume curve was computed using Eq. 3.1 (Fig. 3.2c, green curves).

In this study, the initial pressure P_0 was set to be 50 $mbar$ (the maximum applied pressure during this work is of 168 $mbar$). Total volume changes, controlled using the syringe pump, were applied with the rate of 0.4 ml/min, which was experimentally checked to be small enough to provide quasi-static mechanical behavior for the tested material. This was ensured by repeating the various tests at different deformation rates and choosing a slow enough rate.

In order to check the reproducibility of the results, the aspiration tests on each silicone were repeated nine times in the same condition. For each set of the nine tests, the STandard Deviation (STD) of the volume measurements V_{tissue} were calculated and used as a parameter to assess the measurement precision and reproducibility.

3.2.3 Classical characterization tests

Two classical characterization tests, namely uniaxial tensile test (Fig. 3.3a) and equibiaxial tensile test generated at the top of a bulge test (Fig. 3.3b), were used to identify the reference stress-strain behaviors of the silicones and their associated mechanical parameters. These results will then be compared with the volume-based aspiration method measurements.

3.2.3.1 Uniaxial tensile test

For the uniaxial tensile measurements, a MTS machine with a load cell of 25 N was used (MTS Criterion, Model 41). For each silicone material, 20 rectangular specimens were made. Five groups, each contained 4 specimens, were tested at different engineering extensional strain levels ($\epsilon_{xx(max)} = 20\%$, 30%, 50%, 80% and 100%) (Fig. 3.3a) In order to see any possible hysteresis and load history impact on the material behavior, each sample was tested during 5 loading-unloading cycles.

3.2.3.2 Bulge test

A bulge test was also conducted. A circular sample of 2 mm thickness was clamped between two flanges (Fig. 3.3). A syringe connected to the bottom of the circumferential clamp was used to inject a liquid under the disk to perform the bulge test. The membrane was thus inflated using the syringe pump while measuring the internal pressure with a manometer.

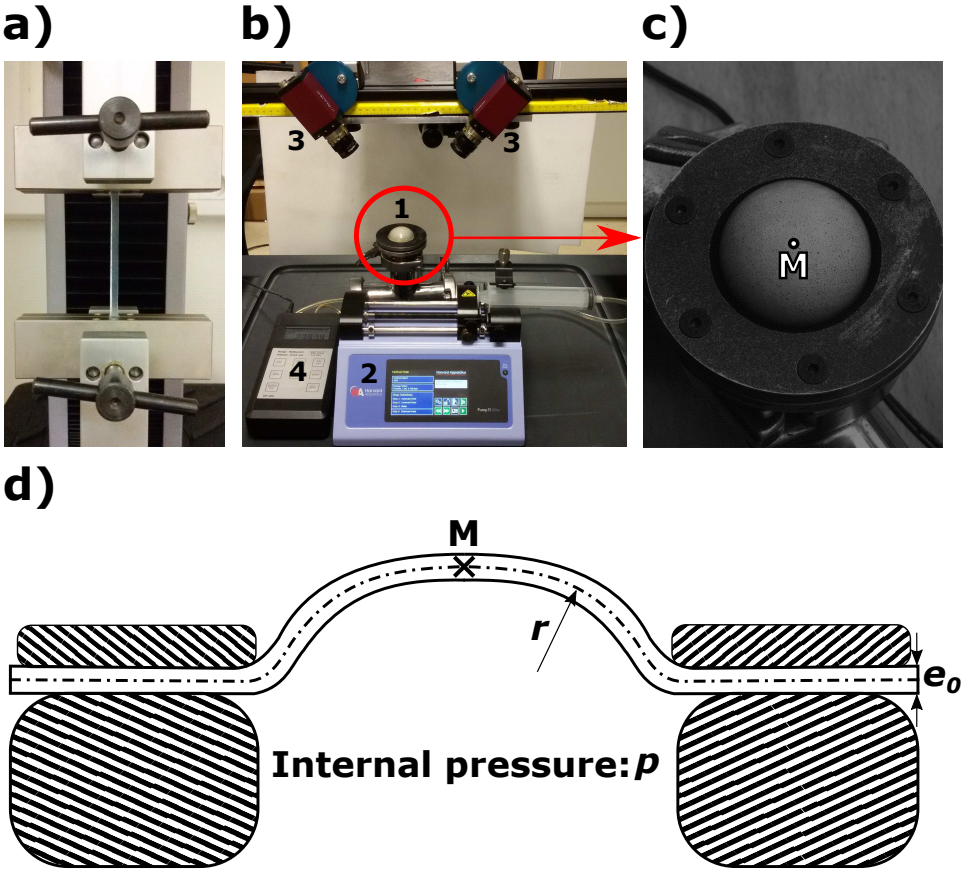

Figure 3.3: a) Tensile test setup, b) Bulge test setup: (1) Bulge membrane and circular clamp, (2) syringe and syringe pump, (3) cameras, (4) manometer, c) close-up of the inflated silicone sample and localization of equibiaxial loading (point M) and d) schematic of the bulge test setup.

The 3D membrane displacement were tracked using Stereo Digital Image Correlation (SDIC, Figs. 3.3b and 3.3c). The upper surface of the silicone sample was coated with a

stochastic paint pattern made of small black speckles to comply with the SDIC requirement and to extract strain field maps over the membrane. Due to transparency of the used materials, the system was filled with a white color liquid such as milk to provide a proper contrast.

The axial-symmetry of the experimental configuration induces the equibiaxiality of the stress and strain state at the top of the inflated membrane (point M, Fig. 3.3c) [Machado et al., 2017]. Given the thickness dimension is $1/25th$ of the membrane diameter, the in-plane stresses were assumed to be uniform along the thickness dimension. The curvature of the inflated sample was also assumed to be the same along all directions at the disk center due to the system axial-symmetry and the materials isotropy and homogeneity. A region of 3 mm^2 at the sample pole, around point M, was considered for the analysis. In-plane components of First Piola-Kirchhoff stress $\sigma_{xx(Bulge)} = \sigma_{yy(Bulge)}$ at point M can thus be calculated using the equation [Machado et al., 2017]:

$$\sigma_{xx(Bulge)} = \sigma_{yy(Bulge)} = \frac{pr}{2e_0}\lambda_{(Bulge)}; \quad \sigma_{zz(Bulge)} = 0 \tag{3.2}$$

where e_0 is the initial thickness of the specimen, r the local curvature radius, $\lambda_{(Bulge)} = \lambda_{xx} = \lambda_{yy}$ the principal stretch and p the pressure recorded during the test (Fig. 3.3d). The details about calculation of the stress from the SDIC measurement can be found in [Hill, 1950].

The bulge test was performed on 4 different specimens for each silicone. In order to study any possible hysteresis and load history impact on the behavior of the materials, each sample was tested during 5 inflating-deflating cycles up to a max strain of 70%. The average responses of the 4 different specimens were then calculated.

3.3 Modeling and inverse characterization

In order to perform the inverse characterization of the materials using aspiration tests, a material model was selected. This model was also used to identify the materials mechanical parameters using the classical characterization tests. In the following sections, the used material model, FE modeling of the aspiration tests and the materials parameters identification methods using both classical and aspiration tests will be presented.

3.3.1 Gent material model

The hyperelastic model proposed by Gent, 1996 was used to model the silicone rubbers [Chagnon, Marckmann, and Verron, 2004]. The strain energy function of the Gent model (W_G) is given by:

$$W_G = -\frac{EJ_m}{6}\ln\left(1 - \frac{I_1 - 3}{J_m}\right) \tag{3.3}$$

where E and J_m are the two material parameters and I_1 is the first Cauchy Green strain invariant. J_m represents the maximum value of (I_1-3) that can be undergone by the material. The Gent model was used to identify the materials parameters either using FE inverse method and the aspiration tests results or using the classical characterization results.

3.3.2 FE modeling of the aspiration tests

A FE simulation of the aspiration tests was performed (ANSYS software) in order to identify the materials parameters. The tests were modeled in 2D with axisymmetry (Fig. 3.4). As the silicone cylinder diameter and height were respectively about 11 and 5 times larger than the aperture diameter (section 3.2.1), boundary conditions on the bottom and the outer sides of the tissue structure do not have any effect on the simulations results. The bottom layer of the nodes was fixed for horizontal and vertical displacements and the outer side of the silicone was allowed to move freely. The sample was meshed with 5800 Quadrilateral 8-node (Q8) elements. The experimental contact properties between the aspiration aperture and the material are unknown. To study the sensitivity of simulation results on these properties, the contact was modeled with two assumptions: (1) a frictionless contact (friction coefficient based on the Coulomb's Law μ=0) and (2) a contact with friction coefficient of μ=1. The displacement of the tissue surface inside the aperture was used to compute the aspirated volume at each pressure step.

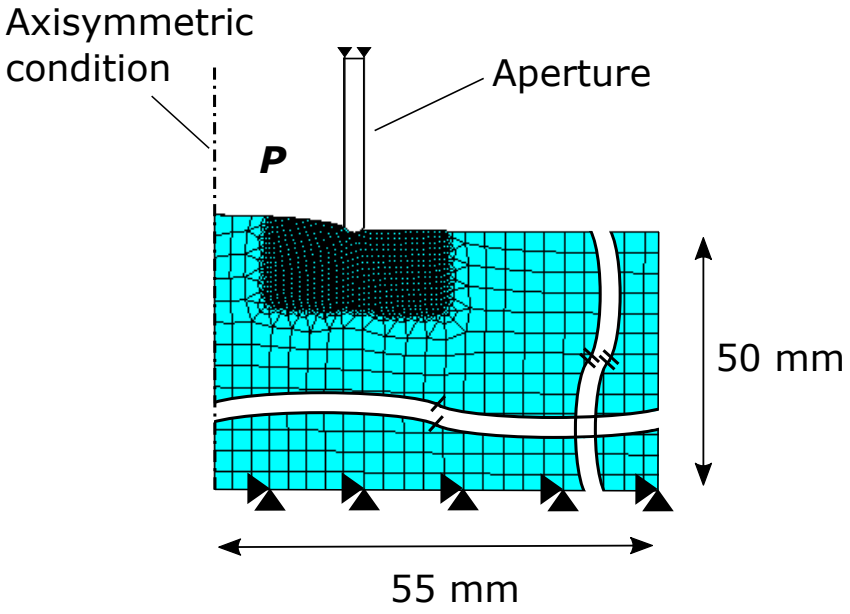

Figure 3.4: Schematic of the FE model and boundary conditions of the aspiration experiment in the deformed configuration.

3.3.3 Material parameters identification

3.3.3.1 Reference material parameters identification on classical tests results

To identify the Gent model parameters using classical tests, the Fist Piola-Kirchhoff stress-stretch relations were calculated based on Eq. 3.3 for uniaxial and equibiaxial extensions, respectively as:

$$\sigma_{xx(uni)} = \left(\lambda_{(uni)}^2 - \frac{1}{\lambda_{(uni)}}\right)\left[\frac{EJ_m/3}{(J_m+3)\lambda_{(uni)} - \lambda_{(uni)}^3 - 2}\right] \tag{3.4}$$

and

$$\sigma_{xx(equi)} = \sigma_{yy(equi)} = \left(\lambda_{(equi)}^{5} - \frac{1}{\lambda_{(equi)}}\right)\left[\frac{EJ_m/3}{(J_m+3)\lambda_{(equi)}^{4} - 2\lambda_{(equi)}^{6} - 1}\right] \tag{3.5}$$

where $\sigma_{xx(uni)}$ and $\sigma_{xx(equi)}$ are stresses and $\lambda_{(uni)}$ and $\lambda_{(equi)}$ are stretches in uniaxial and equibiaxial extensions, respectively. Details about the calculation of the stresses using the strain energy function can be found in [Marckmann and Verron, 2006].

The reference model parameters for each material were estimated by minimizing the least square function S, combining both uniaxial tensile and bulge results:

$$S = \frac{\sum_{j=1}^{J}((\sigma_{xx(uni)j} - \sigma_{xx(Tensile)j})^2)}{J} + \frac{\sum_{k=1}^{K}((\sigma_{xx(equi)k} - \sigma_{xx(Bulge)k})^2)}{K} \tag{3.6}$$

where:

- $\sigma_{xx(uni)}$ and $\sigma_{xx(equi)}$ are described by Eqs. 3.4 and 3.5,
- $\sigma_{xx(Tensile)}$ and $\sigma_{xx(Bulge)}$ are stresses from the tensile and the bulge tests, respectively,
- j and k are the deformation steps indices in the tensile and the bulge tests, respectively,
- J and K are the total numbers of deformation steps in the tensile and the bulge tests, respectively.

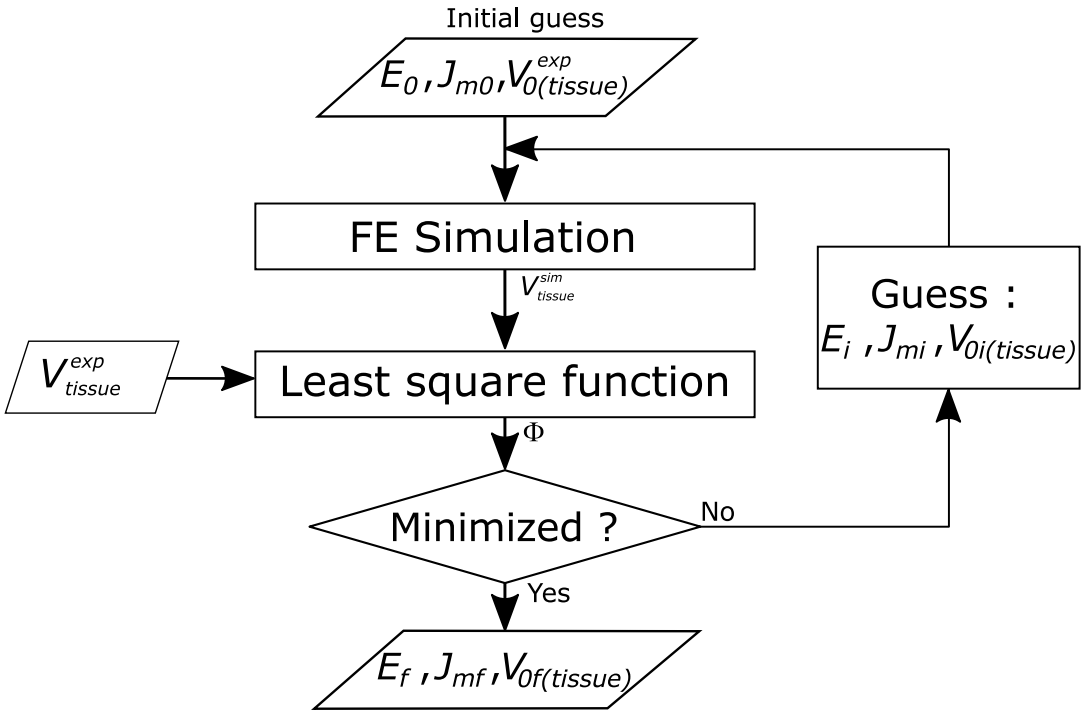

Figure 3.5: Schematic representation of the optimization process for the inverse characterization of the model parameters.

3.3.3.2 Inverse material parameters identification on aspiration tests results

To identify the model parameters (Eq. 3.3) using aspiration tests, an optimization process was adapted from Weickenmeier, Jabareen, and Mazza, 2015. The optimization scheme was extended to minimize the least square function ϕ representing the fitting quality of the pressure-volume curves obtained from the FE simulation (V^{sim}_{tissue}) and the experimental aspiration test (V^{exp}_{tissue}):

$$\phi = \sum_{i=1}^{I} \left[V^{sim}_{tissue}(P_i) - \left(V_{0(tissue)} + V^{exp}_{tissue}(P_i) \right) \right]^2 \tag{3.7}$$

where P_i presents the measured pressure in the ith step, I is the number of points retrieved during the test and $V^{exp}_{tissue}(P_i)$ are the experimental data. The unknowns to identify are the material parameters E and J_m and the initial aspirated volume $V_{0(tissue)}$ that could be affected by leakage.

A schematic of the optimization process is presented in Fig. 3.5, where E_0, J_{m0} and $V^{exp}_{0(tissue)}$ are initial guessed values, E_i, J_{mi} and $V_{0i(tissue)}$ are the iteratively adapted parameters, and E_f, J_{mf} and $V_{0f(tissue)}$ are the final results of the optimization process. The material parameters and the initial aspirated volume in each iteration were guessed using a Nelder-Mead simplex algorithm [Nelder and Mead, 1965] (*fminsearch* procedure in MATLAB).

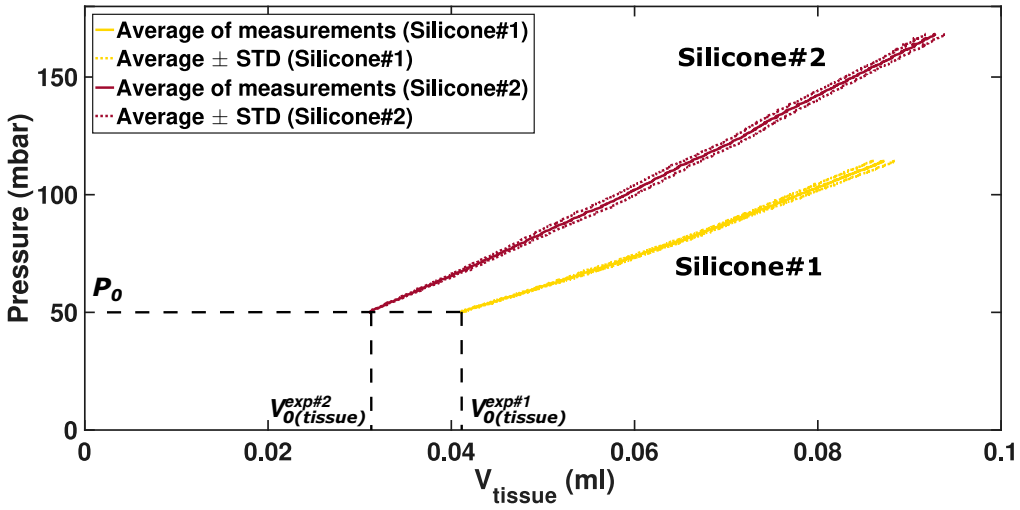

Figure 3.6: Averages and associated STD of pressure-volume curves (loading steps 1 and 3 in Fig. 3.2a) of nine aspiration measurements for Silicones#1 and #2.

3.4 Results

3.4.1 Aspiration results

Results of the volume-based aspiration measurements (loading steps 1 and 3 in Fig. 3.2a) on Silicones#1 and #2 are presented in Fig. 3.6: for each material, average and STD of

pressure-volume (P versus V_{tissue}^{exp}) curves of the nine aspiration tests are plotted. The STD of volume measurements according to the average values for Silicones#1 and #2 are 2.63% and 2.53%, respectively. This highlights the high reproducibility of the aspiration measurements on both materials and also the measurements precision. Moreover, results presented in Fig. 3.6 validate the ability of the volume-based aspiration method to clearly discriminate the two slightly different materials properly: given the measurement precision, aspiration behaviors contrast of more than 2×STD=5% can be identified.

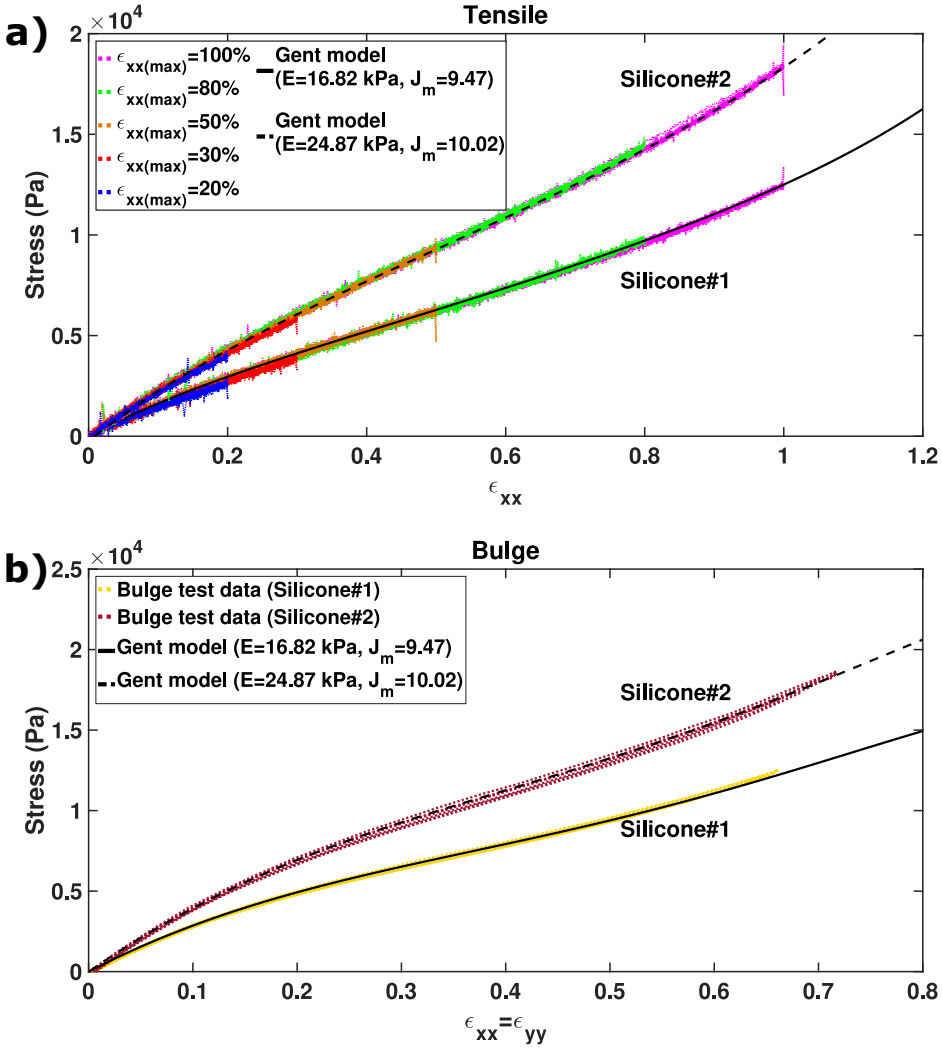

Figure 3.7: Stress-strain results and fitted Gent model using Eq. 3.6 for Silicones#1 and #2 (five cycles of loading-unloading for each): a) tensile tests with increasing strain levels and b) bulge tests.

3.4.2 Classical characterization results

The averaged stress-strain curves over 4 specimens of the uniaxial tensile tests on Silicones#1 and #2 with increasing strain levels ($\epsilon_{xx(max)}$ = 20%, 30%, 50%, 80% and 100%) are presented in Fig. 3.7a. For each strain level, the curve of the five-cycle (load-unload) tensile tests is plotted. These results indicate that both materials present no hysteresis

nor stress softening. Moreover, the superposition of the stress-strain curves with different strain levels and different specimens confirms the test reproducibility and accuracy for both silicones.

The averaged stress-strain results over 4 specimens of the five-cycle (load-unload) equibiaxial bulge tests on Silicones#1 and #2 are plotted in Fig. 3.7b. As previously, no hysteresis behavior and no stress softening can be observed in these results and behavior differences between samples during the five cycles on each material are indiscernible as was expected for unfilled silicone rubbers [Rey et al., 2013].

Gent model curves for uniaxial and equibiaxial extensions (Eqs. 3.4 and 3.5) were respectively fitted to the tensile and bulge tests data of each silicone material (Figs. 3.7a and 3.7b). Both fittings for each silicone were performed simultaneously by minimizing the cost function S (Eq. 3.6) to estimate the best reference parameters (E and J_m) as provided in Table 3.1. Since the experimental results of the tensile tests with different levels of strains overlapped (Fig. 3.7a), the Gent model was only fitted to the results of the tests with $\epsilon_{xx(max)} = 100\%$ strain level.

Table 3.1: Gent model parameters of the silicone materials obtained from classical and inverse characterizations with friction coefficients of μ=0 and 1. Relative errors were calculated in comparison with the reference parameters.

Material	Material constants	Classical characterization	Inverse characterization for μ=[0, 1]	Comparison error (%) for μ=[0, 1]
Silicone#1	E	16.82 kPa	[18.30, 17.76] kPa	[8.8, 5.6]
	J_m	9.47	[9.89, 9.65]	[4.4, 1.9]
Silicone#2	E	24.87 kPa	[26.51, 25.89] kPa	[6.6, 4.1]
	J_m	10.02	[10.16, 10.11]	[1.4, 0.9]

Table 3.2: Initial aspirated volume measured during the experiments and identified during the optimization procedure with friction coefficients of μ=0 and 1. Value of cost function ϕ (Eq. 3.7) for each case is also provided.

Material	Experimental initial volume V_0^{exp} (ml)	Identified initial volume $V_{0f(tissue)}$ (ml) $\mu = [0, 1]$	Mismatch (%) $\mu = [0, 1]$	ϕ value (ml^2) $\mu = [0, 1]$
Silicone#1	0.04	[0.0424, 0.0410]	[6.0, 2.5]	[4.8, 6.3]×10⁻3
Silicone#2	0.03	[0.0314, 0.0304]	[4.7, 1.3]	[3.2, 6.1]×10⁻3

3.4.3 Inverse characterization results

The identified material parameters E_f and J_{mf} obtained after the minimization of the cost function ϕ (section 3.3.3.2) for both contact conditions (frictionless and with friction coefficient μ=1) and their errors in comparison to classical characterization results are reported in Table 3.1. Table 3.2 compares the identified initial aspirated volumes $V_{0f(tissue)}$ and their corresponding values obtained from the experiments $V_{0(tissue)}^{exp}$. Values

of the cost function ϕ for different materials and contact conditions are also reported in Table 3.2.

Comparison of the material model parameters obtained from the inverse and the classical characterizations shows a slight overestimation (about 7%) of the inverse characterization for both silicones (Table 3.1).

3.5 Discussion

3.5.1 Inverse identification results

The direct comparison of the numerical curves and the experimental aspiration curves are presented in Fig. 3.8. The materials parameters obtained from both the classical measurements and inverse identifications were used for the FE simulations (Table 3.1). The plotted curves of FE simulations with the identified materials parameters in Fig. 3.8 validate the identifications and adequacy of the chosen constitutive model equation (Eq. 3.3).

A difference lower than 6% between experimental and identified initial volumes ($V^{exp}_{0(tissue)}$ and $V_{0f(tissue)}$ in Table 3.2) highlights the absence of the initial leakage at the beginning of the tests.

In the literature, the experimental data from aspiration measurements were used to estimate Young's moduli of silicones assuming a Neo-Hookean model [Luboz et al., 2012]. A difference of about 30% between inverse characterization (using the optical aspiration device LASTIC) and classical characterization of silicone materials with a similar range of elasticity was obtained. For the studied friction coefficients (μ=[0, 1]), errors of [8.8, 5.6]% and [6.6, 4.1]% in the values of the Young's moduli of Silicones #1 and #2 were estimated, respectively (Table 3.1).

The improvement of Young's modulus estimation in the volume-based aspiration device comparing to LASTIC is due to:

- continuous recording of the pressure data at a sampling frequency of 5 Hz with a precision of ± 0.004 *mbar* using a digital manometer comparing to pressure measurement precision of ± 6 *mbar* in [Luboz et al., 2012].
- replacement of the apex height measurement by the aspirated volume measurement and thus avoidance of optical alignment errors.
- application of a direct inverse FE procedure versus the use of a library of prearranged FE simulations results in [Luboz et al., 2012].
- use of a Gent model in this study versus the Neo-Hookean model used by Luboz et al., 2012. The Gent constitutive model seems to better model the silicone materials used in this study (Fig. 3.7). In fact, the Neo-Hookean model can provide a softening effect at large strains. On the contrary, using a Gent model allows to define a stiffening effect controlled by the parameter J_m. Such a stiffening effect is often observed in biological soft tissues.

As observed in the previous study [Luboz et al., 2012], the Young's moduli were overestimated. Part of this error was induced by the chosen friction coefficient in the FE model (Table 3.1). This error was not totally induced by this parameter as the identified

moduli remain overestimated even for a friction of μ=1 (assuming the actual friction coefficient belongs to the range μ=[0,1]).

The remaining error may be attributed to the experimentally unknown vertical load applied to the aspiration head through the head clamp during the test. A sensitivity analysis would be required to assess the effect of each parameter. This will be performed in further work.

The value of $V^{exp}_{0(tissue)}$ is considered unknown during the inverse identification process. This choice adds a degree of freedom during the identification and may affect the identified model parameters. In fact, the data about the tissue behavior before point ($V^{exp}_{0(tissue)}$, P_0) could be really valuable while performing inverse identification on biological soft tissues: the material may rapidly "stiffen" at low strain and at pressures lower than P_0. Unfortunately, soft materials behaviors at small loadings are extremely difficult to be experimentally measured, especially *in-situ* and *in-vivo*; the reference state of a soft material is badly defined due to the presence of internal residual stress or initially applied loads. Localizing the zero both in strain and stress for such a soft material is an arduous and interesting problem that was out of the scope of this paper.

In this study, the difference between the experimental and identified initial volumes ($V^{exp}_{0(tissue)}$ and $V_{0f(tissue)}$) is lower than 6%. This difference is small and accounts both for the absence of leakage during measurement, and for the model ability to predict the unknown material behavior for pressure smaller than P_0.

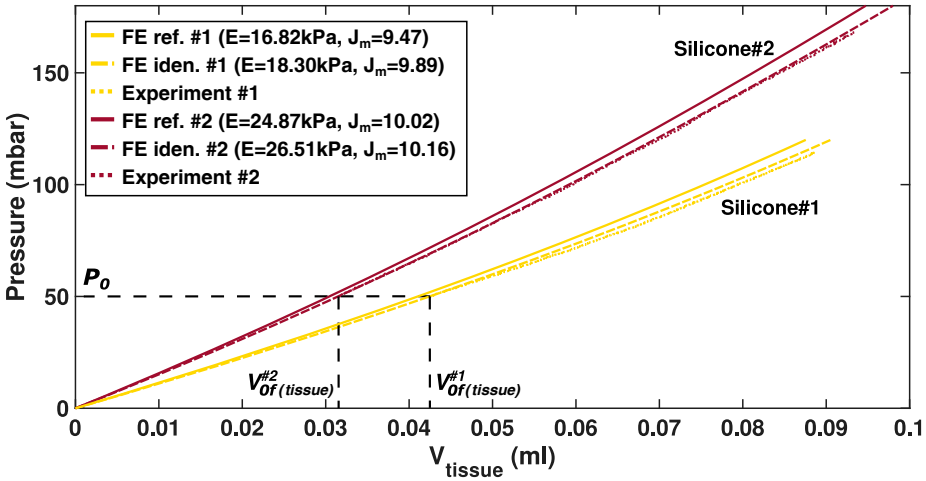

Figure 3.8: Averages of the aspiration measurements and the corresponding FE simulation curves (with frictionless contact μ=0 using the reference parameters obtained from classical measurements and the identified parameters from the inverse procedure (Table 3.1 and 3.2)) for Silicones #1 and #2.

3.5.2 Qualitative comparison of experimental data

Assuming a constitutive model to properly simulate the studied material behavior (hyperelastic, poroelastic or viscoelastic models in the case of time-dependent behavior) is an arduous and complex task when performing an inverse identification on the biological tissues. Moreover, if the difference between experimental and identified initial volumes

($V^{exp}_{0(tissue)}$ and $V_{0f(tissue)}$) is considered significant, the experimental uncertainties on the measured volume $V^{exp}_{0(tissue)}$ may affect the interpretation of the identified parameters of the model.

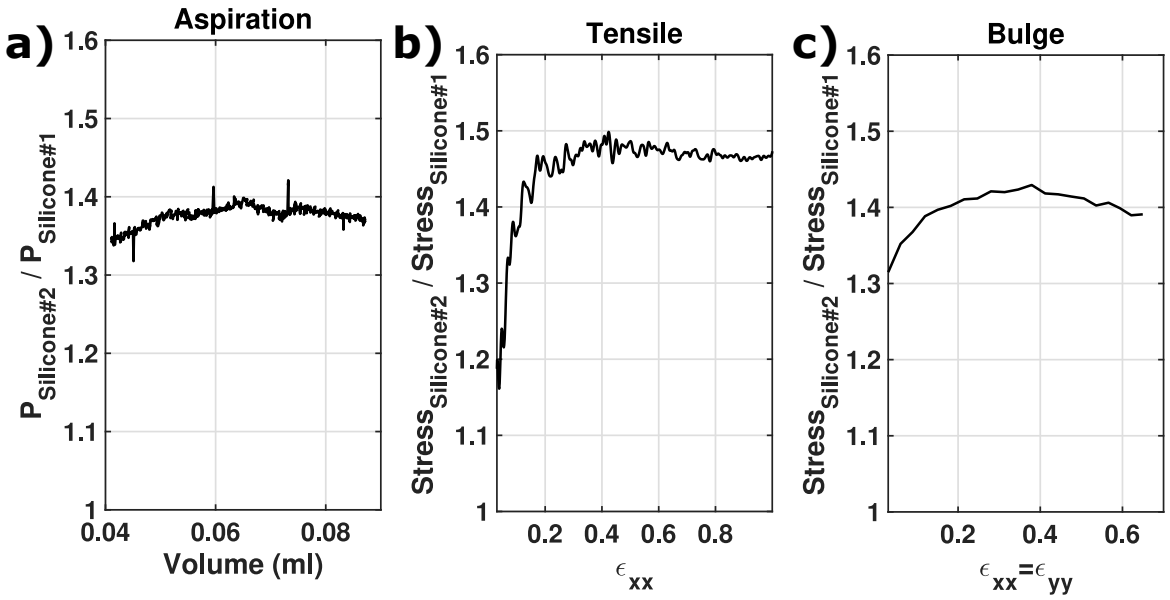

Figure 3.9: Ratios of averaged experimental data for: a) aspiration tests, b) tensile tests and c) bulge tests.

It is thus believed by the authors that analyzing the experimental data without assuming a specific behavior model partially circumvents this issue. This is the reason why a simple ratio of the two silicones' results is provided in this section. This analysis highlights the behavior difference between the two silicones. In addition, performing such an analysis highlights the method ability to provide contrast between different mechanical local behaviors without performing an inverse identification: this feature will enable the creation of contrast maps on the surface of mechanical heterogeneous materials frequently met during *in vivo* and *in situ* measurements. For example, as was very preliminary investigated by Schiavone et al., 2009, such aspirations on different locations of the brain surface could identify the position of a stiffer region that would correspond to a surface tumor.

The loading ratios for the two silicones were calculated for each characterization method:

1. by dividing pressures of Silicones#2 to #1 at the same volume for aspiration tests (Von Mises strain account for the local 3D strain state at the pole of the aspirated volume was [0.19, 0.41]),

2. by dividing stresses of Silicones#2 to #1 at the same strain for the tensile and bulge tests, respectively.

The loading ratios are compared in Fig. 3.9. The ratios for all the aspiration, tensile and bulge tests are of the same amplitude. The observed contrasts between mechanical behaviors of the two silicones are thus similar, even if local stress states are very different

from one test to another (triaxial (aspiration), biaxial (bulge), uniaxial (tensile)). These results indicate a similar ability of the tested mechanical characterization methods to highlight the contrast between different mechanical behaviors. These data can thus be used to highlight mechanical behavior contrasts between materials without requiring a time-consuming inverse identification step.

More investigations on heterogeneous and anisotropic materials will be performed in the future works.

3.5.3 User recommendations

To use the volume-based aspiration method, a user should take the following considerations into account:

- to reduce experimentally induced bias, the absence of leakage between the tissue and the measurement probe should be checked before performing the tests. To ensure this, the initial negative pressure P_0 stability versus time should be checked. Ultrasound gel could be used between the suction probe and the studied material to improve the leakage prevention.

- in the aspiration tests, the friction between the aspiration probe and the studied material is unknown. Adding Ultrasound gel between the suction probe and the studied material would reduce the contact friction during the experiments, so as to diminish the range choice for μ in the simulations.

- according to previous results [Elahi, Connesson, and Payan, 2018], use of a syringe with a smaller diameter for the measurements increases reproducibility of the results and decreases the measurements errors. In this work, using of a small syringe with a diameter of 4.7 mm was enabled by the presented setup in Fig. 3.1.

- the use of various loading steps provides a tool to check the measurements reproducibility (Fig. 3.2).

- the use of a special suction probe holder would be advisable in order to avoid applying external load on the suction probe.

3.6 Conclusion

This chapter evaluated a volume-based aspiration method for *in-vivo* characterization of soft tissues on silicone materials. The ability of the method to discriminate two slightly different silicones was assessed. The aspiration test was repeated nine times on each material. The percentages of STD according to average volume measurements of 2.63% and 2.53% were obtained for the two materials. The method will thus be able to discriminate aspiration behavior differences of 2×STD=5%. Additionally, the measured pressure ratio of the aspiration tests for the two materials is similar to the stress ratios obtained with classical characterization tests. A relative discrimination is thus easy and relative mechanical behavior mapping of soft tissues (organ or skin) is possible without requiring an inverse procedure.

The mechanical parameters of the Gent model were identified either on the classical or the aspiration tests using a direct and FE updating method, respectively. Young's moduli similar to the classical tests with about 7% maximum overestimation for the two silicones were identified. The errors are about 4 times lower than the previous studies based on optical aspiration measurements. These results indicate improvement of the materials identification accuracy using the new device comparing to the previous aspiration devices.

According to the presented results, the volume-based method can thus be used for (1) *in-vivo* and *in-situ* mapping without inverse procedure, and (2) identification of the mechanical properties of various soft tissues.

Soft human tissues, such as skin, usually have complex multi-layered structures. It thus seems to be important to study the mechanical properties of such tissues in depth. In the volume-based aspiration method, the aspiration probe can be changed easily to use different aperture diameters. This feature is used in Chapter 4 to introduce a method in order to identify the superficial layers thicknesses and mechanical properties of each distinct layer.

CHAPTER

FOUR

THICKNESSES AND MECHANICAL PROPERTIES IDENTIFICATION OF MULTI-LAYER SOFT TISSUES USING ONLY A VOLUME-BASED SUCTION METHOD

Some parts of this chapter have been submitted and can be found in the following reference

- ***SA. Elahi, N. Connesson, Y. Payan****, Thicknesses and mechanical properties identification of multi-layer soft tissues using only a volume-based suction method, Exp. Mech., submitted.*

Contents

4.1 Introduction

Human soft tissues and organs such as skin, liver, arteries and vessels are often complex multi-layered structures. In these tissues, the individual layers have distinct mechanical properties that influence the overall mechanical behavior [Flynn, Taberner, and Nielsen, 2011b; Herlin et al., 2014; Jor et al., 2013; Xu and Yang, 2015; Zhao, Sider, and Simmons, 2011]. To identify these mechanical properties a technique based on tissue suction can be used, either considering homogeneous properties [Luboz, Promayon, and Payan, 2014; Mazza et al., 2005; Pensalfini et al., 2018] or in-depth gradient [Hendriks et al., 2006a; Weickenmeier, Jabareen, and Mazza, 2015].

Comparing suction measurements using different aperture sizes provides information on the mechanical properties contrasts and in-depth gradient [Aoki et al., 1997; Hendriks et al., 2006a; Zhao, Sider, and Simmons, 2011]: increasing the suction aperture diameter (AD) increases the depth of the affected tissue (Fig. 4.1). The experimental results thus contain more data about deeper tissue mechanical behavior. This idea has already been used to characterize different layers of human facial tissues, considering the skin and its underlying tissues as multi-layered materials and characterizing either two or three superficial layers [Barbarino, Jabareen, and Mazza, 2011; Weickenmeier, Jabareen, and Mazza, 2015], respectively. The optical systems made it difficult to change of the aperture diameter due to presence of the camera and mirror/prism in the suction probe. This lead the researchers to use only two different systems with aperture diameters of 2 mm and 8 mm, respectively. The two systems used were also different in their design, aspiration loading path and measurement method of the aspirated tissue height (using a camera versus a light source). Moreover, in these studies, the tissue layers thicknesses were supposed to be known and were obtained from Magnetic Resonance Imaging (MRI) and ultrasound measurements. An FE based inverse procedure was implemented to identify the materials parameters in the different tissue layers.

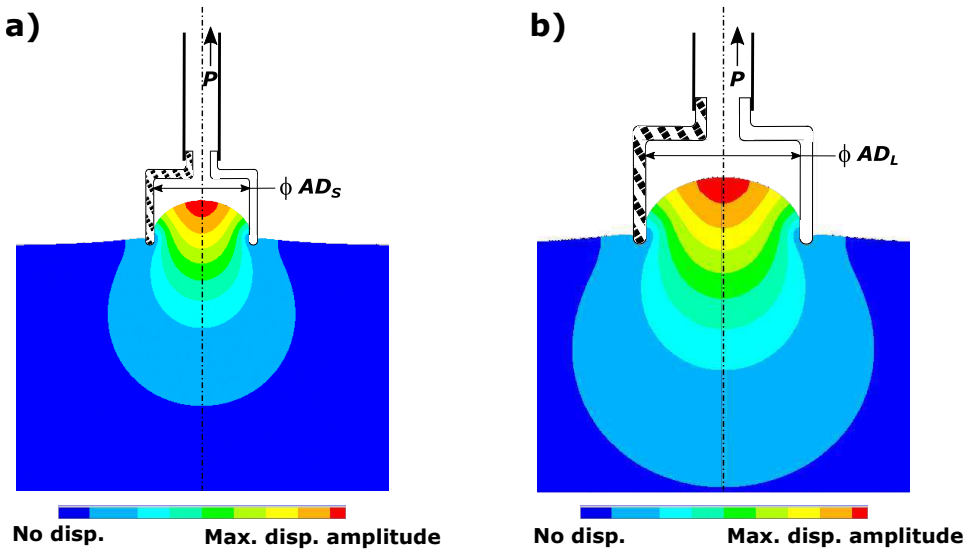

Figure 4.1: Schematic representation of the aperture diameter effect on the in-depth displacement amplitude of material during suction test at the same applied pressure P. Tests with a) small aperture diameter (AD_S) and b) large aperture diameter (AD_L).

Since the validated device in Chapters 2 and 3 has a very simple design and does not require any electronic part in the measuring probe, any value for the aperture diameter can be tested. This characteristic enables to push the previous idea much further. In this chapter, our idea is to model the soft tissues heterogeneity in depth by a superposition of N layers over a bulk soft tissue. By performing an FE inverse procedure on the suction tests results of $2N + 1$ suction aperture diameters, each layer thickness, its mechanical properties and the bulk tissue mechanical properties can be identified. Both the superficial layers' thicknesses and mechanical properties of the multi-layered soft tissues can thus be estimated using only a volume-based suction technique; no other system is required to measure the layers' thicknesses.

In this chapter, our method is experimentally validated on synthetic soft silicone specimens comprised of a single superficial layer of Silicone#1 ($N = 1$) over a bulk Silicone#2. The samples were tested with three different suction aperture diameters. An inverse FE method was then implemented to estimate the superficial layer thickness and both materials mechanical properties.

The general principle of the inverse identification process, the suction tests, the preparation of the silicone samples and the "reference" characterization tests (*i.e.* classical experimental tests carried out on the silicones) are thoroughly presented in sections 4.2.1 to 4.2.5. The details about the silicone constitutive model and the FE modeling of the suction tests are then provided in sections 4.2.6 and 4.2.7. The results obtained with each of the reference and inverse characterization methods are presented in section 4.3. Eventually, the identified parameters are compared with the reference measurements in section 4.4.

4.2 Materials and methods

4.2.1 General principle

As mentioned previously, the idea consists in using suction experimental data (section 4.2.2) of three aperture diameters AD (cases 1 to $J = 3$ in Fig. 4.2) to identify the superficial layer thickness (L_1) and the mechanical constitutive parameters of both the superficial and the underlying bulk materials of synthetic specimens.

To achieve this goal, each suction experimental case is compared to its FE simulation counterpart to identify the material parameters and superficial layer thickness L_1 minimizing the function ϕ defined in the least square sense as:

$$\phi = \sum_{j=1}^{J} \sum_{i=1}^{I_j} \left[Sim_{outj}(P_i) - Exp_{outj}(P_i) \right]^2 \tag{4.1}$$

where Sim_{outj} are the data obtained from the FE simulation (section 4.2.7) and Exp_{outj} are the experimental suction test results (section 4.2.2). In Eq. 4.1, j is index of the suction tests with aperture diameters AD_j (Fig. 4.2), P_i is the measured pressure in the ith step and I_j is the number of data points retrieved during test j. Function ϕ thus represents the fitting quality of the pressure-volume curves obtained from the FE simulation (Sim_{outj}) and the experimental suction test (Exp_{outj}) by guessing the set of unknowns Y_i (Fig. 4.2). Y_0 are the initial set of the unknown parameters, Y_i are the

iteratively adapted set of the parameters, and Y_f are the final results of the optimization process. The material parameters in each iteration were guessed using a Nelder-Mead simplex algorithm [Nelder and Mead, 1965] (*fminsearch* procedure in MATLAB). This optimization process was adapted from Weickenmeier, Jabareen, and Mazza, 2015.

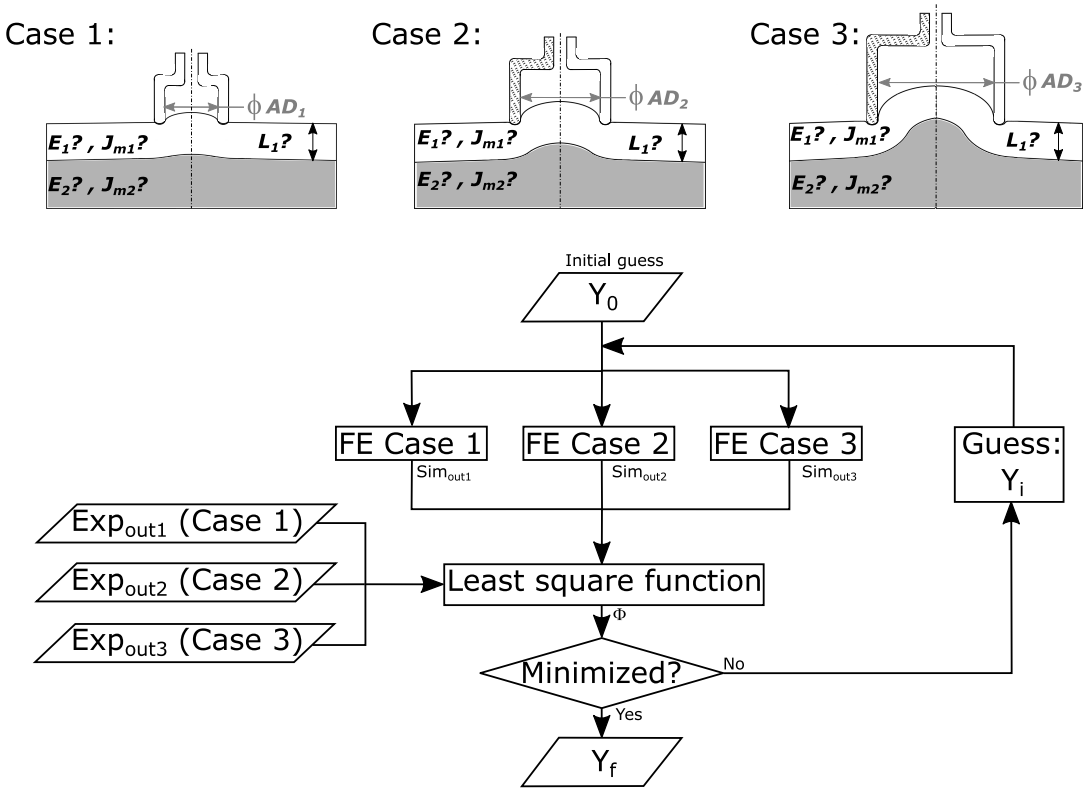

Figure 4.2: Schematic representation of the optimization process for the inverse characterization of the materials parameters and the superficial layer thickness, using aspiration tests with three aperture diameters AD_j. Y are the set of the unknown parameters (here the thickness of the superficial layer L_1 and the Gent constitutive parameters of the two materials E_1, J_{m1}, E_2 and J_{m2}).

4.2.2 Suction device

None of the available suction systems based on optical measurement allow an easy change of the suction aperture diameter. The authors thus developed a measurement method based on volume. Details can be found in [Elahi, Connesson, and Payan, 2018; Elahi et al., 2018]Chapters 2 and 3. The used device is only composed of a suction probe, some connection tubes, a syringe pump and a manometer (Fig. 4.3). The idea consists in aspirating the tissue inside the chamber using the syringe pump, while measuring the negative pressure and the corresponding removed volume V^{total}. Such a volume contains information about both the aspirated tissue volume inside the chamber V_{tissue} and the volume changes in the device V_{system} (air expansion and elasticity of the connections, tubes, syringe, *etc.*). The system volume V_{system} was measured using an off-line calibration process [Elahi et al., 2018]. The aspirated tissue volume V_{tissue} can thus be estimated by:.

$$V_{tissue}(P) = V^{total}(P) - V_{system}(P) \tag{4.2}$$

To check the absence of any leakage at the beginning of the tests, a small stabilized negative pressure (maximum of 5 $mbar$) was applied before each measurement. To prevent application of any significant external load on the suction probe, specific precautions were taken: firstly, the tube connected to the suction probe was chosen to be soft and flexible and could freely move inside a holder (number 6, Fig. 4.3). Secondly, the holder was clamped to a goose neck to offer easy probe positioning (number 5, Fig. 4.3). The external loads due to the suction probe weight was reduced by using very light suction probes (range of 4×10^{-3} to $20 \times 10^{-3} N$) and tubes.

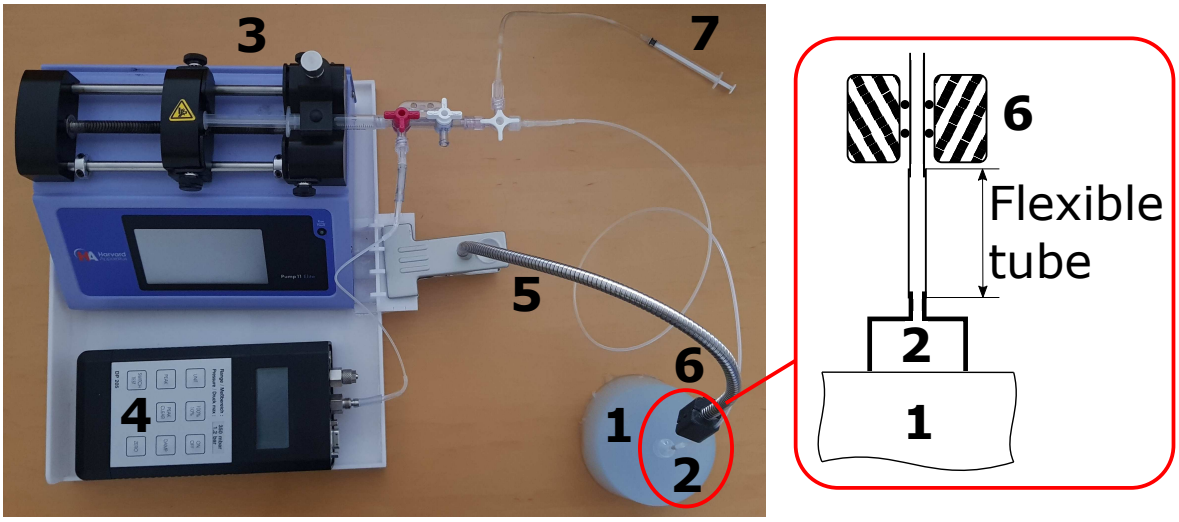

Figure 4.3: Experimental setup for suction tests on the materials: (1) examined material, (2) suction probe, (3) syringe and syringe pump, (4) manometer, (5) goose neck, (6) tube holder and (7) initial pressure syringe.

4.2.3 Samples

In this work, the proof of concept was demonstrated using a specifically designed specimens with a single superficial layer of Silicone#1 over a bulk underneath of Silicone#2. Silicones#1 and #2 are homogeneous and isotropic materials. The superficial layer is of constant thickness ($L_1 << L_2$).

Several synthetic materials have mechanical properties in the same range of human soft tissues [Franceschini et al., 2006; Luboz et al., 2012; Vuskovic, 2001]. RTV-EC00 silicone was chosen due to its ability to generate samples with a very low stiffness (equivalent Young's moduli of the order of some kPa) [Elahi et al., 2018]. The samples were made by mixing two materials' components (base and catalyst) and removing any air bubble from the mixture using a vacuum chamber. The samples were hardened for two weeks at room temperature. The ratio of base and catalyst in the mixture impacts the silicone stiffness; therefore, by modifying this ratio, two soft silicones were obtained:

- Silicone#1: 60% base, 40% catalyst.
- Silicone#2: 40% base, 60% catalyst.

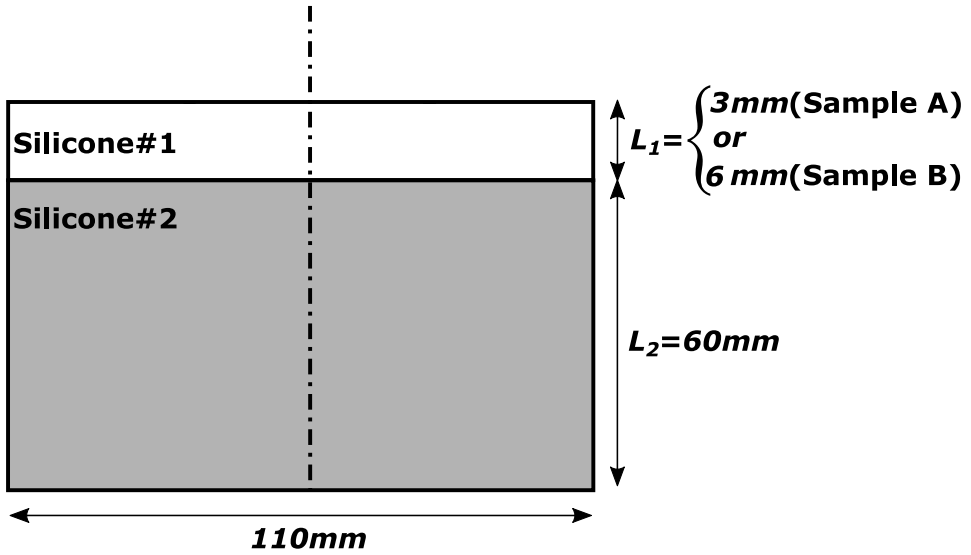

Figure 4.4: Schematic of the fabricated superficial layers over the bulk cylindrical silicone samples.

Eventually, three groups of samples were created by different molds:

1. **Superficial layered samples for suction tests:** two cylindrical samples of 110 mm diameter and height (L_1+L_2) of 63 mm and 66 mm made from Silicone#1 as the superficial layers and Silicone#2 as the bulk underneath (Samples A and B in Fig. 4.4). The superficial layer thicknesses L_1 for the two samples were chosen equal to 3 and 6 mm, respectively. These choices were made to mimic the human skin layer, measured to be in the range of about 1 mm for the facial skin to about 5 mm for the buttocks skin [Herlin et al., 2014]. These skin thickness measurements were performed using Magnetic Resonance Imaging (MRI) method.

   To make the superficial layers over the bulk samples, the material for the bulk underneath was injected into a mold. Before complete hardening of the material, the superficial layer was injected on the top of it.

2. **Homogeneous samples for suction tests:** cylindrical samples of 110 mm diameter and 60 mm height for each of the Silicones#1 and #2.

3. **Samples for tensile and bulge tests:** 2 mm thick membrane cut either into a 50 mm disk or 4 $mm\times100$ mm straps for each of the Silicones#1 and #2.

For each silicone, all the samples were made the same day from the same mixture to ensure the same mechanical properties of the different samples.

4.2.4 Results normalization

Fig. 4.5 illustrates suction measurements on a sample with a superficial layer using small and large aperture diameters (AD_S and AD_L). In the test with small aperture diameter AD_S (Fig. 4.5a), the superficial layer mechanical behavior is mainly measured; for a small enough AD_S, the effect of the deep bulk material on the measured mechanical behavior

becomes negligible. On the other hand, in the test with large aperture diameter AD_L (Fig. 4.5b), both the superficial layer and the under-layer material mechanical behaviors affect the measurement. By increasing the AD_L, relative contribution of the superficial layer in the measured mechanical behavior decreases.

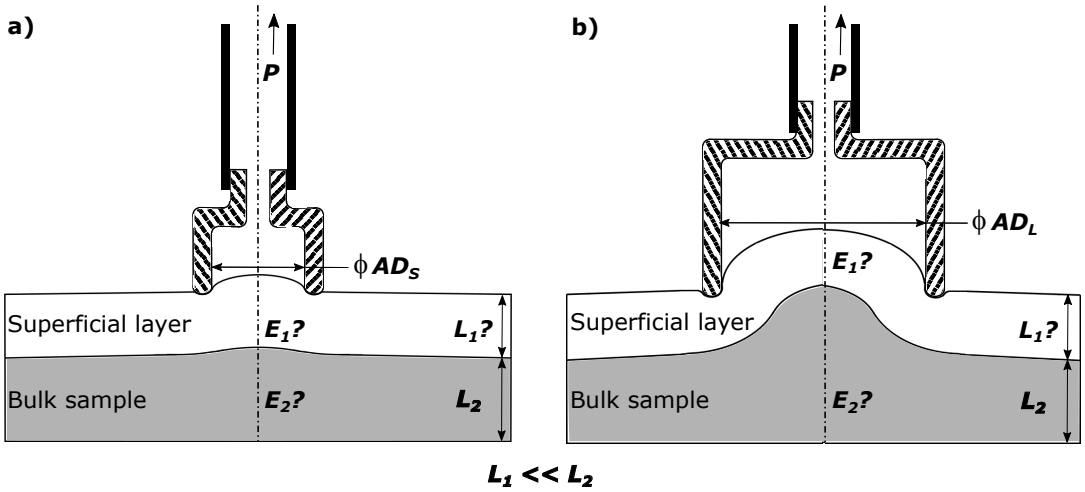

Figure 4.5: Suction measurements on a superficial layer over a bulk sample using a) small and b) large aperture diameters (AD_S and AD_L).

If both Silicones #1 and #2 have the same mechanical behavior, suction test with different aperture diameters provide different pressure-volume curves but contains the same data about the material behavior (Fig. 4.1): performing a suction test on a large bulk material at a pressure P with two different aperture diameters provide the same results relatively to the scale of the aperture diameter. The measured volume V_{tissue} should thus be normalized with respect to the aperture diameter AD, which has been chosen as the volume of a half sphere filling the aperture:

$$Shape = \frac{12\ V_{tissue}}{\pi AD^3} \tag{4.3}$$

This normalization thus define a "shape ratio", since a value equal to one refers to an aspirated tissue volume V_{tissue} equals to half a sphere.

Plotting the suction tests results as pressure-$Shape$ curves will thus show either an in-depth homogeneous behavior (identical curves) or a material gradient (different curves).

To have enough experimental data for the identification of the parameters, the tests on each sample were performed using three suction aperture diameters (AD=4.7, 9.7 and 26.7 mm). These values actually correspond to the diameters of classical syringes which tubes were used to build the three suction probes.

4.2.5 Reference measurements

Once all the aspiration experiments were finished, the superficial layers thicknesses L_1 of the samples (Samples A and B) were pealed and their actual thicknesses were measured at different points using a micrometer for the Samples A and B, respectively.

To identify the "reference" mechanical parameters of the Silicones#1 and #2, two characterization tests were performed on the samples built from the same material used

to create the cylindrical suction tests samples: (i) uniaxial extension test (Fig. 4.6a) and (ii) equibiaxial extension test generated at the top of a bulge test (Fig. 4.6b). The identified parameters were used as references and compared with the inverse identification results (section 4.4.3).

For each silicone material, uniaxial tensile test specimens (100 mm long straps of rectangular section of 4 mm×2 mm) were tested (Fig. 4.6a). A MTS machine (MTS Criterion, Model 41) was used to perform the measurements. Each sample was tested in five loading-unloading cycles up to a maximum strain of 100% to see any possible hysteresis behavior of the silicone materials.

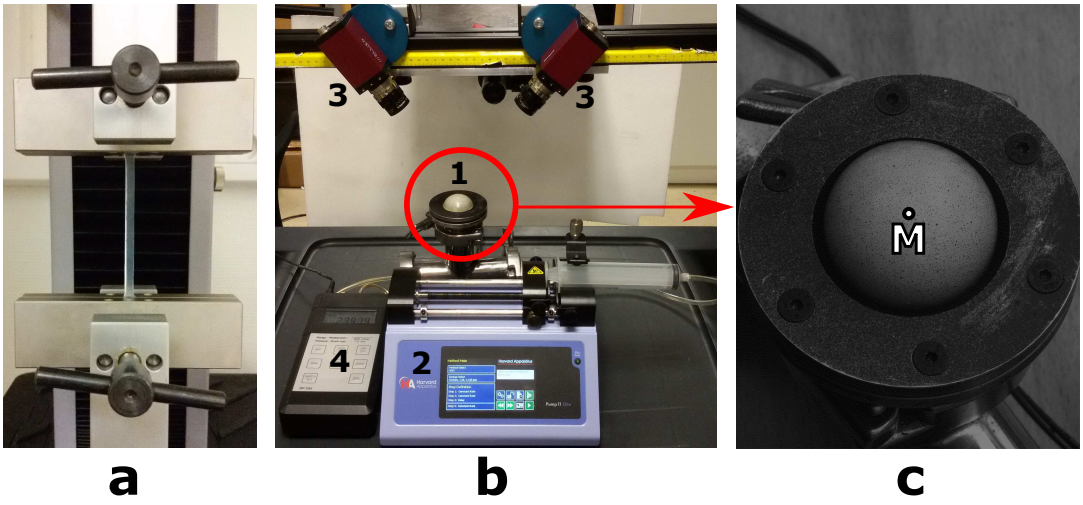

Figure 4.6: a) Tensile test setup, b) Bulge test setup: (1) Bulge membrane and circular clamp, (2) syringe and syringe pump, (3) cameras, (4) manometer and c) close-up of the inflated silicone sample and localization of equibiaxial loading (point M) [Elahi et al., 2018].

The bulge tests were conducted on thin disk specimens of 50 mm diameter (thickness of 2 mm) (Fig. 4.6) [Elahi et al., 2018]. The sample was fixed in the bulge test configuration and inflated by injection of a liquid using the syringe pump. The internal pressure was measured with a manometer. The 3D membrane displacement was tracked using Stereo Digital Image Correlation (SDIC, Figs. 4.6b and 4.6c). The axial-symmetry of the experimental configuration induces the equibiaxiality of the stress and strain state at the top of the inflated membrane (point M, Fig. 4.6c) [Machado et al., 2017]. Since the thickness dimension is 1/25th of the membrane diameter, the in-plane stresses were assumed to be uniform along the thickness dimension. The curvature of the inflated sample was also assumed to be the same along all directions at the disk center due to the system axial-symmetry and material isotropy and homogeneity. In-plane components of First Piola-Kirchhoff stress $\sigma_{xx(Bulge)} = \sigma_{yy(Bulge)}$ at point M can thus be calculated using the following equation [Machado et al., 2017]:

$$\sigma_{xx(Bulge)} = \sigma_{yy(Bulge)} = \frac{pr}{2e_0}\lambda_{(Bulge)}; \quad \sigma_{zz(Bulge)} = 0 \tag{4.4}$$

where e_0 is the initial thickness of the specimen, r the local curvature radius, $\lambda_{(Bulge)} = \lambda_{xx} = \lambda_{yy}$ the principal stretch and p the pressure recorded during the test.

In order to see any possible hysteresis behavior of the materials, each sample was tested during five inflating-deflating cycles up to a maximum strain of about 70%.

4.2.6 Material constitutive model

A hyperelastic Gent model [Gent, 1996] was selected to model each silicone behavior during both suction and classical tests. This model was previously used to model the silicone rubbers [Chagnon, Marckmann, and Verron, 2004]. The strain energy function of the Gent model (W_G) is given by:

$$W_G = -\frac{EJ_m}{6} \ln\left(1 - \frac{I_1 - 3}{J_m}\right) \tag{4.5}$$

where E and J_m are the two material parameters and I_1 is the first Cauchy Green strain invariant. J_m represents the maximum value of (I_1-3) that can be undergone by the material. The Gent model was used to simulate the materials parameters either using the FE method (suction test, section 4.2.7) or to identify the materials parameters from the classical characterization results (tensile and bulge tests, section 4.3.2).

4.2.7 FE modeling of the suction test

A FE simulation of the suction tests on the samples was performed (ANSYS software) in order to simulate the experimental cases 1 to 3 (Fig. 4.2).

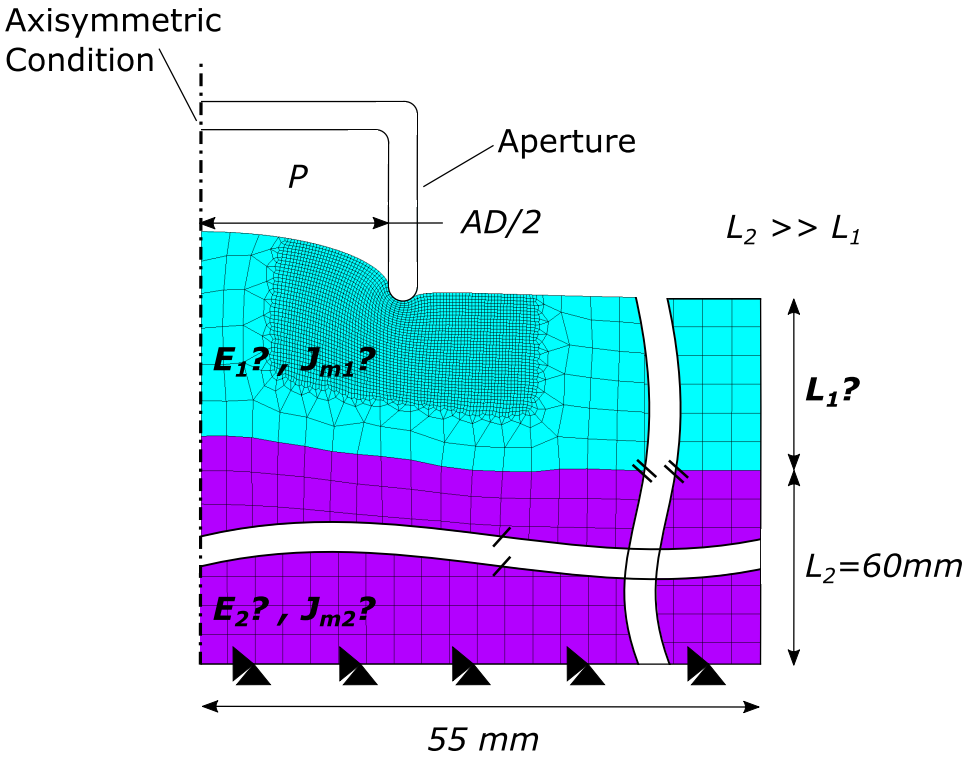

Figure 4.7: Schematic of the FE model and associated boundary conditions. Example of displacement results.

The materials were assumed to be nearly incompressible. The tests were modeled in 2D with axisymmetry (Fig. 4.7). As the silicone cylinder diameter and height were respectively at least about 4.2 and 2.2 times larger than the aperture diameter (section 4.2.3), boundary conditions on the bottom and the outer sides of the tissue structure do not have any effect on the simulations results. Yet, the bottom layer of the nodes was fixed for horizontal and vertical displacements and the outer side of the tissue was allowed to move freely. The sample was meshed with Quadratic 8-node (Q8) elements. The contact properties between the suction probe and the material surface were modeled as a frictionless contact. The displacement of the tissue surface inside the aperture was used to compute the aspirated volume at each pressure step.

4.3 Parameters identification results

4.3.1 Reference thicknesses

The reference measurements of superficial layers thicknesses L_1 for Samples A and B were: L_{ref1}=3.02±0.03mm and 6.08±0.09mm, respectively. The values after the ± signs represent STandard Deviation (STD) of the measurements at different points of the samples' superficial layers.

4.3.2 Reference material parameters

The parameters of the Gent model were identified using the classical tests for Silicones#1 and #2 as references. The Fist Piola-Kirchhoff stress-stretch relations were calculated based on Eq. 4.5 for uniaxial and equibiaxial extensions, respectively as:

$$\sigma_{xx(uni)} = \left(\lambda_{(uni)}^2 - \frac{1}{\lambda_{(uni)}}\right)\left[\frac{EJ_m/3}{(J_m+3)\lambda_{(uni)} - \lambda_{(uni)}^3 - 2}\right] \tag{4.6}$$

and

$$\sigma_{xx(equi)} = \sigma_{yy(equi)} = \left(\lambda_{(equi)}^5 - \frac{1}{\lambda_{(equi)}}\right)\left[\frac{EJ_m/3}{(J_m+3)\lambda_{(equi)}^4 - 2\lambda_{(equi)}^6 - 1}\right] \tag{4.7}$$

where $\sigma_{xx(uni)}$ and $\sigma_{xx(equi)}$ are stresses and $\lambda_{(uni)}$ and $\lambda_{(equi)}$ are stretches in uniaxial and equibiaxial extensions, respectively.

The reference model parameters for each material were estimated by minimizing simultaneously the errors between Eqs. 4.6 and 4.7 and the experimental results of the uniaxial tensile and bulge tests, respectively.

The stress-strain curves of the five-cycle uniaxial tensile tests on Silicones#1 and #2 are presented in Fig. 4.8a. These results show that both materials have no hysteresis behavior.

The stress-strain results of the five-cycle bulge tests on Silicones#1 and #2 are plotted in Fig. 4.8b. As previously, no hysteresis behavior can be observed in these results and behavior differences between samples during the five-cycle tests on each material are indiscernible.

Gent model curves for uniaxial and equibiaxial extensions were respectively fitted to the tensile and bulge tests data of each silicone material (Figs. 4.8a and 4.8b). Both fittings for each silicone were performed simultaneously to estimate the best model parameters (E and J_m) as given in Table 4.1.

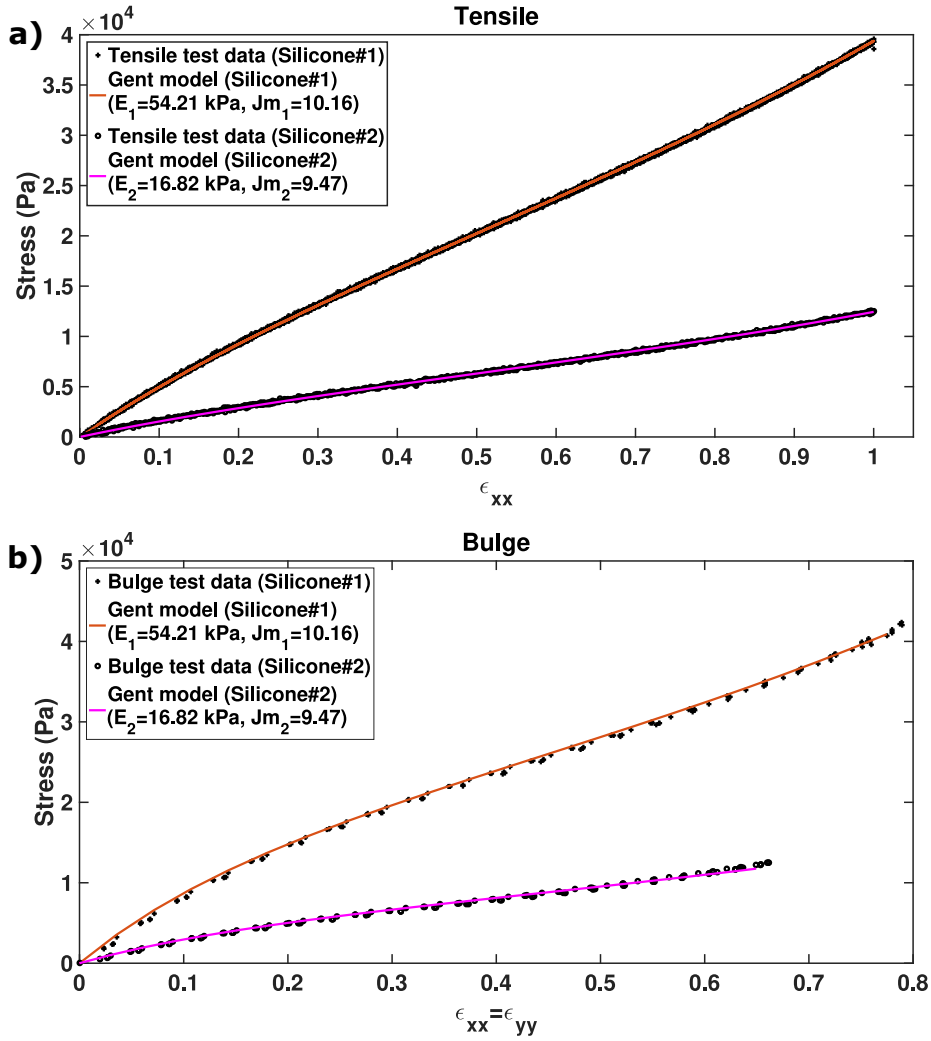

Figure 4.8: Stress-strain results and fitted Gent model for Silicones#1 and #2 (five cycles for each): a) tensile tests and b) bulge tests.

4.3.3 Suction tests results

To study quasi-static mechanical behavior for the tested materials in the suction tests, the changes in the volume were applied with the very low rate of 0.4 ml/min [Elahi et al., 2018]. The reproducibility of the results was checked by repeating each suction test nine times in the same condition. The STandard Deviation (STD) of the volume measurements V_{tissue} was calculated for each set of the nine tests and used as a parameter to assess the measurement precision and reproducibility.

The pressure-*Shape* data of the suction tests using the three different aperture diameters AD on the homogeneous sample made of Silicone#2 are plotted in Fig. 4.9. The

obtained results validate the hypothesis about the identical pressure-*Shape* curves for the suction tests with different aperture diameters AD on a homogeneous sample.

Results of the volume-based suction tests on the homogeneous samples made of Silicones#1 or #2 are compared with the tests results of the samples with superficial layers in Figs. 4.10a and b. Average of the nine experimental pressure-*Shape* (Eq. 4.3) measurements for each curve is presented. The STD of the volume measurements according to the average values was between 0.25% (Sample B with AD=26.7 mm) and 2.87% (Sample A with AD=4.7 mm). The low STD of the measurements shows the reproducibility of the experimental data.

In order to identify the upper layer thickness L_1 and the Gent model materials parameters of the samples with superficial layers using the optimization process (section 4.2.1), the unknown parameters were defined as:

$$Y = \left\{ \begin{array}{c} \left\{ \begin{array}{c} L_1 \\ E_1 \\ J_{m1} \end{array} \right\} \\ \left\{ \begin{array}{c} E_2 \\ J_{m2} \end{array} \right\} \end{array} \right\} \tag{4.8}$$

where Y includes two groups of parameters: (i) the superficial layer thickness L_1 and material model constants (E_1 and J_{m1}), and (ii) the bulk material model constants (E_2 and J_{m2}).

The identified parameters using the optimization procedure are compared with the reference measurements in Table 4.1.

Table 4.1: Comparison of the identified parameters and the reference measurements.

Samples	Parameters	Reference measurements	Identified	Identification error (%)
Sample A	L_1 (mm)	3.02±0.03	3.13	[2.6, 4.5]
	E_1 (kPa)	54.21	52.98	2.3
	J_{m1}	10.16	10.05	1.1
	E_2 (kPa)	16.82	15.37	8.6
	J_{m2}	9.47	9.32	1.6
Sample B	L_1 (mm)	6.08±0.09	6.05	[1.0, 2.0]
	E_1 (kPa)	54.21	57.89	6.8
	J_{m1}	10.16	10.21	0.5
	E_2 (kPa)	16.82	15.61	7.2
	J_{m2}	9.47	9.36	1.2

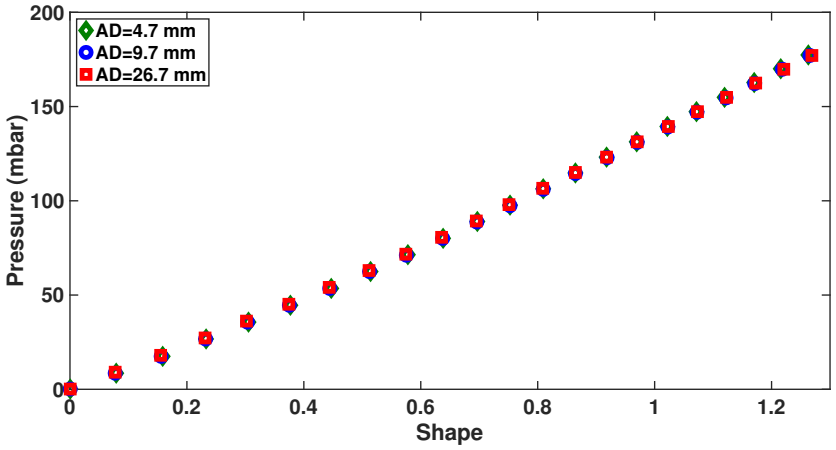

Figure 4.9: Pressure-*Shape* data of the suction tests using the three different aperture diameters *AD* on the homogeneous sample made of Silicone#2.

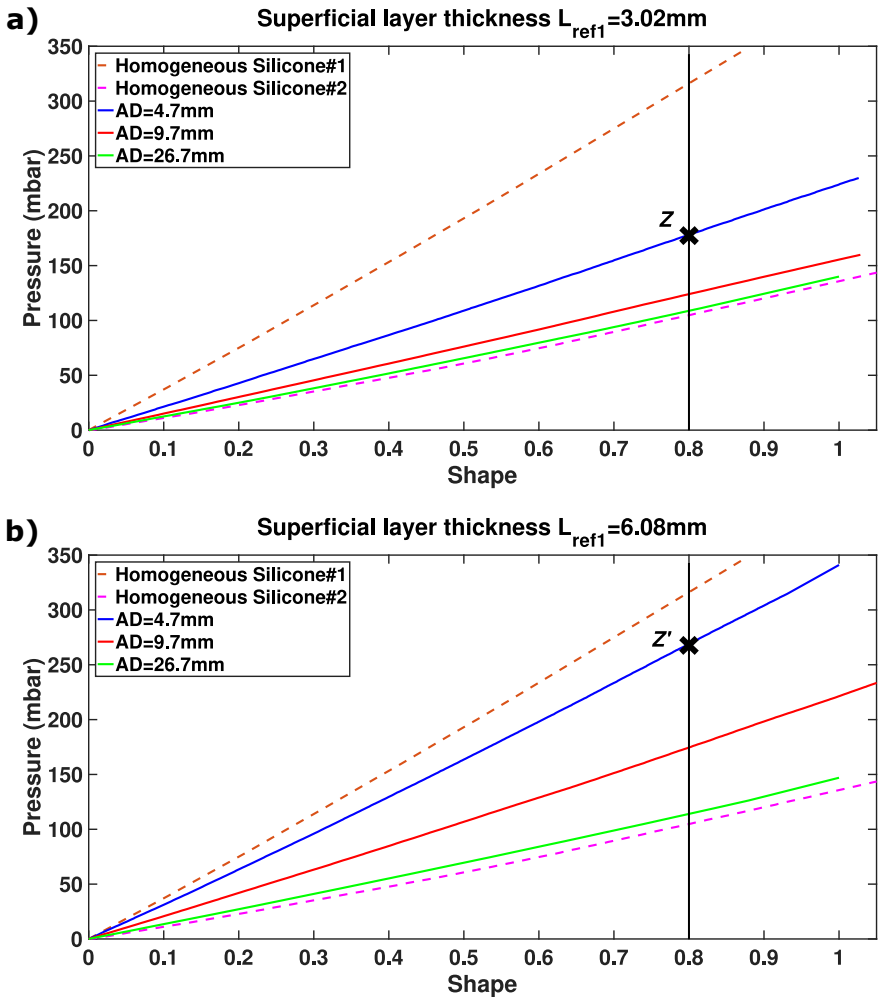

Figure 4.10: Pressure-*Shape* averaged curves of suction measurements for homogeneous samples made of Silicones#1, #2 and samples with superficial layers using different aperture diameters: a) sample A and b) sample B.

4.4 Discussion

4.4.1 Experimental suction tests results

In Fig. 4.10a different pressure-*Shape* curves were obtained from the tests with different aperture diameters AD on the samples with superficial layer. The in-depth mechanical gradient was thus highlighted during the suction tests: homogeneous mechanical properties would provide identical pressure-*Shape* curves (Fig. 4.9). Similar results were obtained for the sample with thicker superficial layer (Fig. 4.10b). In particular, the volume-based suction method is able to clearly highlight the different behaviors of the superficial layered samples during the tests thanks to the different suction aperture diameters AD. The following experimental observations (from Figs. 4.10a and b) validate the quality of the volume-based suction measurements:

- The superficial layered specimen curves should be located between the curves of its constitutive materials (homogeneous Silicones#1 and #2). In the suction tests on the superficial layered samples, using small aperture diameters AD mainly load the superficial layer: the pressure-*Shape* curve is thus closer to the superficial layer material curve (homogeneous Silicone#1 in Fig. 4.10). On the other hand, in the tests with larger aperture diameters AD the depth of loaded material increases. The pressure-*Shape* curves for the tests with large aperture diameters AD are thus closer to the underneath material curve (homogeneous Silicone#2 in Fig. 4.10).

- Since Silicone#1, used to make the superficial layers, was stiffer in comparison to the Silicon#2, increasing the superficial layer thickness L_1 creates an overall stiffer specimen. Comparison of the tests with the same aperture diameter AD on the Samples A and B (Figs. 4.10a and b) shows that more pressure P was needed to have the same *Shape* for Sample B with thicker superficial layer (point Z') than for Sample A (point Z).

4.4.2 Comparison of numerical and experimental results

The direct comparison of experimental and numerical curves for Samples A and B reveal good agreements (Figs. 4.11 and 4.12). These numerical simulations were performed using the final identified data (Table 4.1). The presented results validate the proper identification of the superficial layer thickness L_1 and material parameters for Samples A and B. Moreover, the results highlight the adequacy of the chosen constitutive model equation (Eq. 4.5).

4.4.3 Comparison of the identified and reference parameters

In this paper, for the first time, a method was proposed to identify the superficial layers thicknesses in multi-layer soft tissues using only suction tests results. The average identification errors of the superficial layer thickness L_1 using the proposed method for Samples A and B are 3.6% and 0.5%, respectively (Table 4.1). These results validate the ability of the volume-based suction method for accurate measurement of the superficial layer thickness L_1. Consequently, it seems that there is no need additional methods to measure the superficial layer thickness, as it was proposed previously [Barbarino, Jabareen,

and Mazza, 2011; Weickenmeier, Jabareen, and Mazza, 2015]. In addition, according to Table 4.1, the superficial layer thickness L_1 was identified more accurately for Sample B (with $L_{ref1} = 6.08mm$ and maximum error of 2.0%) in comparison with Sample A (with $L_{ref1} = 3.02mm$ and maximum error of 4.5%). This is probably due to the fact that the thicker superficial layer provided more contrast for the chosen aperture diameters AD (Fig. 4.10).

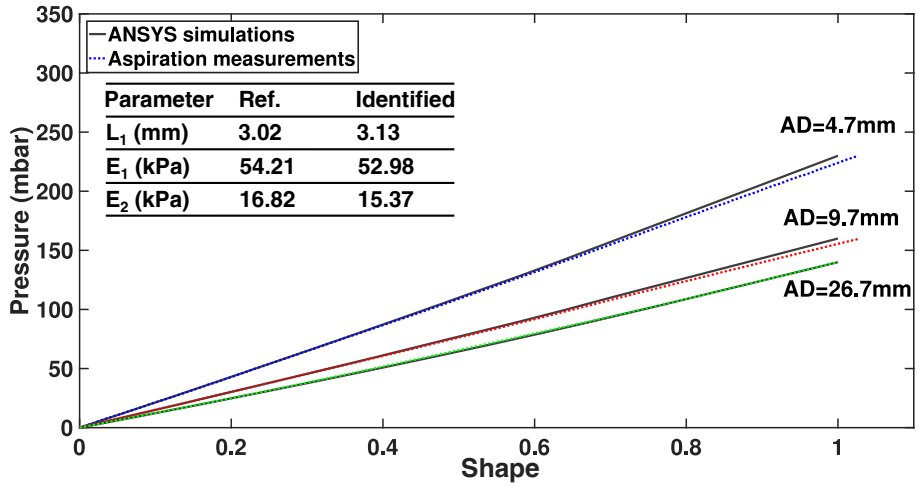

Figure 4.11: Comparison of the suction measurements averages and the corresponding FE simulation results based on the identified material model parameters for sample A.

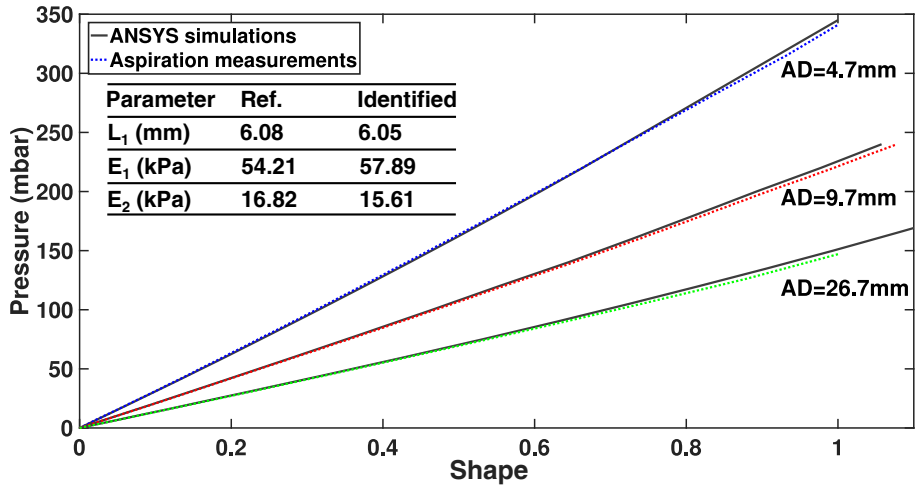

Figure 4.12: Comparison of the suction measurements averages and the corresponding FE simulation results based on the identified material model parameters for sample B.

The suction tests results are most often used to estimate Young's moduli of soft tissues [Luboz et al., 2012; Weickenmeier, Jabareen, and Mazza, 2015]. The identified Young's moduli are compared with the reference Young's moduli in Table 4.1 based on the tests on Samples A and B. Results show identification errors of 2.3% and 6.8% for

the superficial layer Young's moduli (E_1) of Samples A and B, respectively. Errors for the underneath silicone (E_2) of Samples A and B are 8.6% and 7.2%, respectively.

For comparison, the experimental data from aspiration measurements were used to estimate Young's moduli of silicones assuming a Neo-Hookean model [Luboz et al., 2012]. A difference of about 30% between inverse characterization (using the optical aspiration device LASTIC) and classical characterization of silicone materials with a similar range of elasticity was obtained. This indicates four times improvement using the volume-based method, even if the measurements in this work were performed on samples with superficial layers: despite the presence of the superficial layer, the mechanical properties of the deeper tissue were identified with a maximum error of only 8%, which is considered very encouraging.

4.5 Conclusion

This chapter validated a novel method for *in-vivo* mechanical identification of soft tissues with one superficial layer over a bulk of tissue. Using the proposed method, the superficial layer thickness, its mechanical properties and the bulk tissue mechanical properties can be obtained using only the volume-based suction measurements.

This method could be straightforwardly extended to identify the thicknesses and mechanical properties of multi-layered soft tissues (N layers over a bulk tissue) by increasing the number of tested aperture diameters. Identifying these parameters over N layers would thus require the use of $2N + 1$ properly chosen aperture diameters.

To validate the method, synthetic samples with one superficial layer ($N = 1$) over a bulk material were made using two silicone materials with different stiffnesses. To study in-depth gradient of the mechanical properties, the samples were tested during suction experiments with different aperture diameters. Each suction test was performed nine times and STD percentage ranges of 0.2% to 2.9% were obtained.

The superficial layer thickness and materials parameters were identified using an FE updating inverse method on the suction experiment results. To assess the identification quality, the silicone samples were tested using classical uniaxial and equibiaxial extension tests, as references. The results give maximum identification errors of 3% and 8% for the superficial layer thickness and mechanical characteristics, respectively.

According to the authors, it is the first time that suction method is used to identify the superficial layer thickness along with their mechanical properties. Moreover, comparison of the mechanical parameters identification error with the literature indicates a significant accuracy improvement. It is hoped that these results will open the door to extensive *in-vivo* measurements on various regions of the human skin, assuming a two-layer structure of human skin (mainly represented by dermal and sub-dermal tissues). This could provide subject-specific values for constitutive parameters of these two layers as well as for the thickness of the dermal tissues.

This method can also be used in order to identify the mechanical properties of multi-layered internal human tissues, such as liver and uterus. Due to the time limits during the intra-operative measurements the computation time for inverse identification plays an important rule. The used inverse identification procedures in Chapters 3 and 4 take from one hour to a few hours to be performed, which make them impossible to be used for intra-operative measurements. Chapter 5 presents a real-time inverse identification

method in order to reduce the computation time of the inverse identifications to a few seconds.

CHAPTER

FIVE

REAL-TIME INVERSE IDENTIFICATION

Contents

5.1 Introduction

In-vivo characterization of the associated mechanical parameters of soft tissues should be performed in real-time to feed biomechanical simulations during intra-operative assisted surgery.

In the previous chapters, an original volume-based aspiration device was introduced. The experimental data collected from the aspiration tests could not be analyzed in real-time to identify material parameters of the constitutive models. Indeed, the used inverse method required at least one FE simulation (homogeneous silicones of Chapter 3) per iteration and more than 100 iterations. The corresponding CPU time was about one hour using an eight core computer with a frequency of 2.6 GHz. When a N layer material is analyzed, it requires at least $2N+1$ simulations per iteration, thus drastically increasing the required CPU time up to a few hours.

This chapter focuses on introducing a method for real-time inverse characterization of soft tissues using the volume-based aspiration experimental results. To reach this goal, a Design Of Experiment (DOE) method was adapted from Frauziols et al., 2016. The method consists in fitting an approximating polynomial function to the FE simulation results. Using the fitting function instead the FE simulations during the inverse identification procedure, the calculation time was drastically decreased to a few seconds.

Eventually, the parameters of the fitting function provide a mean to study the experiments sensitivity to various parameters.

In this chapter, to describe the used DOE method, a simple mechanical problem is employed. The methodology is first presented to solve this problem (section 5.2). Applications of the proposed method are then demonstrated on experimental aspiration tests of the homogeneous silicone samples of Chapter 3 and two-layer silicone samples of Chapter 4 (section 5.3). The inverse identifications using the DOE method were compared with the reference materials parameters obtained in Chapters 3 and 4 and differences of 10 and 12% were obtained for homogeneous and two-layer silicones, respectively.

5.2 Methodology

5.2.1 Problem definition

To describe the method, a simple mechanical problem is analyzed (Fig. 5.1): an elastic cantilever beam, denoted "$beam^0$" is clamped to a wall. Its free end is then subjected to a point load F. The deflection (δ^0_{exp}) at the load application point is the experiment output. The beam cross-section width $w = 0.1m$ and the material Young's Modulus $E = 100GPa$ are known. The goal is to use the deflections δ^{0k}_{exp} for different loads F_k on $beam^0$ to identify its cross-section height h_0 and length L_0, assuming the analytical solution is not known.

To achieve this, the experimental results δ^{0k}_{exp} on $beam_0$ are compared to a set of numerical results δ^i_{num} of known beams with different cross-section heights h_i, lengths L_i and loaded with different point loads F_i. In this beam illustration, the set of these

numerical results δ^i_{num} will be generated using the exact theoretical solution, given by:

$$\begin{aligned} \delta_{theo} &= -\frac{FL^3}{3EI} \\ I &= \frac{wh^3}{12} \end{aligned} \tag{5.1}$$

For more complex problems for which no analytical solution exists (like aspiration tests), FE simulations are used to compute the numerical results.

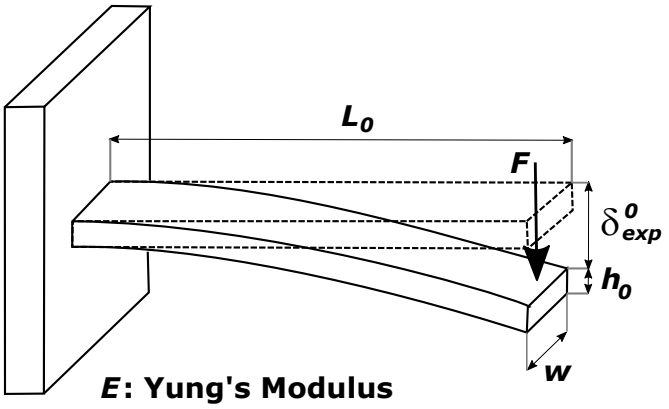

Figure 5.1: Schematic of defined simple beam problem for describing the DOE method.

5.2.2 Approximating function

In such a problem, there are three types of parameters:

- **Type 1:** Known and stable parameters during experiments (example: cross-section width w and Young's modulus E).
- **Type 2:** Unknown parameters, which have to be the outputs of the inverse identification (example: cross-section height h and length L).
- **Type 3:** Experimental set of parameters, which are input and outputs of the experiments (example: $[F_k,\, \delta^{0k}_{exp}]$).

In order to identify the unknown parameters using the DOE, the experimental output δ^0_{exp} is approximated using a linear polynomial function of types 2 and 3 variables (h, L and F) and their binary interactions:

$$\begin{aligned} \delta_{approx}(h, L, F) =& \gamma_0 + \gamma_h h + \gamma_L L + \gamma_F F + \\ & \gamma_{hL} hL + \gamma_{Fh} Fh + \gamma_{FL} FL \end{aligned} \tag{5.2}$$

The 7 coefficients (γ_j) of Eq. 5.2 have to be identified using a set of reference values δ^i_{num}. With such a polynomial function, a set of at least 7 reference values δ^i_{num} is required. The DOE method proposes to use $2^3 + 1 = 9$ set of values (h_i, L_i and F_i) based on the full factorial design. This will be discussed later in the text.

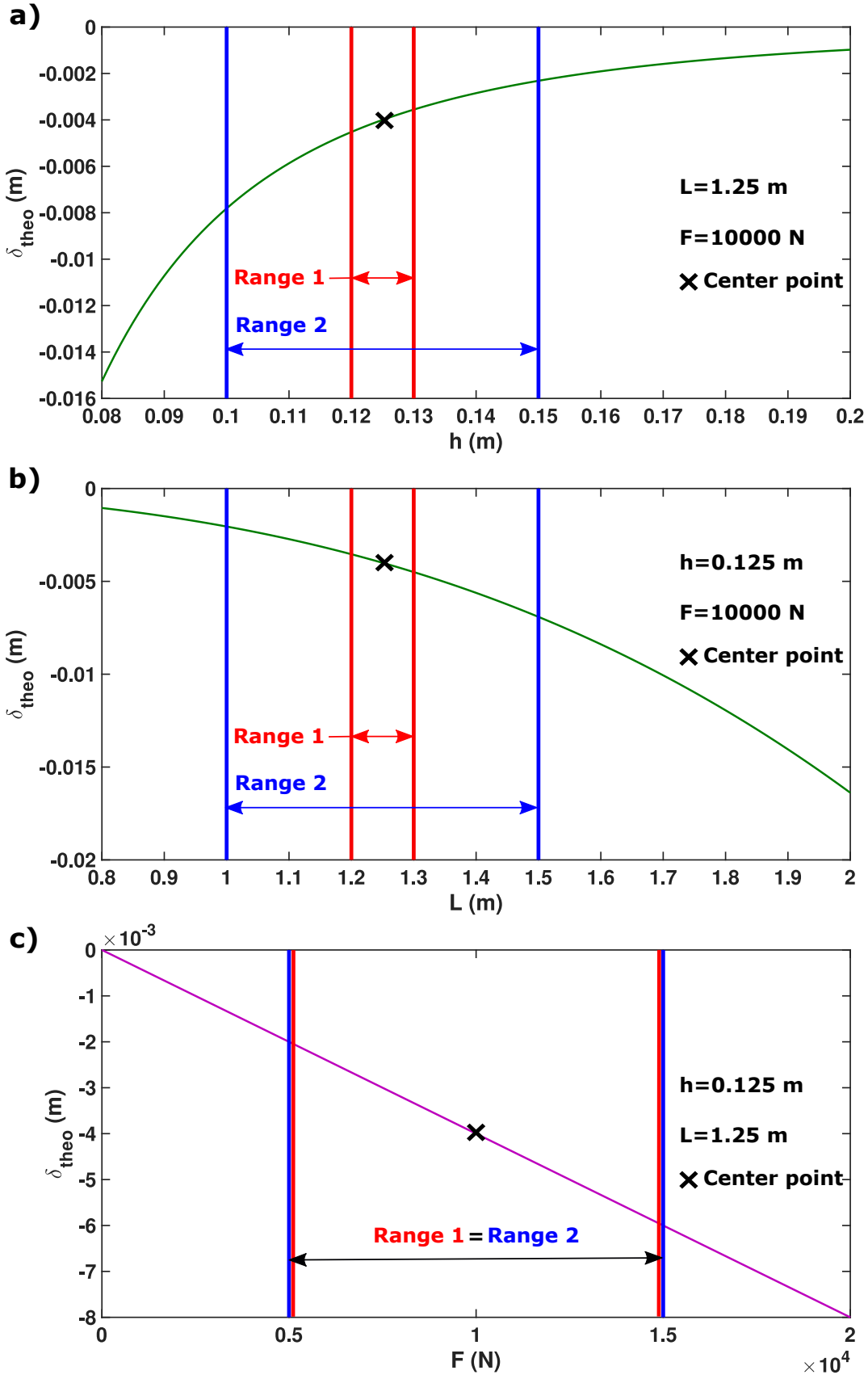

Figure 5.2: δ_{theo} versus a) h, b) L and c) F curves using Eq. 5.1. The chosen Ranges 1 and 2 are illustrated for each variable.

In this beam example, it is yet obvious that the first order polynomial δ_{approx} (Eq. 5.2) is ill designed to fit properly the actual displacement δ_{theo} (Eq. 5.1). This linear approximation will be correct only locally, if the set of reference values δ^i_{num} is defined on a small enough domain for the three variables (h_i, L_i and F_i) and if the desired solution (h_0 and L_0) is contained in this domain.

An illustration of this approximation quality is proposed in Fig. 5.2, plotting δ_{theo} around an arbitrary chosen center of domain ($h = 0.125m, L = 1.25m$ and $F = 10000N$). In this case, selecting Range 1 (the smaller range) for the variables domains will induce less error in the linear approximation than selecting Range 2.

Since δ_{theo} (Eq. 5.1) is a linear function of F, the two ranges were selected to be the same for this variable. The chosen Ranges 1 and 2 of the variables that contain the expected desired values h_0 and L_0 are respectively given in Tables 5.1 and 5.2.

Table 5.1: Range 1 of the variables domains.

Parameters	Minimum	Center	Maximum
$h(m)$	0.12	0.125	0.13
$L(m)$	1.2	1.25	1.3
$F(N)$	5000	10000	15000

Table 5.2: Range 2 of the variables domains.

Parameters	Minimum	Center	Maximum
$h(m)$	0.1	0.125	0.15
$L(m)$	1	1.25	1.5
$F(N)$	5000	10000	15000

Following the DOE method, any variable x can be normalized in its respected range from -1 to 1 using the following equation:

$$x^* = \frac{2x - (x_{max} + x_{min})}{x_{max} - x_{min}} \tag{5.3}$$

where x^* is the normalized variable and x_{max} and x_{min} are the maximum and minimum of the variable range, respectively.

Normalizing the variables, the δ_{approx} given by Eq. 5.2 can be rewritten as:

$$\begin{aligned}\delta_{approx} =& \beta^*_0 + \beta^*_{h^*} h^* + \beta^*_{L^*} L^* + \beta^*_{F^*} F^* + \\ & \beta^*_{h^*L^*} h^* L^* + \beta^*_{F^*h^*} F^* h^* + \beta^*_{F^*L^*} F^* L^*\end{aligned} \tag{5.4}$$

The problem was thus changed from identifying the coefficients γ_j in Eq. 5.2 into identifying the coefficients β^*_j in Eq. 5.4.

The set of experiments δ^i_{num} was defined using a full factorial design with interactions and provided n set of parameters h^*, L^* and F^*:

$$n = 2^m + 1 \tag{5.5}$$

where m is the number of variables ($m = 3$ in this beam example which means $n = 9$). The 9 experiments corresponding to the 9 sets of parameters were performed using

permutations of the minimum and maximum values of the variables' ranges and using and additional point at the center of the domain (Table 5.3).

Table 5.3: Tested parameters and obtained results for each of the Ranges 1 and 2.

Test No. (i)	h^*	L^*	F^*	δ^i_{num} (m) [Range 1]	δ^i_{num} (m) [Range 2]
1	0	0	0	-4×10^{-3}	-4×10^{-3}
2	1	1	1	-6×10^{-3}	-6×10^{-3}
3	-1	1	1	-7.6×10^{-3}	-2.02×10^{-2}
4	1	-1	1	-4.7×10^{-3}	-1.8×10^{-3}
5	-1	-1	1	-6×10^{-3}	-6×10^{-3}
6	1	1	-1	-2×10^{-3}	-2×10^{-3}
7	-1	1	-1	-2.5×10^{-3}	-6.7×10^{-3}
8	1	-1	-1	-1.6×10^{-3}	-5.9×10^{-4}
9	-1	-1	-1	-2×10^{-3}	-2×10^{-3}

The approximation error $\epsilon_{(i)}$ at each of the test points can be written as:

$$\epsilon_{(i)} = \delta^i_{approx} - \delta^i_{num} \tag{5.6}$$

The coefficients β^*_j are identified in the least mean square sense so as to minimize the cost function:

$$CF_1 = \sum_{i=1}^{n} (\epsilon_{(i)})^2 = \sum_{i=1}^{n} (\delta^i_{approx} - \delta^i_{num})^2 \tag{5.7}$$

The cost function CF_1 is then minimized according to the coefficients of Eq. 5.4:

$$\frac{\partial CF_1}{\partial \beta^*_j} = 0, \forall j \in [0, h^*, L^*, F^*, F^*h^*, F^*L^*, h^*L^*] \tag{5.8}$$

Solving this system of equations gives:

$$\begin{aligned}
\beta^*_0 &= \overline{\delta^i_{num}} \\
\beta^*_{h^*} &= \frac{1}{8}(\delta^2_{num} - \delta^3_{num} + \delta^4_{num} - \delta^5_{num} + \delta^6_{num} - \delta^7_{num} + \delta^8_{num} - \delta^9_{num}) \\
\beta^*_{L^*} &= \frac{1}{8}(\delta^2_{num} + \delta^3_{num} - \delta^4_{num} - \delta^5_{num} + \delta^6_{num} + \delta^7_{num} - \delta^8_{num} - \delta^9_{num}) \\
\beta^*_{F^*} &= \frac{1}{8}(\delta^2_{num} + \delta^3_{num} + \delta^4_{num} + \delta^5_{num} - \delta^6_{num} - \delta^7_{num} - \delta^8_{num} - \delta^9_{num}) \\
\beta^*_{h^*L^*} &= \frac{1}{8}(\delta^2_{num} - \delta^3_{num} - \delta^4_{num} + \delta^5_{num} + \delta^6_{num} - \delta^7_{num} - \delta^8_{num} + \delta^9_{num}) \\
\beta^*_{F^*h^*} &= \frac{1}{8}(\delta^2_{num} - \delta^3_{num} + \delta^4_{num} - \delta^5_{num} - \delta^6_{num} + \delta^7_{num} - \delta^8_{num} + \delta^9_{num}) \\
\beta^*_{F^*L^*} &= \frac{1}{8}(\delta^2_{num} + \delta^3_{num} - \delta^4_{num} - \delta^5_{num} - \delta^6_{num} - \delta^7_{num} + \delta^8_{num} + \delta^9_{num})
\end{aligned} \tag{5.9}$$

Repeating the described procedure for each of the selected Ranges 1 and 2 give an approximating function δ_{approx} for each range.

5.2.3 Validation criteria

To visually assess the quality of the approximating function δ_{approx}, its curves versus each approximating function variable (h, L and F) should be compared, if possible, with the corresponding values of δ_{num}. For each of the Ranges 1 and 2 the curves were plotted versus each variable in its selected range, while the two other variables were at the centers of their ranges (Figs. 5.3 and 5.4, respectively). The curves versus the variable F were not plotted due to the perfectly linear behavior of δ_{theo} according to this variable.

The maximum mismatches between δ_{approx} and δ_{theo} curves for the Range 1 (Fig. 5.3) is about 40 times lower (Fig. 5.3) than the maximum mismatch for the Range 2 (Fig. 5.4). This confirms that an appropriate selection of a range for the variables, in which the experimental output is closer to the linear behavior approximation, increases the approximating function accuracy significantly.

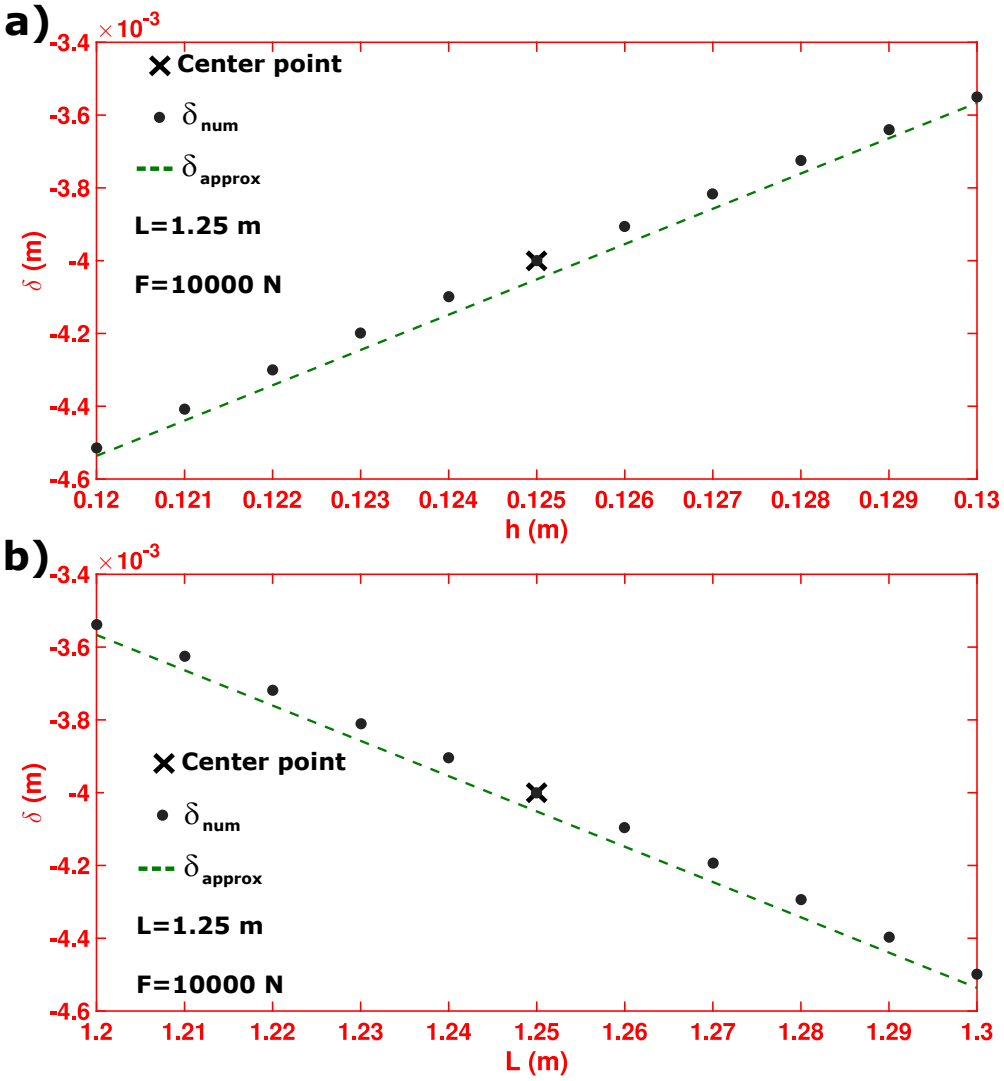

Figure 5.3: Comparison of δ_{num} and δ_{approx} versus h and L curves for arbitrary chosen Range 1: a) while h changes in its domain and L and F are at their domains centers and b) while L changes in its domain and h and F are at their domains centers.

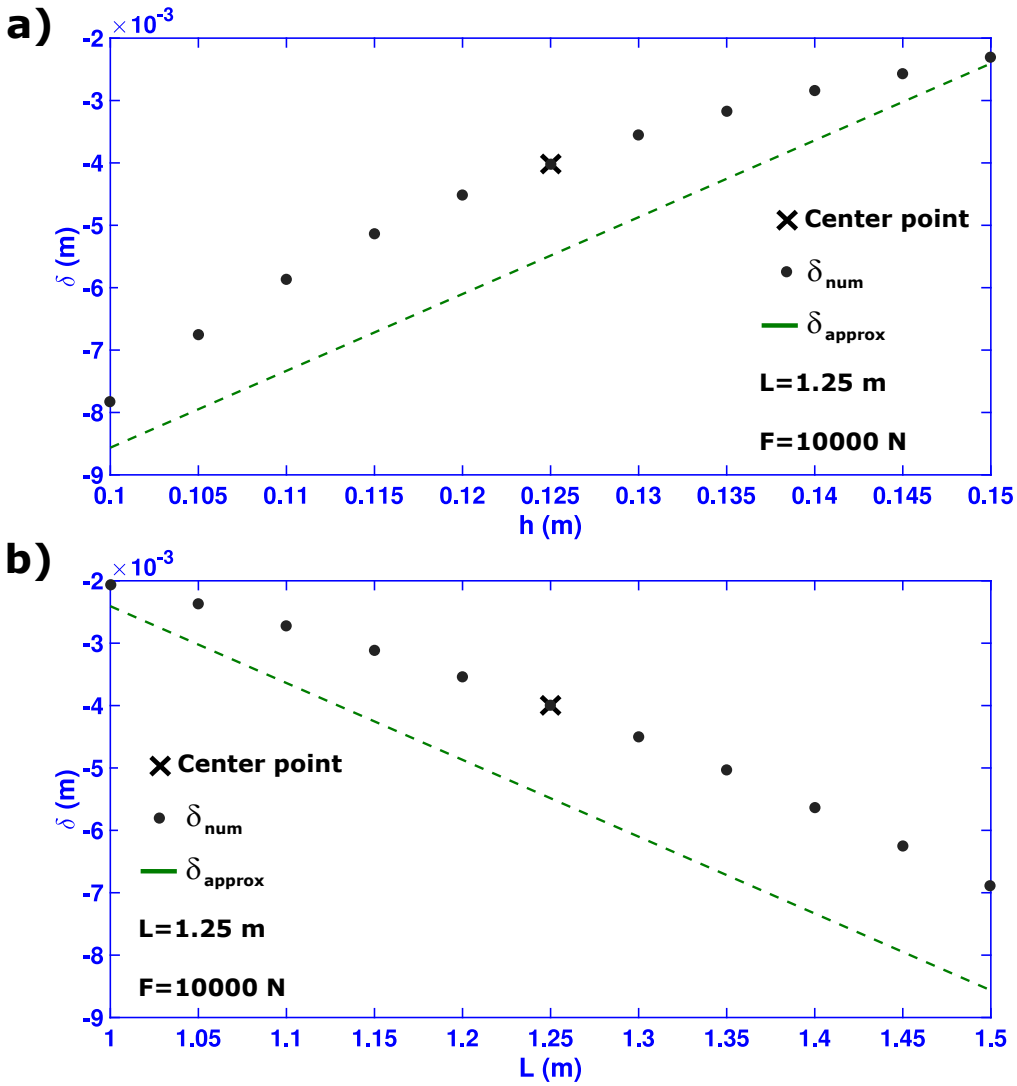

Figure 5.4: Comparison of δ_{num} and δ_{approx} versus h and L curves for arbitrary chosen Range 2: a) while h changes in its domain and L and F are at their domains centers and b) while L changes in its domain and h and F are at their domains centers.

To assess the quality of the approximating function δ_{approx} statistically, an ANalysis Of VAriance (ANOVA) was proposed by Frauziols et al., 2016. Variance of the n numerical data can be calculated as:

$$var = \frac{\sum_{i=1}^{n} \left(\delta_{num}^{i} - \overline{\delta_{num}^{i}}\right)^2}{n-1} \tag{5.10}$$

The numerator of the variance can be approximated as:

$$\underbrace{\sum_{i=1}^{n} \left(\delta_{num}^{i} - \overline{\delta_{num}^{i}}\right)^2}_{SST} \simeq \underbrace{\sum_{i=1}^{n} \left(\delta_{num}^{i} - \delta_{approx}^{i}\right)^2}_{SSE} + \underbrace{\sum_{i=1}^{n} \left(\delta_{approx}^{i} - \overline{\delta_{num}^{i}}\right)^2}_{SSR} \tag{5.11}$$

where n ($n = 9$ here) is the number of experiments. SST, SSE and SSR are the Sum

of Squares of all the experiments distances between the average and the values (Total), Sum of Squares of Errors and Sum of Squares of the Regression, respectively.

A small error induces a small SSE. SST and SSR values should thus be very much alike. This is tested by assessing the relative error of SSR compared to SST as:

$$R^2 = \frac{SSR}{SST} = 1 - \frac{SSE}{SST} \ , \ 0 \leq R^2 \leq 1 \tag{5.12}$$

where R^2 is the linear coefficient of regression. The closer to 1 is R^2, SSR will be closer to SST, which means that SSE is smaller and the fitting quality is higher.

In this problem, for each of the Ranges 1 and 2, $R^2 = 0.9994$ and 0.9716, respectively. SSE is thus smaller for the Range 1. This result is similar to the visual validation: selecting a range in which the experimental output is more linear improves significantly the approximating function accuracy.

5.2.4 Parameters sensitivity analysis

Equation 5.4 coefficients β_j^* and their relative proportions show how to manipulate this equation to perform inverse identifications:

First, if a coefficient is negligible compared to the others (*e.g.* less than 1%), its effect on δ_{approx} will be negligible when the parameter changes in the chosen range. Small coefficients will be neglected in the approximating function (here in Eq. 5.4) or the associated parameters values will be chosen, but shall have negligible effects on the identification.

Second, the variables coefficients in the approximating function (β_j^* in Eq. 5.4) represent the experimental output sensitivity to the variables and their binary interactions: the higher is the absolute value of the coefficient, the more sensitive is the approximated experimental response δ_{approx} to a change of this parameter.

Figures 5.5 and 5.6 compare the calculated coefficients of the variables and their interactions for the Ranges 1 and 2, respectively.

For the Range 1, the absolute values of $\beta_{F^*}^*$, $\beta_{F^*h^*}^*$ and $\beta_{F^*L^*}^*$ are respectively about 420%, 50% and 50% of the absolute value of $\beta_{h^*}^*$ or $\beta_{L^*}^*$. Experimentally change of F^* will thus significantly change δ_{approx} and affect the interaction of F^* with h^* and L^*: h^* and L^* can be identified by using F^* as experimental variable. If one of these interactions was infinitesimal, change of F^* would not affect properly the interaction between F^* and the corresponding variable. This would thus prevent proper identification of the variable.

This result could appear strange given that changing F^* in Eq. 5.1 provides no other information about L^3/h^3 ratio. It should yet be noted that the coefficients of Eq. 5.4 were identified on the numerical responses δ_{num}^i obtained from different values of h, F and L. Changing F in Eq. 5.4 affect h and L.

Analyzing the coefficients of Eq. 5.4 can thus guide the choice of experimental parameters to perform the identification.

By changing the chosen Range 1 to 2, the interactions coefficients and their proportions change. In the Range 2 (Fig. 5.6), changing F^* will also affect h^* and L^*, but the interaction between h^* and L^* becomes larger ($\beta_{h^*L^*}^*$ is about 21% and 55% of $\beta_{h^*}^*$ or $\beta_{L^*}^*$ for the Ranges 1 and 2, respectively). This means the interaction between h and L might also influence the identification.

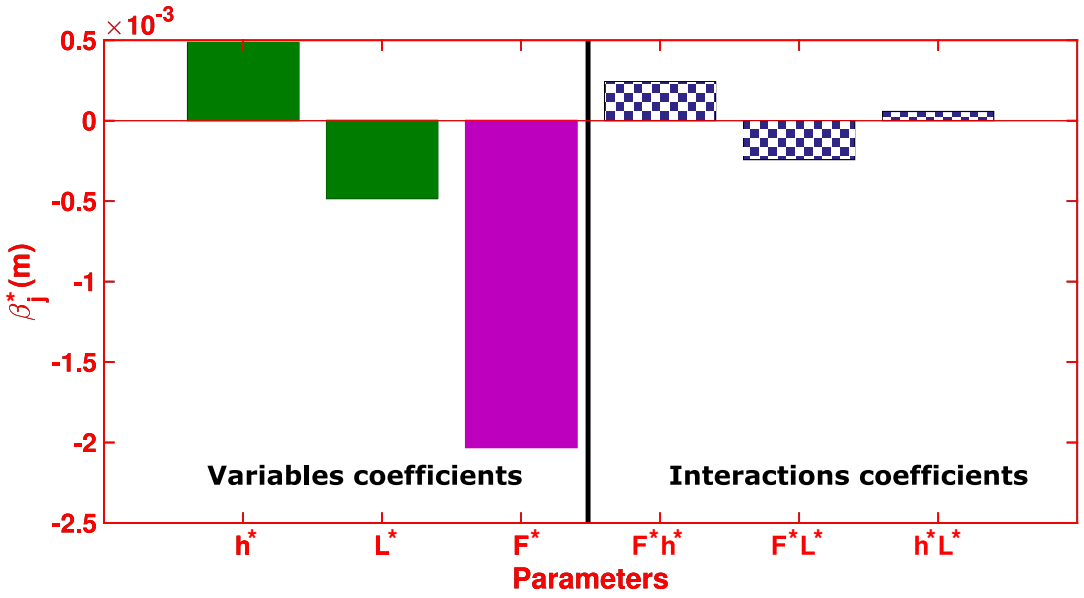

Figure 5.5: Factors of the variables and their interactions in Eq. 5.4 (β_j^*), calculated for Range 1: provide a parameters sensitivity analysis of the approximating function (δ_{approx}) to the variables and their interactions.

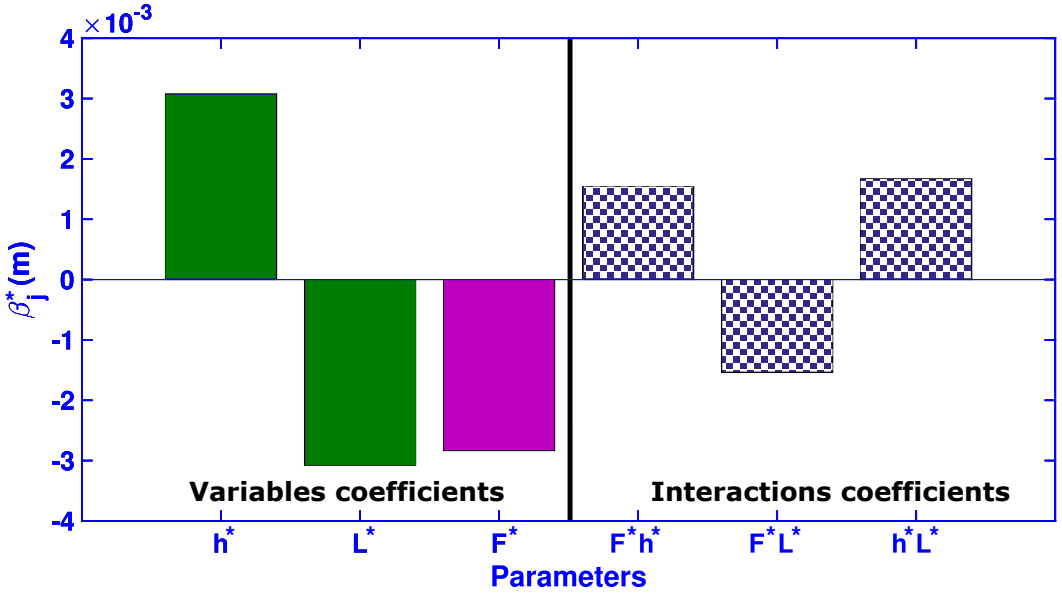

Figure 5.6: Factors of the variables and their interactions in Eq. 5.4 (β_j^*), calculated for Range 2: provide a parameters sensitivity analysis of the approximating function (δ_{approx}) to the variables and their interactions.

5.2.5 Inverse identification

Lets assume the function δ_{approx} was identified on the reference numerical results δ_{num}^i. The function δ_{approx} can now be used as a reduced model in the least mean square sense.

Performing K experiments on $beam_0$ using K different load F_k, as observed by analyzing the coefficients of Eq. 5.4, the unknown values h^* and L^* are sought so as to minimize the cost function:

$$CF_2 = \sum_{k=1}^{K} \left[\delta^k_{approx}(h^*, L^*, F^*_k) - \delta^{0k}_{exp}\right]^2 \tag{5.13}$$

where K is the number of experimental points, δ^k_{approx} is the approximating function at each experimental point and δ^{0k}_{exp} is the experimental output.

Since this beam problem has two unknowns, at least two experimental points must be used ($K = 2$). The "experimental"outputs δ^{0k}_{exp} were obtained using Eq. 5.1 with two experimental variables: $F_{k=1} = 5000N$ ($F^*_{k=1} = -1$) and $F_{k=2} = 15000N$ ($F^*_{k=2} = 1$). Inserting δ^{0k}_{exp} and F^*_k into Eq. 5.13, CF_2 is minimized when the following system of equations is satisfied:

$$\begin{aligned} \frac{\partial CF_2}{\partial h^*} &= 0 \\ \frac{\partial CF_2}{\partial L^*} &= 0 \end{aligned} \tag{5.14}$$

Using Eq. 5.3, h and L values were calculated from the normalized parameters h^* and L^*.

The inverse procedure was repeated for both Ranges 1 and 2. The identification results for the two ranges were compared with the reference values (Table 5.4). As it was expected from the visual and statistical validation results (section 5.2.3), the Range 1 identifications are about 3 times more accurate than the Range 2 identifications.

These results show that choosing a proper range for the domain of δ^i_{num}, in which the experimental output behavior is closer to the linear approximation, improves the accuracy of the inverse identification.

Table 5.4: Inverse identifications of the unknown parameters for Ranges 1 and 2 and their comparison with the theoretical results.

Parameters	Reference values	Range 1		Range 2	
		Inverse identification	Inverse identification error (%)	Inverse identification	Inverse identification error (%)
$h(m)$	0.128	0.124	3.1	0.116	9.4
$L(m)$	1.23	1.27	3.3	1.35	9.8

5.3 Applications

This section applies the presented DOE method in order to perform an inverse mechanical characterization of soft silicone samples. The method is used to characterize the silicone materials tested by the aspiration method as described in Chapters 3 and 4 (homogeneous and two-layer silicones). The real-time inverse identification results are compared to the reference materials characteristics obtained from the classical tests.

5.3.1 Homogeneous silicones

The FE simulations were performed with the method presented in Chapter 3. The aspiration experimental results collected on the homogeneous silicone samples were used for the inverse characterization.

Problem definition

The goal is to identify the mechanical properties of the silicone samples using the real-time inverse identification method (section 5.2) based on the aspiration tests results.

Apart the material properties, several parameters are impacting on the aspiration test results: the friction coefficient (μ) and the vertical load (Vl) between the aspiration probe and the target sample, the boundary conditions, the sample size, *etc.*. In the aspiration tests of the homogeneous samples, the boundary conditions and samples sizes were known. However, as presented in section 2.7, some questions remain about the effects of μ and Vl on the aspiration tests. To address these questions the effects of μ and Vl on the tests results are studied in this section.

A Gent model was used for FE simulation of the mechanical behavior of the silicone samples (section 3.3.1). The Gent constitutive parameters are E and J_m. The aspiration test output should thus be estimated as a function of E, J_m, μ and Vl. This function should be fitted to the FE simulation outputs.

Approximating function

In this problem the three types of parameters are:

- **Type 1:** Known and stable parameters during the experiments: the cylindrical silicone sample diameter ϕ and height L and the aspiration aperture diameter AD (Chapter 3).
- **Type 2:** Unknown parameters: the material parameters E and J_m, the friction coefficient μ and the vertical load Vl.
- **Type 3:** Experimental set of parameters: pressure-volume curves $(P_i, V_i)_k$.

Following the example in Frauziols et al., 2016 and since the pressure-volume curves of the aspiration tests on the homogeneous samples are almost linear, it was assumed to replace the experimental curves $(P_i, V_i)_k$ by their slopes $S^k_{H(exp)}$.

Table 5.5 gives the chosen ranges for the unknown parameters. These parameters were normalized from -1 to 1 in their respected ranges.

Table 5.5: The variables ranges for the homogeneous silicones.

Parameters	Minimum	Center	Maximum
$E(kPa)$	10	25	40
J_m	8	10	12
μ	0	0.5	1
$Vl(N)$	0	1	2

The approximating function can thus be defined as:

$$\begin{aligned} S_{H(approx)} =& \beta_0^* + \beta_{E^*}^* E^* + \beta_{J_m^*}^* J_m^* + \beta_{\mu^*}^* \mu^* + \beta_{Vl^*}^* Vl^* + \\ & \beta_{E^* J_m^*}^* E^* J_m^* + \beta_{E^* \mu^*}^* E^* \mu^* + \beta_{E^* Vl^*}^* E^* Vl^* + \\ & \beta_{J_m^* \mu^*}^* J_m^* \mu^* + \beta_{J_m^* Vl^*}^* J_m^* Vl^* + \beta_{\mu^* Vl^*}^* \mu^* Vl^* \end{aligned} \tag{5.15}$$

Using Eq. 5.5 and knowing that $m = 4$ in this problem, it can be shown that 17 FE simulations should be performed to identify the constants β_j^*. The coefficients β_j^* are defined in the least square sense to minimize the cost function:

$$CF_{H1} = \sum_{i=1}^{17} (S_{H(approx_i)} - S_{H(FE_i)})^2 \tag{5.16}$$

Minimizing the cost function according to the coefficients β_j^*, is written as a set of 11 equations:

$$\frac{\partial CF_{H1}}{\partial \beta_j^*} = 0, \forall j \in [0, E^*, J_m^*, \mu^*, Vl^*, E^* J_m^*, E^* \mu^*, E^* Vl^*, J_m^* \mu^*, J_m^* Vl^*, \mu^* Vl^*] \tag{5.17}$$

Solving this system of equations, the coefficients β_j^* of Eq. 5.15 can thus be identified.

Validation criteria

To visually assess the quality of the approximating function $S_{H(approx)}$, its curves versus each unknown variable (E, J_m, μ and Vl) should be compared with the corresponding FE simulations responses $S_{H(FE)}$. The curves were plotted versus each variable in its range, while the three other variables were constant and at the centers of their respected ranges (Fig. 5.7). The two curves overlap perfectly for all the variables. This provides a first overview of the fitting quality.

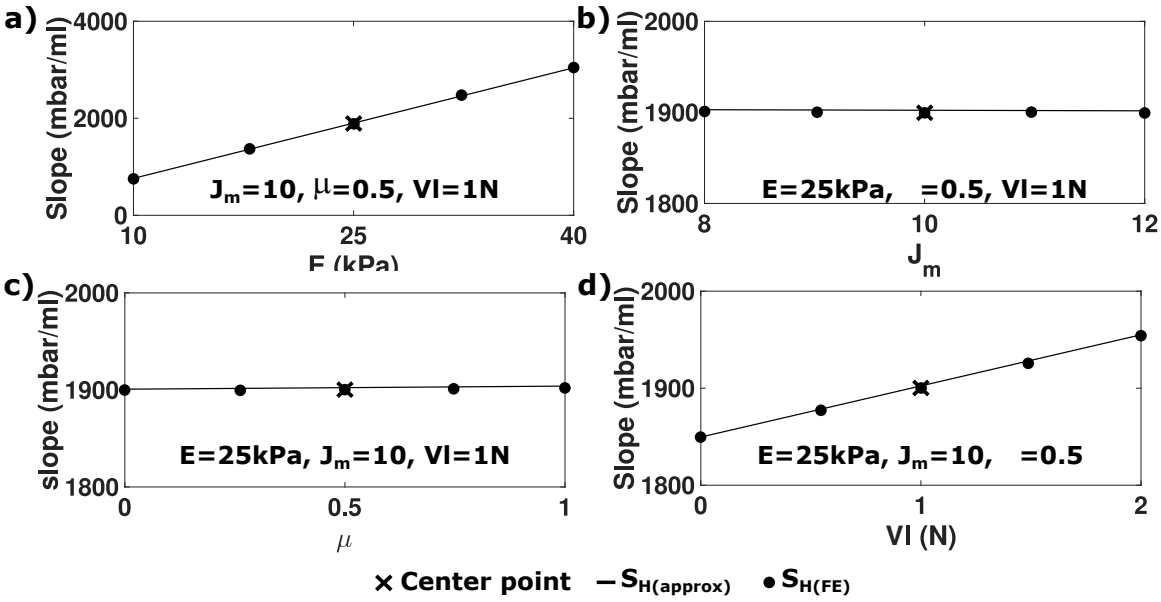

Figure 5.7: $S_{H(FE)}$ versus the unknown parameters curves: while a) E, b) J_m, c) μ and d) Vl change in their selected domains and the other parameters are constant at the centers of their domains.

In order to use the ANOVA method for the statistical assessment of the fitting quality, the parameters SST, SSE and SSR can be defined as:

$$\underbrace{\sum_{i=1}^{n}\left(S_{H(FE_i)}-\overline{S_{H(FE_i)}}\right)^2}_{SST}=\underbrace{\sum_{i=1}^{n}\left(S_{H(FE_i)}-S_{H(approx_i)}\right)^2}_{SSE}+\underbrace{\sum_{i=1}^{n}\left(S_{H(approx_i)}-\overline{S_{H(FE_i)}}\right)^2}_{SSR} \tag{5.18}$$

where $n = 17$ is the number of FE simulations.

Using the obtained parameters from Eq. 5.18, the linear coefficient of regression R^2 for this problem was calculated to be 0.9999. This result concurs with the visual validation in Fig. 5.7 and indicates a very good agreement of the approximating function (estimated by Eq. 5.15) with the FE simulations.

Parameters sensitivity analysis

The variables coefficients and their interactions in Eq. 5.15 (β_j^*) are compared in Fig. 5.8. These coefficients represent the sensitivity of the FE simulation response to the variables and their interactions.

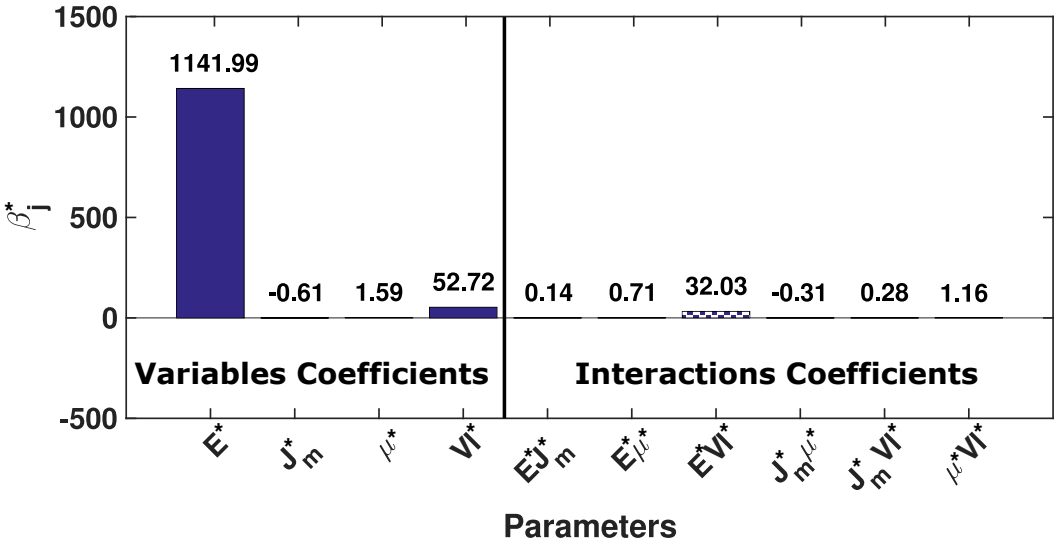

Figure 5.8: Factors of the unknown parameters and their interactions in Eq. 5.15 (β_j^*): this provides a parameter sensitivity analysis of the FE simulation response ($S_{H(FE)}$) to the parameters and their interaction.

Among the studied parameters, the sensitivity is significantly higher for the material Young's modulus E: this result confirms that the proposed contribution of the experimental and numerical approaches allows to identify the Young's modulus E of the silicone materials.

The sensitivity to the friction coefficient μ is about 0.1% of the sensitivity to E, which means that it has only a minor impact on the results of the aspiration tests. The sensitivity to the vertical load Vl is less than 5% of the sensitivity to E. This shows the large influence of Vl on the deformation history of the aspirated tissue in comparison to μ.

The vertical load Vl should be minimized during the experiments. Using the holder proposed in Chapter 4 can thus reduce the chance of application of any unknown external load to the aspiration probe. The sensitivity of the FE simulations of the aspiration tests to the friction coefficient and to the vertical load between the aspiration probe and the target tissue were previously studied [Hollenstein et al., 2009 and Badir, Bajka, and Mazza, 2013]. These studies revealed similar results as the present study.

In addition the sensitivity to the material parameter J_m is about 0.05% of the sensitivity to E. The sensitivity to the parameters binary interactions are also lower than 3% of the sensitivity to E. These results indicate that E is the only parameter which has a major effect on the approximating function. Therefore, the other parameters can be replaced by a preset values in the approximating function (Eq. 5.15). The preset values for μ and Vl are chosen to be zero and for J_m it is approximated to be 10 ($\mu^* = -1, Vl^* = -1$ and $J_m^* = 0$). The reduced approximating function $S_{H(approx)}^{reduced}$ can thus be written as:

$$S_{H(approx)}^{reduced} = \beta_0^* - \beta_{\mu^*}^* - \beta_{Vl^*}^* + \beta_{\mu^* Vl^*}^* + (\beta_{E^*}^* - \beta_{E^*\mu^*}^* - \beta_{E^*Vl^*}^*)E^* \tag{5.19}$$

Real-time inverse identification

For real-time inverse identification of the unknown parameters, a cost function was defined to estimate the mismatch between the reduced approximating function $S_{H(approx)}^{reduced}$ (Eq. 5.19) and the experimental output $S_{H(exp)}^{k}$ as:

$$CF_{H2} = \sum_{k=1}^{K} \left[S_{H(approx)}^{reduced}(E^*) - S_{H(exp)}^{k} \right]^2 \tag{5.20}$$

Since this problem has just one unknown, one experimental output $S_{H(exp)}^{k}$ is enough to identify the unknown parameter E^* ($K = 1$).

To calculate $S_{H(exp)}^{k}$ in Eq. 5.20, the experimental pressure-volume curves (Fig. 3.8), obtained from aspiration tests, were used. Minimizing the cost function CF_{H2} for the parameter E^* of each tested silicone, this parameter was identified for the Silicones #1 and #2. The material parameter E was obtained using Eq. 5.3 and is reported for each of the silicones in Table 5.6.

Table 5.6: Parameter E of the Gent model for the silicone materials of Chapter 3 obtained from reference measurements and real-time inverse identifications. The real-time inverse errors are compared with the previous inverse identifications errors from Chapter 3.

Material	Material constant	Reference measurement from Chapter 3	Real-time inverse identification	Real-time inverse error (%)	FE inverse error (%) from Chapter 3
Silicone#1	$E(kPa)$	16.82	18.5	10.2	8.8
Silicone#2	$E(kPa)$	24.87	26.90	8.2	6.6

Table 5.6 compares the identified parameters for the Silicones#1 and #2 using the real-time inverse identifications and the reference measurements performed in Chapter 3. The identifications errors were calculated according to the reference measurements. The real-time inverse identifications have about 10 and 8% errors for the identified Young's

moduli E of Silicones#1 and #2, respectively. These errors from the previous FE inverse identifications presented in Chapter 3 were about 8 and 6%, respectively. Although the real-time inverse identification method increases the errors about 2%, it decreases the computation time from about one hour (for the previous FE inverse identifications) to a few seconds. Therefore, using the real-time identification makes the characterization method more compatible with any intra-operative procedure, in which the measurement duration is a key issue.

5.3.2 Two-layer silicones

This section presents the application of the presented DOE method for real-time inverse identification of the superficial layer thickness and material properties of two-layer silicone samples. The experimental results are obtained from the aspiration tests that were performed in Chapter 4. The FE modeling presented in section 4.2.7 is used for the simulations.

Problem definition

The problem consists in a cylindrical bulk silicone sample with a superficial layer made of a stiffer silicone. The Gent material model constants of the superficial layer (E_1 and J_{m1}) and of the bulk silicone (E_2 and J_{m2}) and the superficial layer thickness (L_1) are the unknown parameters in this problem. The goal is to obtain the unknown parameters using the real-time inverse procedure based on the experimental aspiration tests with different aperture diameters (AD_k).

As it was mentioned in section 5.3.1 the friction coefficient and vertical load had infinitesimal effects on the simulations responses in comparison with the material Young's modulus. In addition, using a holder to perform the aspiration tests reduced the vertical load and consequently the friction coefficient effect on the tests results. These two parameters (μ and Vl) are thus set to zero for the FE simulations in this section.

The linear behavior of the pressure-normalized volume curves of the tests on the two-layer samples (Figs. 4.11 and 4.12) shows that the curves slopes ($S^k_{TL(exp)}$) can be used as the experimental outputs, as proposed in Frauziols et al., 2016. The FE simulations response can thus be noted as $S_{TL(FE)}$.

Approximating function

The three types of parameters in this problem are:

- **Type 1:** Known and stable parameters during the experiments: the bulk silicone height L_2, the superficial layer diameter ϕ, which is the same as the bulk silicone diameter.

- **Type 2:** Unknown parameters: the superficial layer material parameters E_1 and J_{m1}, the bulk silicone material parameters E_2 and J_{m2} and the superficial layer thickness L_1.

- **Type 3:** Experimental set of variables: $[AD_k, S^k_{TL(exp)}]$.

The experimental output $S_{TL(exp)}$ is thus approximated as a linear polynomial function of type 2 and type 3 parameters.

The inverse identifications were performed using the aspiration tests with different aperture diameters AD_k. their effects were taken into account using the variable $r = L_1/AD$ representing the scale of AD compared to the superficial layer thickness L_1.

The chosen ranges for the variables are given in Table 5.7. The variables were then normalized from -1 to 1 in their respected ranges.

Table 5.7: The variables ranges for the two-layer silicones.

Parameters	Minimum	Center	Maximum
$E_1(kPa)$	40	55	70
$E_2(kPa)$	5	15	25
J_{m1}	8	10	12
J_{m2}	8	10	12
$r = L_1/AD$	0.1	0.8	1.5

The approximating function was thus defined as:

$$\begin{aligned} S_{TL(approx)} =& \beta_0^* + \beta_{E_1^*}^* E_1^* + \beta_{E_2^*}^* E_2^* + \beta_{J_{m1}^*}^* J_{m1}^* + \beta_{J_{m2}^*}^* J_{m2}^* + \beta_{r^*}^* r^* + \\ & \beta_{E_1^* E_2^*}^* E_1^* E_2^* + \beta_{E_1^* J_{m1}^*}^* E_1^* J_{m1}^* + \beta_{E_1^* J_{m2}^*}^* E_1^* J_{m2}^* + \beta_{E_1^* r^*}^* E_1^* r^* + \\ & \beta_{E_2^* J_{m1}^*}^* E_2^* J_{m1}^* + \beta_{E_2^* J_{m2}^*}^* E_2^* J_{m2}^* + \beta_{E_2^* r^*}^* E_2^* r^* + \beta_{J_{m1}^* J_{m2}^*}^* J_{m1}^* J_{m2}^* + \\ & \beta_{J_{m1}^* r^*}^* J_{m1}^* r^* + \beta_{J_{m2}^* r^*}^* J_{m2}^* r^* \end{aligned} \tag{5.21}$$

Inserting $m = 5$ into Eq. 5.5 showed that 33 FE simulations should be performed to identify the constants β_j^* of Eq. 5.21. At each simulation point, the approximating function estimates the slope response $S_{TL(FE_i)}$. To identify the coefficients β_j^*, the following cost function was defined in the least square sense:

$$CF_{TL1} = \sum_{i=1}^{33} (S_{TL(approx_i)} - S_{TL(FE_i)})^2 \tag{5.22}$$

Minimizing the cost function, given by Eq. 5.22, according to the coefficients β_j^*, gives at set of 16 equations:

$$\begin{aligned} & \frac{\partial CF_{TL1}}{\partial \beta_j^*} = 0, \forall j \in [0, E_1^*, J_{m1}^*, E_2^*, J_{m2}^*, r^*, ... \\ & E_1^* J_{m1}^*, E_1^* E_2^*, E_1^* J_{m2}^*, E_1^* r^*, E_2^* J_{m1}^*, E_2^* J_{m2}^*, E_2^* r^*, J_{m1}^* J_{m2}^*, J_{m1}^* r^*, J_{m2}^* r^*] \end{aligned} \tag{5.23}$$

Solving this system of equations, the coefficients β_j^* of Eq. 5.21 are identified.

Validation criteria

The visual assessment of the approximating function is shown in Fig. 5.9: $S_{TL(approx)}$ curves versus each of the studied variables (E_1, E_2, J_{m1}, J_{m2} and r) are compared with the FE simulations $S_{TL(FE)}$ curves. The curves were plotted versus each variable in its range, while the other variables were constant and at the centers of their respected

ranges. Adequate agreement can be observed between $S_{TL(approx)}$ and $S_{TL(FE)}$ curves for all the parameters.

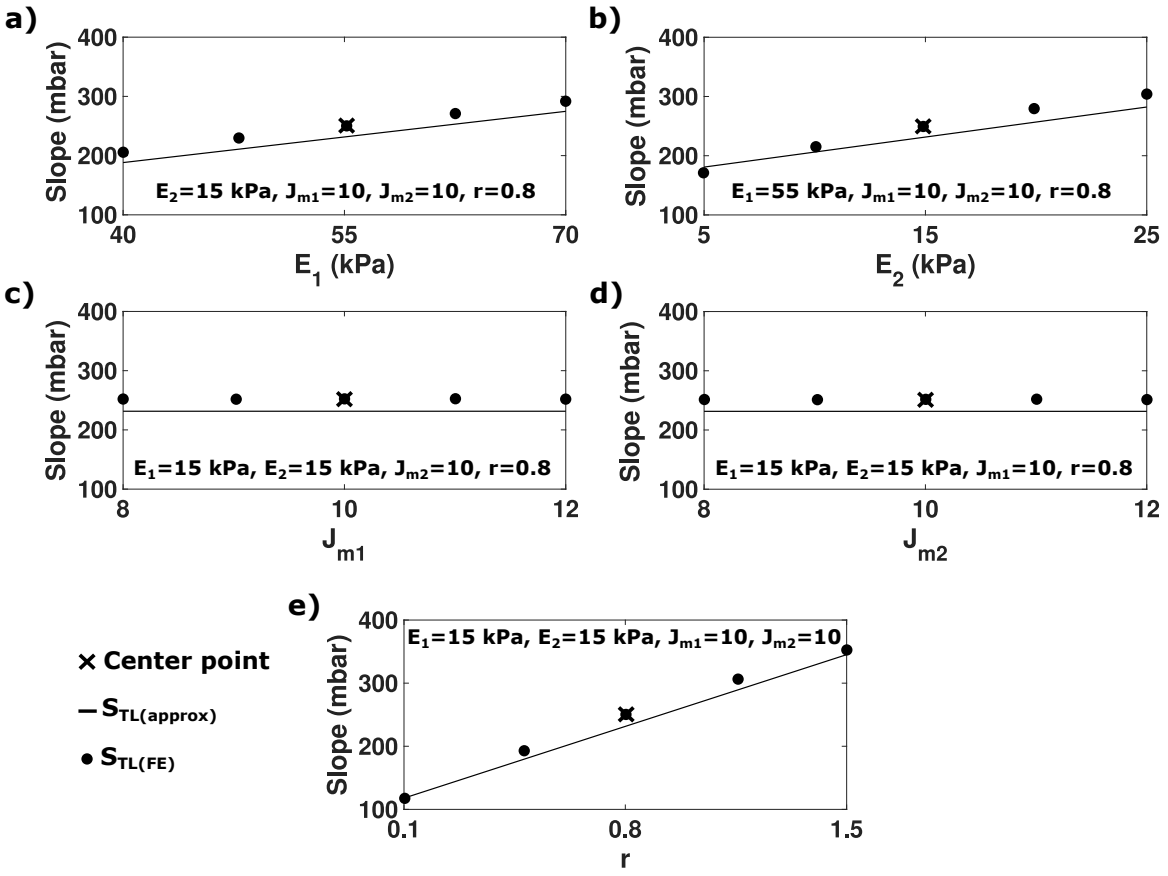

Figure 5.9: $S_{TL(FE)}$ versus the unknown parameters curves: while a) E_1, b) E_2, c) J_{m1}, d) J_{m2} and e) r change in their selected domains and the other parameters are constant at the centers of their domains.

To assess the fitting quality of the approximating function using ANOVA method, the parameters SST, SSE and SSR were defined as:

$$\underbrace{\sum_{i=1}^{n}\left(S_{TL(FE_i)}-\overline{S_{TL(FE_i)}}\right)^2}_{SST}=\underbrace{\sum_{i=1}^{n}\left(S_{TL(FE_i)}-S_{TL(approx_i)}\right)^2}_{SSE}+\underbrace{\sum_{i=1}^{n}\left(S_{TL(approx_i)}-\overline{S_{TL(FE_i)}}\right)^2}_{SSR} \tag{5.24}$$

where the number of FE simulations is $n = 33$.

Inserting the obtained parameters from Eq. 5.24 into Eq. 5.12, the linear coefficient of regression R^2 for this problem was calculated to be 0.9981. The results of the visual validation (Fig. 5.9) and the ANOVA method indicate acceptable agreement of the approximating function (Eq. 5.21) with the FE simulations.

Parameters sensitivity analysis

Figure 5.10 compares the coefficients of the variables and their interactions in the Eq. 5.21. As previously mentioned, these coefficients of the approximating function show the FE

simulations responses sensitivity to each variable and its interactions with the other variables.

The sensitivities are considerably higher for the variables E_1, E_2 and r (more than 8500 times larger than the sensitivity to the parameters J_{m1} and J_{m2}). As a result, the proposed contribution of experimental and numerical approaches allows to identify the superficial layer thickness L_1 and the two materials' Young's moduli E_1 and E_2.

The sensitivity to the variables interactions $E_1 r$ and $E_2 r$ are significant, which means that the identification quality of the parameters E_1, E_2 and r are linked.

The infinitesimal sensitivity to the parameters J_{m1} and J_{m2} and their binary interaction with the other parameters show that these parameters can be replaced by preset values in the approximation function (Eq. 5.21). Choosing the preset values to be $J_{m1} = 10$ and $J_{m2} = 10$ ($J^*_{m1} = 0$ and $J^*_{m2} = 0$), the reduced approximating function $S^{reduced}_{TL(approx)}$ can be written as:

$$\begin{aligned} S^{reduced}_{TL(approx)} =& \beta^*_0 + \beta^*_{E^*_1} E^*_1 + \beta^*_{E^*_2} E^*_2 + \beta^*_{r^*} r^* + \\ & \beta^*_{E^*_1 E^*_2} E^*_1 E^*_2 + \beta^*_{E^*_1 r^*} E^*_1 r^* + \beta^*_{E^*_2 r^*} E^*_2 r^* \end{aligned} \tag{5.25}$$

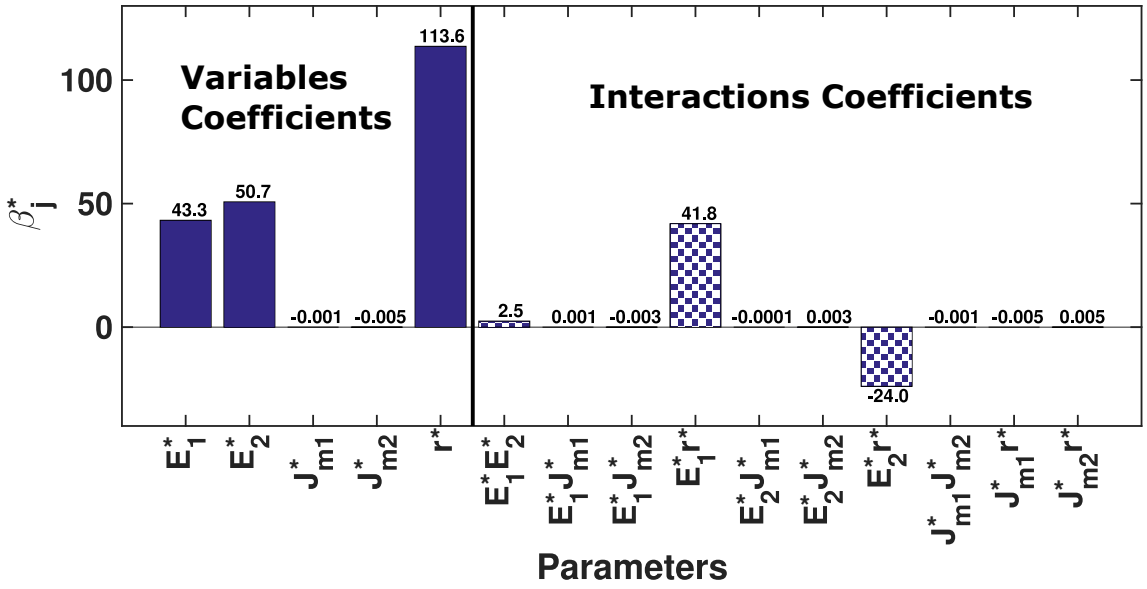

Figure 5.10: Factors of the unknown parameters and their interactions in Eq. 5.21 (β^*_j): this provides a parameter sensitivity analysis of the FE simulation response ($S_{TL(FE)}$) to the parameters and their interactions.

The parameters E_1, E_2 and r must be identified. This requires to use at least three different experiments. Since $r = L_1/AD$, performing the experiments with at least three different AD is required.

Real-time inverse identification

To estimate the mismatch between the approximating function $S^{reduced(k)}_{TL(approx)}$ (Eq. 5.25) and the experimental response $S^{k}_{TL(exp)}$, a cost function was defined in the least square sense:

$$CF_{TL2} = \sum_{k=1}^{K} \left[S^{reduced(k)}_{TL(approx)}(E_1^*, E_2^*, r_k^*) - S^{k}_{TL(exp)} \right]^2 \tag{5.26}$$

As mentioned during the parameters sensitivity analysis, three experimental measurements with three different AD on each sample are required to perform the inverse identifications. In Eq. 5.26, K was thus set to 3 and r_k^* was defined as (see Eq. 5.3):

$$r_k^* = \frac{2(\frac{L_1}{AD_k}) - (r_{max} + r_{min})}{r_{max} - r_{min}} \tag{5.27}$$

where AD_k is the aspiration aperture diameter in each of the three experiments.

The real-time inverse identification was enabled by minimizing the cost function CF_{TL2}, given by Eq. 5.26 according to the unknown variables (E_1^*, E_2^* and L_1). The material parameters (E_1 and E_2) were then calculated using Eq. 5.3.

Table 5.8: Comparison of the identified parameters using the reference measurements and the real-time inverse identifications for the two-layer samples of Chapter 4. The real-time inverse errors are compared with the previous inverse identifications errors from Chapter 4.

Samples	Parameters	Reference measurements from Chapter 4	Real-time inverse identification	Real-time inverse error (%)	FE inverse error (%) from Chapter 4
Sample A	$L_1(mm)$	3.02±0.03	3.16	[3.6, 5.7]	[2.6, 4.5]
	$E_1(kPa)$	54.21	51.50	5.0	2.3
	$E_2(kPa)$	16.82	14.77	12.2	8.6
Sample B	$L_1(mm)$	6.08±0.09	5.98	[0.1, 3.1]	[1.0, 2.0]
	$E_1(kPa)$	54.21	59.11	9.0	6.8
	$E_2(kPa)$	16.82	15.12	10.1	7.2

The identified parameters for each of the Samples A and B, tested in Chapter 4, are reported in Table 5.8. The real-time inverse identifications errors were calculated according to the reference measurements performed in Chapter 4. These errors were compared with the errors of the previous FE inverse identifications from Chapter 4. The maximum errors of the identified superficial layer thickness and materials' Young's moduli using the real-time inverse identification are about 5 and 12%, respectively. These errors are about 4 and 8% for the previous FE inverse identifications. However, the real-time inverse identifications reduce the computation time from around two hours (for the previous FE inverse identification method) to a few seconds. Therefore, although this method increases the characterization errors, it is more compatible with the intra-operative characterization of a two-layer soft tissue.

5.4 Conclusion

Real-time data processing is required for intra-operative measurements of soft tissues mechanical behavior. To address this question, a real-time inverse identification method for the mechanical characterization of soft tissues using the volume-based aspiration tests results was introduced.

First the used method was described on a simple mechanical problem. The presented method was then applied to the aspiration experimental results of the homogeneous and two-layer samples tested in Chapters 3 and 4, respectively. The real-time identification errors in comparison with the reference measurements were calculated: the Young's moduli were identified with 8% and 12% maximum errors for the homogeneous and two-layer samples, respectively. Moreover, the superficial layer thicknesses of the two-layer samples were identified with a maximum error of 5%.

The obtained errors from the real-time inverse identification were compared with the previous FE inverse identifications (performed in Chapters 3 and 4): using the new method was still acceptable with an error of about 12% at its maximum level. However, the computation time decreased from more than one hour in the previous identifications to a few seconds in the real-time inverse identification. The presented method seems thus compatible with the clinical constraints.

A parameter sensitivity analysis was conducted using the numerical approximating functions estimated for the inverse identifications. The FE simulations are highly sensitive to the material Young's modulus for the homogeneous samples and to the materials Young's moduli and superficial layer thickness for the two-layer samples. This validates that the proposed real-time inverse identification method enables identification of these parameters. The analyses show lower sensitivity to unknown parameters like the friction coefficient μ and the vertical load Vl in comparison with the desired material parameters like the material Young's modulus E. As it was proposed in Chapter 4, the use of an aspiration probe holder with an ultrasound gel will avoid increasing the effect of the parameters μ and Vl on the experimental results.

GENERAL CONCLUSION AND PERSPECTIVES

Conclusions

This thesis has addressed the *in-vivo* and *in-situ* mechanical characterization of soft living tissues. An original aspiration method based on the measurement of the aspirated tissue volume was proposed to overcome some constraints of the previous aspiration devices (based on optical measurements) regarding the complex designs and the sterilization constraints. Using the volume-based method all the electronic parts were removed from the aspiration probe. The system head was thus reduced to a simple tube: the sterilization becomes easy and the head is disposable after use. The simple design of the new device enables the user to choose the aspiration aperture diameter and shape according to the test needs.

In a first step, the volume measurement accuracy of our new method was compared with the classic optical method: the same or even better relative accuracy was obtained for this volume-based method. The effects of the aspiration aperture and syringe diameters on volume measurement accuracy were also evaluated. The results showed that the accuracy is almost independent of the aperture diameter while decreasing the syringe diameter provides a better accuracy.

Then, our volume-based aspiration method was evaluated on silicone materials. Samples from two soft silicones with different stiffnesses were made and tested during three experimental configurations: 1) our aspiration test, 2) uniaxial tensile test and 3) equibiaxial tensile test obtained at the top of a bulge test. The results of the aspiration tests were used in an inverse FE-based procedure in order to identify the materials parameters. The reference material parameters were characterized using the tensile and bulge tests results. Comparison of the inverse identifications with the reference parameters resulted in a relative error of about 7% for the identified Young's moduli. The errors are about 4 times lower than our previous studies based on optical aspiration measurements. Additionally, the measured pressure ratio of the aspiration tests for the two materials is similar to the stress ratios obtained with standard characterization tests. A relative discrimination between different parts of the structure is thus easy and relative mechanical behavior mapping of soft tissues (organ or skin) is possible without requiring an inverse procedure.

In the next step, a new method was introduced to identify the superficial layer thickness and the mechanical properties of multi-layered soft tissues using our aspiration measurements with different aperture diameters. The method was validated on two-layer synthetic samples made from two silicones with different stiffnesses. The superficial

layer thickness and materials' parameters were identified using an FE updating inverse method. To assess the identification quality, the silicone samples were tested using classical uniaxial and equibiaxial extension tests, as references. The results gave maximum identification errors of 3% and 8% for the superficial layer thickness and the mechanical parameters, respectively.

Finally, a method was proposed for the real-time inverse identification of soft tissues based on the aspiration measurements, which is a prerequisite for any intra-operative application. The method was applied to the aspiration test results of the homogeneous and the two-layer silicones investigated in the previous steps. The real-time identification errors in comparison with the reference measurements were also calculated: using the real-time inverse identification method increased the errors about 4% at its maximum level. However, the computation time decreased from more than one hour in the previous identifications to a few seconds in the "real-time"inverse identification. This means that the proposed inverse method is compatible with the intra-operative clinical constraints.

We should however be conscious of the limitations of our work. In particular, as any aspiration device, our volume based aspiration method and its associated inverse identification only provide a local estimation of tissue stiffness. Many works have shown the complexities of the mechanical behavior of biological soft tissues such as human skin [Flynn, Taberner, and Nielsen, 2011a,c; Jor et al., 2013]. It is clear that such complexity is not taken into account here since properties like time-dependent behavior or anisotropy are not captured with the aspiration device.

Moreover, when investigating in vivo tissues, the presence of internal residual stress as well as some non-controlled boundary conditions may bias the stiffness estimated from the aspiration experiment with a reference state of the tissue that is not well defined. Localizing the zero both in strain and stress for such a living tissue is an arduous problem which was out of the scope of this Ph.D. work.

Eventually, it is important to note that choosing a material constitutive law to properly model the soft tissue behavior is of great importance and can unfortunately not be fully determined with a single aspiration test. Such a test will have to be combined with other testing in various kinematic configurations so that a suitable strain energy formulation and the corresponding parameters can be chosen.

Perspectives

The comparison of the silicone mechanical parameters identification error with our previous works indicates a significant accuracy improvement (about 4 times lower identification error). Moreover, to the best of our knowledge, it is the first time that an aspiration method is used to identify the superficial layer thickness along with the mechanical properties of multi-layered tissues.

The next step of this work will address the *ex-vivo* validation of the method on real biological tissues. It is hoped that these results will open the door to extensive *in-vivo* measurements on various regions of the human skin, assuming in a first step a two-layer structure of human skin (mainly represented by dermal and sub-dermal tissues). This could provide subject-specific values for constitutive parameters of these two layers as well as for the thickness of the dermal tissues. The biomechanical models of the face, buttock or breast tissues developed in our group should therefore directly benefit from

such measurements [Bucki, Nazari, and Payan, 2010; Luboz et al., 2018; Mîra et al., 2018].

For future works, using aspiration probes with inhomogeneous aperture shapes (like elliptical) may give more information about the tissue inhomogeneity in its surface. In addition, the time-dependent properties of tissue (like viscoelasticity or poroelasticity) can be measured by applying time-dependent aspiration to the tissue, as it was previously performed using the optical aspiration devices [Hollenstein et al., 2013; Kauer, 2001; Nava et al., 2008].

APPENDIX

A

CONSTITUTIVE MODELING BASICS OF BIOLOGICAL SOFT TISSUES

Contents

Continuum-based constitutive relations describe the general behavior of the internal constitution of biological soft tissues [Gasser, Ogden, and Holzapfel, 2006]. Constitutive relations are of fundamental importance for the numerical simulation of deformations inside the tissues. Most of the efforts for constitutive modeling of the soft tissues consisted in assuming a law from the collected experimental data [Sun and Sacks, 2005].

The derived constitutive laws proposed in the literature try to approximate different mechanical behaviors such as: hyperelasticity, viscoelasticity, anisotropy, stress-softening

and residual strain [Maher et al., 2012]. The soft tissues are usually considered as incompressible materials in the constitutive laws since they are mainly composed of water [Carew, Vaishnav, and Patel, 1968; Payan and Ohayon, 2017].

The basics of continuum mechanics and a short literature review about modeling of hyperelasticity in soft tissues are briefly presented in the following sections.

A.1 Continuum mechanics basics

Let Ω_0 and Ω be considered as the initial and deformed configurations of a continuous volume, respectively. According to Fig. A.1, $\mathbf{X}$ and $\mathbf{x}$ are the position vectors of a point Z_0 in the initial and Z in the deformed configurations, respectively. The initial and deformed configurations are connected through a displacement vector $\mathbf{u}(\mathbf{X})$. Mapping an infinitesimal vector $d\mathbf{X}$ in the initial configuration (at point Z_0) to an infinitesimal vector $d\mathbf{x}$ in the deformed configuration (at point Z) leads to the definition of a deformation gradient:

$$\mathbf{F} = \frac{d\mathbf{x}}{d\mathbf{X}} \tag{A.1}$$

The stretch can be defined as the ratio of the deformed vector $d\mathbf{x}$ length to the initial vector $d\mathbf{X}$ length:

$$l = \frac{|d\mathbf{x}|}{|d\mathbf{X}|} \tag{A.2}$$

The right and left Cauchy-Green deformation tensors can respectively be defined as:

$$\mathbf{C} = \mathbf{F}^T\mathbf{F} \tag{A.3}$$

and

$$\mathbf{B} = \mathbf{F}\mathbf{F}^T \tag{A.4}$$

More details can be found in [Ogden, 1997].

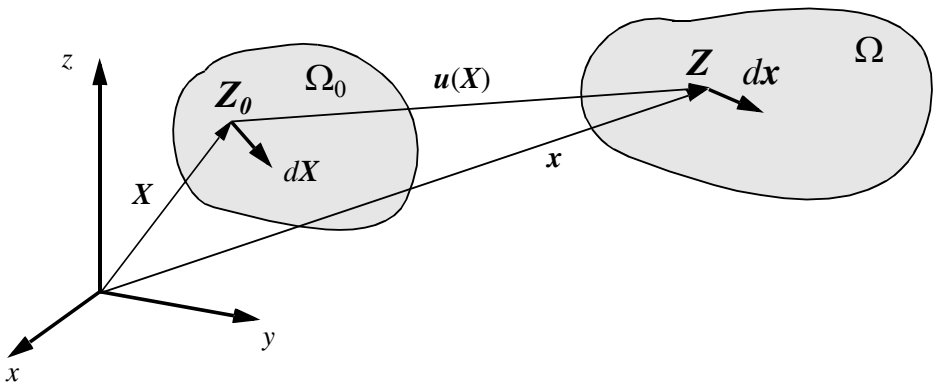

Figure A.1: Initial configuration (Ω_0) and deformed configuration (Ω) [Kauer, 2001].

The engineering strain for small deformations is described as the ratio of the change in the deformed vector length to the corresponding initial vector length:

$$\boldsymbol{\epsilon} = \frac{d\mathbf{x} - d\mathbf{X}}{d\mathbf{X}} \tag{A.5}$$

For large deformations, which is the case for most biological soft tissues, the strain defined by Eq. A.5 is no more applicable. For such large deformations, a measure of strain can be any monotonically increasing function related to stretch in a one-to-one manner, this function has to vanish in the reference configuration. For example, the Green-Lagrangian strain tensor is commonly used for large deformations:

$$\mathbf{E} = \frac{1}{2}(\mathbf{C} - \mathbf{I}) \tag{A.6}$$

where $\mathbf{C}$ is described with Eq. A.3 and $\boldsymbol{I}$ is the identity tensor.

The stress response of the material due to the applied boundary conditions can be defined in three ways:

1. The second Piola-Kirchoff stress tensor $\mathbf{S}$ using the initial configuration.
2. The Cauchy stress tensor $\boldsymbol{\sigma}$ using the deformed configuration.
3. The first Piola-Kirchoff stress tensor $\mathbf{\Pi}$ using an intermediate state.

Details about the stresses definitions and conservation equations can be found in continuum mechanics handbooks such as [Liu, 2002].

A.2 Hyperelasticity

A hyperelastic material is an elastic material for which the work is independent of the deformation path. This corresponds to the absence of energy dissipation inside the material during the deformation. A hyperelastic material is therefore defined by a stressstrain relationship that derives from a strain energy density function W. The stress, such as the second Piola-Kirchoff stress tensor $\mathbf{S}$, can be written as a function of the potential strain energy W:

$$\mathbf{S} = \frac{\partial W(\mathbf{E})}{\partial \mathbf{E}} = 2\frac{\partial \psi(\mathbf{C})}{\partial \mathbf{C}} \tag{A.7}$$

The hyperelastic models are suitable for elastic materials that can be subjected to large deformations and present non-linear stress responses.

For hyperelastic isotropic materials, W can be expressed as a function of the three invariants of the deformation tensor $\mathbf{C}$ [Kauer, 2001]:

$$W = W\left(I_1, I_2, I_3\right) \tag{A.8}$$

where I_1, I_2 and I_3 are:

$$I_1 = tr\mathbf{C} \tag{A.9}$$

$$I_2 = \frac{1}{2}\left[(tr\mathbf{C})^2 - tr\mathbf{C}^2\right] \tag{A.10}$$

$$I_3 = det\mathbf{C} \tag{A.11}$$

For incompressible materials, $I_3 = 1$.

There are several strain energy functions that are proposed for different hyperelastic behaviors of materials. Among these functions the Mooney-Rivlin strain energy is quite popular [Mooney, 1940]:

$$W_{M-R} = C_1(I_1 - 3) + C_2(I_2 - 3) + \frac{K}{2}(J-1)^2 \tag{A.12}$$

where C_1 and C_2 are material constants, K is the initial bulk modulus (dealing with compressibility) and $J = det(\mathbf{F})$. The Mooney-Rivlin model has usually been used for rubber materials [Huanh, Xie, and Liu, 2008; Mullins and Tobin, 1965].

The Neo-Hookean model [Treloar, 1943a,b], resulted from Eq. A.12 by neglecting the function dependency on the second deformation tensor invariant, has also been used widely:

$$W_{Neo} = C_1(I_1 - 3) + \frac{K}{2}(J-1)^2 \tag{A.13}$$

In this Ph.D. work, another model introduced by Gent, 1996 was implemented to model the silicone materials:

$$W_G = -\frac{EJ_m}{6}\ln\left(1 - \frac{I_1 - 3}{J_m}\right) + \frac{K}{2}\left(\frac{J^2-1}{2} - \ln J\right) \tag{A.14}$$

where E and J_m are the two material parameters. J_m represents the asymptotic maximum value of (I_1-3) that can be undergone by the material.

For incompressible materials, such as biological soft tissues, the last term in Eqs. A.12 to A.14 is considered to be zero ($J = 1$).

There are several other hyperelastic material models such as: Fung [Fung, 1967; Fung, Fronek, and Patitucci, 1979], Ogden [Ogden, 1972], Yeoh [Yeoh, 1993], and Arruda-Boyce [Arruda and Boyce, 1993].

BIBLIOGRAPHY

Abrahams M (1967). "Mechanical Behaviour of Tendon". In: *Med. & biol. Engng* 5.1964, pp. 433–443.

Agache, P. G., C Monneur, J. L. Leveque, and J De Rigal (1980). "Mechanical properties and Young's modulus of human skin in vivo." In: *Archives of dermatological research* 269.3, pp. 221–32.

Aoki, T, T Ohashi, T Matsumoto, and M Sato (1997). "The pipette aspiration applied to the local stiffness measurement of soft tissues". In: *Annals of biomedical engineering* 25.3, pp. 581–7.

Arruda, E. M. and M. C. Boyce (1993). "A Three-dimensional Constitutive Model for the Large Stretch Behaviour of Rubber Elastic Materials". In: *Journal of Mechanics and Physics of Solids* 41, pp. 389–412.

Asbach, P., D. Klatt, U. Hamhaber, J. Braun, R. Somasundaram, B. Hamm, and I. Sack (2008). "Assessment of liver viscoelasticity using multifrequency MR elastography". In: *Magnetic Resonance in Medicine* 60.2, pp. 373–379.

Badir, S., M. Bajka, and E. Mazza (2013). "A novel procedure for the mechanical characterization of the uterine cervix during pregnancy". In: *Journal of the Mechanical Behavior of Biomedical Materials* 27, pp. 143–153.

Barbarino, G. G., M. Jabareen, and E. Mazza (2011). "Experimental and numerical study on the mechanical behavior of the superficial layers of the face". In: *Skin Research and Technology* 17.4, pp. 434–444.

Beatty, M. F. and S. Krishnaswamy (2000). "A theory of stress-softening in incompressible isotropic materials". In: *Journal of the Mechanics and Physics of Solids* 48.9, pp. 1931–1965.

Brouwer, I., J. Ustin, L. Bentley, A. Sherman, N. Dhruv, and F. Tendick (2001). "Measuring in vivo animal soft tissue properties for haptic modeling in surgical simulation". In: *Medicine meets virtual reality*. Ed. by J. D. Westwood. Vol. 81. IOS Press, pp. 69–74.

Brown, J. D., J. Rosen, M. Moreyra, M. Sinanan, and B. Hannaford (2002). "Computer-controlled motorized endoscopic grasper for in vivo measurement of soft tissue biomechanical characteristics". In: *Medicine Meets Virtual Reality 02/10: Digital Upgrades, Applying Moore's Law to Health* 85, pp. 71–73.

Brown, J. D., J. Rosen, Y. S. Kim, L. Chang, M. N. Sinanan, and B. Hannaford (2003). "In-vivo and in-situ compressive properties of porcine abdominal soft tissues". In: *Studies in Health Technology and Informatics* 94, pp. 26–32.

Brown, R. A., R. Prajapati, D. A. McGrouther, I. V. Yannas, and M. Eastwood (1998). "Tensional homeostasis in dermal fibroblasts: Mechanical responses to mechanical loading in three-dimensional substrates". In: *Journal of Cellular Physiology* 175.3, pp. 323–332.

Bucki, M., M. A. Nazari, and Y. Payan (2010). "Finite element speaker-specific face model generation for the study of speech production". In: *Computer Methods in Biomechanics and Biomedical Engineering* 13.4, pp. 459–467.

Budday, S., G. Sommer, C. Birkl, C. Langkammer, J. Haybaeck, J. Kohnert, M. Bauer, F. Paulsen, P. Steinmann, E. Kuhl, and G. A. Holzapfel (2017a). "Mechanical characterization of human brain tissue". In: *Acta Biomaterialia* 48, pp. 319–340.

— (2017b). "Mechanical characterization of human brain tissue". In: *Acta Biomaterialia* 48, pp. 319–340.

Carew, T. E., R. N. Vaishnav, and D. J. Patel (1968). "Compressibilty of the Arterial Wall". In: *Circulation Research* 23, pp. 61–68.

Carter, F. J., T. G. Frank, P. J. Davies, D. McLean, and A. Cuschieri (2001). "Measurements and modelling of the compliance of human and porcine organs". In: *Medical Image Analysis* 5.4, pp. 231–236.

Chagnon, G., G. Marckmann, and E. Verron (2004). "A comparison of the hart-smith model with arruda-boyce and gent formulations for rubber elasticity". In: *Rubber chemistry and technology* 77.4, pp. 724–735.

Cox, M. A., N. J. Driessen, R. A. Boerboom, C. V. Bouten, and F. P. Baaijens (2008). "Mechanical characterization of anisotropic planar biological soft tissues using finite indentation: Experimental feasibility". In: *Journal of Biomechanics* 41.2, pp. 422–429.

Diridollou, S., F. Patat, F. Gens, L. Vaillant, D. Black, J. M. Lagarde, Y. Gall, and M. Berson (2000). "In vivo model of the mechanical properties of the human skin under suction." In: *Skin research and technology : official journal of International Society for Bioengineering and the Skin (ISBS) [and] International Society for Digital Imaging of Skin (ISDIS) [and] International Society for Skin Imaging (ISSI)* 6.4, pp. 214–221.

Dorfmann, A. and R. W. Ogden (2004). "A constitutive model for the Mullins effect with permanent set in particle-reinforced rubber". In: *International Journal of Solids and Structures* 41.7, pp. 1855–1878.

Elahi, S. A., N. Connesson, and Y. Payan (2018). "Disposable system for in-vivo mechanical characterization of soft tissues based on volume measurement". In: *Journal of Mechanics in Medicine and Biology* 18.04.

Elahi, S. A., N. Connesson, G. Chagnon, and Y. Payan (2018). "In-vivo soft tissues mechanical characterization: volume-based aspiration method validated on silicones". In: *Experimental Mechanics (under revision).*

Farshad, M., M. Barbezat, P. Flueler, F. Shmidlin, P. Graber, and P. Niederer (1999). "Material Characterization of the Pig Kidney in Relation with the Biomechanical Analysis of Rental Trauma". In: *Journal of Biomechanics* 32, pp. 411–425.

Findley, W. N., J. S. Lai, and K. Onaran (1976). *Creep and relaxation of nonlinear viscoelastic materials*. Vol. 19. 1. New York: Dover Publication, p. 118.

Finlay, B. (1971). "The torsional characteristics of human skin in vivo". In: *Biomedical engineering* 6.

Florentin, E. and G. Lubineau (2010). "Identification of the parameters of an elastic material model using the constitutive equation gap method". In: *Computational Mechanics* 46.4, pp. 521–531.

Flynn, C., A. Taberner, and P. Nielsen (2011a). "Measurement of the force-displacement response of in vivo human skin under a rich set of deformations". In: *Medical Engineering and Physics* 33, pp. 610–619.

— (2011b). "Mechanical characterisation of in vivo human skin using a 3D force-sensitive micro-robot and finite element analysis". In: *Biomechanics and Modeling in Mechanobiology* 10, pp. 27–38.

— (2011c). "Modeling the mechanical response of in vivo human skin under a rich set of deformations". In: *Annals of Biomedical Engineering* 39, pp. 1935–1946.

Franceschini, G., D. Bigoni, P. Regitnig, and G. A. Holzapfel (2006). "Brain tissue deforms similarly to filled elastomers and follows consolidation theory". In: *Journal of the Mechanics and Physics of Solids* 54.12, pp. 2592–2620.

Frauziols, F., F. Chassagne, P. Badel, L. Navarro, J. Molimard, N. Curt, and S. Avril (2016). "In vivo Identification of the Passive Mechanical Properties of Deep Soft Tissues in the Human Leg". In: *Strain* 52.5, pp. 400–411.

Fung, Y. C. (1967). "Elasticity of soft tissues in simple elongation". In: *American Journal of Physiology-Legacy Content* 213, pp. 1532–1544.

Fung, Y. C., K. Fronek, and P. Patitucci (1979). "Pseudoelasticity of arteries and the choice of its mathematical expression". In: *American Journal of Physiology-Heart and Circulatory Physiology* 237, pp. 620–631.

Gasser, T. C., R. W Ogden, and G. A Holzapfel (2006). "Hyperelastic modelling of arterial layers with distributed collagen fibre orientations". In: *Journal of The Royal Society Interface* 3.6, pp. 15–35. arXiv: `0312002v1 [arXiv:q-bio]`.

Gent, A. N. (1996). "A new constitutive relation for rubber". In: *Rubber chemistry and technology Technol* 69, pp. 59–61.

Gentleman, E., A. N. Lay, D. A. Dickerson, E. A. Nauman, G. A. Livesay, and K. C. Dee (2003). "Mechanical characterization of collagen fibers and scaffolds for tissue engineering". In: *Biomaterials* 24.21, pp. 3805–3813.

Hendriks, F. M., D. Brokken, C. W. J. Oomens, D. L. Bader, and F. P. T. Baaijens (2006a). "The relative contributions of different skin layers to the mechanical behavior of human skin in vivo using suction experiments". In: *Medical Engineering and Physics* 28.3, pp. 259–266.

— (2006b). "The relative contributions of different skin layers to the mechanical behavior of human skin in vivo using suction experiments". In: *Medical Engineering and Physics* 28.3, pp. 259–266.

Herlin, C., B. Gilles, G. Subsol, and G. Captier (2014). "Generic 3D geometrical and mechanical modeling of the skin/subcutaneous complex by a procedural hybrid method". In: *Lecture Notes in Computer Science*. Vol. 8789, pp. 173–181.

Hill, R. (1950). "A theory of the plastic bulging of a metal diaphragm by lateral pressure". In: *The London, Edinburgh, and Dublin Philosophical Magazine and Journal of Science* 41, pp. 1133–1142.

Hollenstein, M., M. Jabareen, S. Breitenstein, M.-O. Riener, P.-A. Clavien, M. Bajka, and E. Mazza (2009). "Intraoperative mechanical characterization of human liver". In: *Pamm* 9.1, pp. 83–86.

Hollenstein, M., G. Bugnard, R. Joos, S. Kropf, P. Villiger, and E. Mazza (2013). "Towards laparoscopic tissue aspiration". In: *Medical Image Analysis* 17.8, pp. 1037–1045.

Holzapfel, G. A., T. C. Gasser, and M Stadler (2002). "A structural model for the viscoelastic behavior of arterial walls: \mbox{C}ontinuum formulation and finite element analysis". In: *European Journal of Mechanics A/Solids* 21.10, pp. 441–463.

Holzapfel, G. A. and R. W. Ogden (2010). "Constitutive modelling of arteries". In: *Proceedings of the Royal Society A: Mathematical, Physical and Engineering Sciences* 466.2118, pp. 1551–1597. arXiv: 77953418030.

Holzapfel, G. A. (2001). "Biomechanics of soft tissue". In: *Handbook of materials behavior models: nonlinear models and properties*. Ed. by J. Lemaitre. Academic Press, pp. 1057–1071.

Huanh, J.-l., G.-j. Xie, and Z.-w. Liu (2008). "FEA of hyperelastic rubber material based on Mooney-Rivlin model and Yeoh model [J]". In: *China Rubber Industry* 8.

Jor, J. W. Y., M. D. Parker, A. J. Taberner, M. P. Nash, and P. M. F. Nielsen (2013). "Computational and experimental characterization of skin mechanics: Identifying current challenges and future directions". In: *Wiley Interdisciplinary Reviews: Systems Biology and Medicine* 5, pp. 539–556.

Kauer, M., V. Vuskovic, J. Dual, G. Szekely, and M. Bajka (2001). "Inverse finite element characterization of soft tissues". In: *Medical Image Analysis* 2208, pp. 128–136.

Kauer, M. (2001). "Inverse Finite Element Characterization of Soft Tissues with Aspiration Experiments Inverse Finite Element Characteriza- tion of Soft Tissues with Aspiration". PhD thesis. Swiss Federal Institute of Technology.

Kenedi, R. M., T Gibson, J. H. Evans, and J. C. Barbenel (1975). "Tissue Mechanics". In: *Physics in Medecine and Biology* 20.5, pp. 699–717.

Kerdok, A. E., M. P. Ottensmeyer, and R. D. Howe (2006). "Effects of perfusion on the viscoelastic characteristics of liver". In: *Journal of Biomechanics* 39.12, pp. 2221–2231.

Lally, C., A. J. Reid, and P. J. Prendergast (2004). "Elastic behavior of porcine coronary artery tissue under uniaxial and equibiaxial tension". In: *Annals of Biomedical Engineering* 32.10, pp. 1355–1364.

Liu, I.-S. (2002). *Continuum Mechanics*. Springer-Verlag.

Luboz, V., E. Promayon, and Y. Payan (2014). "Linear Elastic Properties of the Facial Soft Tissues Using an Aspiration Device: Towards Patient Specific Characterization". In: *Annals of Biomedical Engineering* 42.11.

Luboz, V., M. Bailet, C. Boichon Grivot, M. Rochette, B. Diot, M. Bucki, and Y. Payan (2018). "Personalized modeling for real-time pressure ulcer prevention in sitting posture". In: *Journal of Tissue Viability* 27.1, pp. 2–9.

Luboz, V., E. Promayon, G. Chagnon, T. Alonso, D. Favier, C. Barthod, and Y. Payan (2012). "Validation of a Light Aspiration Device for In Vivo Soft Tissue Characterization (LASTIC)". In: *Soft Tissue Biomechanical Modeling for Computer Assisted Surgery*. Vol. 11. Berlin: Springer-Verlag, pp. 243–256.

Machado, G., G. Chagnon, and D. Favier (2010). "Analysis of the isotropic models of the Mullins effect based on filled silicone rubber experimental results". In: *Mechanics of Materials* 42.9, pp. 841–851.

Machado, G., A. Stricher, G. Chagnon, and D. Favier (2017). "Mechanical behavior of architectured photosensitive silicone membranes: Experimental data and numerical analysis". In: *Mechanics of Advanced Materials and Structures* 24.6, pp. 524–533.

Machado, G. (2011). "A contribution to the study of induced anisotropy by Mullins effect in silicone rubber". PhD thesis. Grenoble Alpes University.

Maher, E., A. Creane, C. Lally, and D. J. Kelly (2012). "An anisotropic inelastic constitutive model to describe stress softening and permanent deformation in arterial tissue". In: *Journal of the Mechanical Behavior of Biomedical Materials* 12, pp. 9–19.

Marckmann, G. and E. Verron (2006). "Comparison of hyperelastic models for rubber-like materials". In: *Rubber chemistry and technology* 7, pp. 835–858.

Masri, C. (2017). "Study of the elastomeric silicone cuff of an artificial urinary sphincter". PhD thesis. Grenoble Alpes University.

Mazza, E., O. Papes, M. B. Rubin, S. R. Bodner, and N. S. Binur (2005). "Nonlinear elastic-viscoplastic constitutive equations for aging facial tissues". In: *Biomechanics and Modeling in Mechanobiology* 4.2-3, pp. 178–189.

Mazza, E., M. Parra-Saavedra, M. Bajka, E. Gratacos, K. Nicolaides, and J. Deprest (2014). "In vivo assessment of the biomechanical properties of the uterine cervix in pregnancy". In: *Prenatal Diagnosis* 34.1, pp. 33–41.

Menard, K. P. (2008). *Dynamic mechanical analysis: a practical introduction*. CRC Press.

Miller, K and K Chinzei (2002). "Mechanical properties of brain tissue in tension". In: *Journal of Biomechanics* 35.4, pp. 483–490.

Miller, K., K. Chinzei, G. Orssengo, and P. Bednarz (2000). "Mechanical properties of brain tissue in-vivo: Experiment and computer simulation". In: *Journal of Biomechanics* 33.11, pp. 1369–1376.

Mîra, A., A.-k. Carton, S. Muller, and Y. Payan (2018). "BREAST biomechanical modelling for compression optimization in digital breast Tomosynthesis". In: *Computer Methods in Biomechanics and Biomedical Engineering*. Ed. by G. A. and W. D. Springer, pp. 29–35.

Mooney, M. (1940). "A theory of large elastic deformation". In: *Journal of Applied Physics* 11.9, pp. 582–592. arXiv: `arXiv:1011.1669v3`.

Morris, K. A. (2011). "What is Hysteresis?" In: *Applied Mechanics Reviews* 64.5.

Mullins, L (1948). "Effect of stretching on the properties of rubber". In: *Rubber Chemistry and Technology* 21.2, pp. 281–300.

— (1969). "Softening of rubber by deformation". In: *Rubber chemistry and technology* 42.1, pp. 339–362.

Mullins, L and N. R. Tobin (1965). "Stress softening in rubber vulcanizates. Part I. Use of a strain amplification factor to describe the elastic behavior of fillerreinforced vulcanized rubber". In: *Journal of Applied Polymer Science* 9, pp. 2993–3009.

Muñoz, M. J., J. A. Bea, J. F. Rodríguez, I. Ochoa, J. Grasa, A. Pérez del Palomar, P. Zaragoza, R. Osta, and M. Doblaré (2008). "An experimental study of the mouse skin behaviour: Damage and inelastic aspects". In: *Journal of Biomechanics* 41.1, pp. 93–99.

Nava, A., E. Mazza, M. Furrer, P. Villiger, and W. H. Reinhart (2008). "In vivo mechanical characterization of human liver". In: *Medical Image Analysis* 12.2, pp. 203–216.

Nelder, J. A. and R. Mead (1965). "A simplex method for function minimization". In: *The computer journal* 7, pp. 308–313.

Ní Annaidh, A., K. Bruyère, M. Destrade, M. D. Gilchrist, and M. Otténio (2012). "Characterization of the anisotropic mechanical properties of excised human skin". In: *Journal of the Mechanical Behavior of Biomedical Materials* 5.1, pp. 139–148. arXiv: 1302.3022.

Nicolas, E., S. Callé, S. Nicolle, D. Mitton, and J. P. Remenieras (2018). "Biomechanical characterization of ex vivo human brain using ultrasound shear wave spectroscopy". In: *Ultrasonics* 84, pp. 119–125.

Odegard, G, T. S. Gates, and H. B.T.E. M. Herring (2005). "Characterization of viscoelastic properties of polymeric materials through nanoindentation". In: *Experimental Mechanics* 45.2, pp. 130–136.

Ogden, R. W. (1972). "Large deformation isotropic elasticity - on the correlation of theory and experiment for incompressible rubberlike solids". In: *Proceedings of the Royal Society A: Mathematical, Physical and Engineering Sciences* 326, pp. 565–584. arXiv: arXiv:1205.0516v2.

— (1997). *Non-linear elastic deformations*. New York: Dover Publications.

Omari, E. A., T. Varghese, M. A. Kliewer, J. Harter, and E. M. Hartenbach (2015). "Dynamic and quasi-static mechanical testing for characterization of the viscoelastic properties of human uterine tissue". In: *Journal of Biomechanics* 48.10, pp. 1730–1736. arXiv: 15334406.

Payan, Y. and J. Ohayon, eds. (2017). *Biomechanics of Living Organs: Hyperelastic constitutive laws for finite element modeling*. Academic P. Elsevier.

Peña, E. (2014). "Computational aspects of the numerical modelling of softening, damage and permanent set in soft biological tissues". In: *Computers and Structures* 130, pp. 57–72.

— (2011). "Prediction of the softening and damage effects with permanent set in fibrous biological materials". In: *Journal of the Mechanics and Physics of Solids* 59.9, pp. 1808–1822.

Pensalfini, M., J. Weickenmeier, M. Rominger, R. Santoprete, O. Distler, and E. Mazza (2018). "Location-specific mechanical response and morphology of facial soft tissues". In: *Journal of the Mechanical Behavior of Biomedical Materials* 78.October 2017, pp. 108–115.

Picinbono, G., N. Ayache, E. Project, S.-a. Cedex, and H Delingette (2001). "Non-linear and anisotropic elastic soft tissue models for medical simulation". In: *IEEE Int Conf Robot and Automation* 2.1, pp. 1370–1375.

Qi, H. J. and M. C. Boyce (2004). "Constitutive model for stretch-induced softening of the stress-stretch behavior of elastomeric materials". In: *Journal of the Mechanics and Physics of Solids* 52.10, pp. 2187–2205.

Rebouah, M. (2014). "Anisotropic stress softening and viscoelasticity in rubber like materials and architectured materials". PhD thesis. Grenoble Alpes University.

Rey, T., G. Chagnon, J. B. Le Cam, and D. Favier (2013). "Influence of the temperature on the mechanical behaviour of filled and unfilled silicone rubbers". In: *Polymer Testing* 32.3, pp. 492–501.

Rosen, J., B. Hannaford, M. P. MacFarlane, and M. N. Sinanan (1999). "Force controlled and teleoperated endoscopic grasper for minimally invasive surgery - Experimental performance evaluation". In: *IEEE Transactions on Biomedical Engineering* 46.10, pp. 1212–1221.

Samani, A., J. Zubovits, and D. Plewes (2007). "Elastic moduli of normal and pathological human breast tissues: An inversion-technique-based investigation of 169 samples". In: *Physics in Medicine and Biology* 52.6, pp. 1565–1576.

Samur, E., M. Sedef, C. Basdogan, L. Avtan, and O. Duzgun (2007). "A robotic indenter for minimally invasive measurement and characterization of soft tissue response". In: *Medical Image Analysis* 11.4, pp. 361–373.

Sanders, R. (1973). "Torsional elasticity of human skin in vivo". In: *Pflugers Archive European Journal of Physiology* 342.3, pp. 255–260.

Schiavone, P, T Boudou, E Promayon, P Perrier, and Y Payan (2008). "A light sterilizable pipette device for the in vivo estimation of human soft tissues constitutive laws." In: *Conference proceedings : Annual International Conference of the IEEE Engineering in Medicine and Biology Society. IEEE Engineering in Medicine and Biology Society. Conference*. Vol. 2008, pp. 4298–301.

Schiavone, P., F. Chassat, T. Boudou, E. Promayon, F. Valdivia, and Y. Payan (2009). "In vivo measurement of human brain elasticity using a light aspiration device". In: *Medical Image Analysis* 13.4, pp. 673–678. arXiv: `0904.1267`.

Schiavone, P., E. Promayon, and Y. Payan (2010). "LASTIC : a Light Apiration device for in vivo Soft TIssue Characterization". In: *5th International Symposium on Biomedical Simulation ISBMS10*. Springer-Verlag, pp. 1–10.

Schwenninger David, D., S. Schumann, and J. Guttmann (2011). "In vivo characterization of mechanical tissue properties of internal organs using endoscopic microscopy and inverse finite element analysis". In: *Journal of Biomechanics* 44.3, pp. 487–493.

Snedeker, J. G., M. Bajka, J. M. Hug, and P. Niederer (2002). "The creation of a high-fidelity finite element model of the kidney for use in trauma research". In: *Journal of Visualization and Computer Animation* 13.1, pp. 53–64.

Sun, W. and M. S. Sacks (2005). "Finite element implementation of a generalized Fung-elastic constitutive model for planar soft tissues". In: *Biomechanics and Modeling in Mechanobiology* 4, pp. 190–199.

Székely (2003). "Surgical simulators." In: *Minimally invasive therapy & allied technologies : MITAT : official journal of the Society for Minimally Invasive Therapy* 12.1, pp. 14–8.

Treloar, L. R. G. (1943a). "The elasticity of a network of long-chain molecules I". In: *Transactions of the Faraday Society*, pp. 36–41.

— (1943b). "The elasticity of a network of long-chain molecules II". In: *Transactions of the Faraday Society*, pp. 241–246.

Valtorta, D. and E. Mazza (2005). "Dynamic measurement of soft tissue viscoelastic properties with a torsional resonator device". In: *Medical Image Analysis* 9.5 SPEC. ISS. Pp. 481–490.

Veronda, D. R. and R. A. Westmann (1970). "Mechanical characterization of skin-Finite deformations". In: *Journal of Biomechanics* 3.1.

Vexler, A., I. Polyansky, and R. Gorodetsky (1999). "Evaluation of skin viscoelasticity and anisotropy by measurement of speed of shear wave propagation with viscoelasticity skin analyzer". In: *Journal of Investigative Dermatology* 113.5, pp. 732–739.

Vuskovic, V (2001). "Device for in-vivo measurement of mechanical properties of internal human soft tissues". PhD thesis. Swiss Federal Institute of Technology.

Weickenmeier, J., M. Jabareen, and E. Mazza (2015). "Suction based mechanical characterization of superficial facial soft tissues". In: *Journal of Biomechanics* 48.16, pp. 4279–4286.

Xu, M. and J. Yang (2015). "Human Facial Soft Tissue Thickness and Mechanical Properties: A Literature Review". In: *Volume 1A: 35th Computers and Information in Engineering Conference*. November, V01AT02A045.

Yao, W., K. Yoshida, M. Fernandez, J. Vink, R. J. Wapner, C. V. Ananth, M. L. Oyen, and K. M. Myers (2014). "Measuring the compressive viscoelastic mechanical properties of human cervical tissue using indentation". In: *Journal of the Mechanical Behavior of Biomedical Materials* 34, pp. 18–26.

Yeoh, O. H. (1993). "Some forms of the strain energy function for rubber". In: *Rubber chemistry and technology* 66, pp. 754–771.

Zemánek, M., J. Burša, and M. Děták (2009). "Biaxial Tension Tests with Soft Tissues of Arterial Wall". In: *Engineering Mechanics* 16.1, pp. 3–11.

Zhao, R., K. L. Sider, and C. A. Simmons (2011). "Measurement of layer-specific mechanical properties in multilayered biomaterials by micropipette aspiration". In: *Acta Biomaterialia* 7.3, pp. 1220–1227.